Spring 1-1-2011

Optimizing Two Pairs of GRACE-like Satellites for Recovering Temporal Gravity Variations

David N. Wiese
University of Colorado at Boulder, wiese@colorado.edu

Optimizing Two Pairs of GRACE-like Satellites for Recovering Temporal Gravity Variations

by

David N. Wiese

B.S., Aerospace Engineering, The University of Texas at Austin, 2005

M.S. Aerospace Engineering Sciences, University of Colorado at Boulder, 2007

A thesis submitted to the

Faculty of the Graduate School of the

University of Colorado in partial fulfillment

of the requirements for the degree of

Doctor of Philosophy

Department of Aerospace Engineering Sciences

2011

This thesis entitled:
Optimizing Two Pairs of GRACE-like Satellites for Recovering Temporal Gravity Variations
written by David N. Wiese
has been approved for the Department of Aerospace Engineering Sciences

Dr. R. Steven Nerem

Dr. Peter Bender

Dr. Srinivas Bettadpur

Dr. Frank Lemoine

Dr. Pieter Visser

Dr. John Wahr

Date

The final copy of this thesis has been examined by the signatories, and we find that both the content and the form meet acceptable presentation standards of scholarly work in the above mentioned discipline.

Wiese, David N. (Ph.D., Aerospace Engineering Sciences)

Optimizing Two Pairs of GRACE-like Satellites for Recovering Temporal Gravity Variations

Thesis directed by Dr. R. Steven Nerem

The Gravity Recovery and Climate Experiment (GRACE) mission has demonstrated the ability to quantify global mass variations at large spatial scales with monthly to sub-monthly temporal resolution. It is expected that future missions will take advantage of improved technologies by flying drag-free and performing the satellite-to-satellite ranging with a laser interferometer. With these improvements, errors due to undersampling geophysical signals will be the limiting error source. In an effort to reduce the level of these temporal aliasing errors, we suggest the addition of a second pair of satellites.

A Monte-Carlo analysis using numerical simulations is used to reduce the search space for finding an optimal architecture consisting of two satellite pairs. A search space originally consisting of fifteen variables is reduced to two variables with the utmost impact on mission performance: the repeat period of both satellite pairs (shown to be near-optimal when they are equal to each other), and the inclination of one of the satellite pairs (the other is assumed to be in a polar orbit). With appropriate assumptions, we find that an optimal architecture consists of a polar pair of satellites at 320 km coupled with a 290 km pair inclined at 72^o, both in 13-day repeating orbits. The option of estimating low resolution gravity fields at a high frequency is shown to further reduce temporal aliasing errors.

Global and regional analyses are performed to quantify the expected scientific benefits of adding an optimally-placed second pair of satellites. Analysis using empirical orthogonal functions reveals that two satellite pairs determines annual and semi-annual mass variations in small basins which are undetected using one pair of satellites. Averaging kernels and spatiospectral localization are used to show error reductions ranging from 25% - 75% in determining mass variations over the year in 53 hydrological basins, 12 Greenland basins, and one ocean basin. A simulated earthquake

signal is also shown to be detected with higher spatial resolution. Perhaps the largest benefit of having two satellites pairs is that the gravity solutions do not necessitate ad-hoc GRACE post-processing techniques of removing correlated errors and smoothing when studying signals to spatial resolution of $\sim$ 330 km.

Dedication

To my beautiful wife, and her newly found love for gravity.

Acknowledgements

I would like to thank my research advisor, Dr. Nerem for his continued support and guidance with this project. Also from the University of Colorado, I owe many thanks to Dr. Peter Bender and Sean Swenson (at NCAR) for the multitude of stimulating discussions, as well as Dr. John Wahr for making complicated matters seem so simple at times. I cannot express enough gratitude to Bryant Loomis (now at SGT) for teaching me GEODYN and setting up our computing cluster.

I would especially like to thank Dr. Bill Folkner of JPL for helping me get started on this research. Dr. Willy Bertiger, Dr. Paul Thompson, and Dr. Mike Watkins also have my gratitude for all the help they gave me during the summer of 2006 at JPL. Many thanks to Dr. Pieter Visser for mentoring and guiding me while at TU Delft University in the fall of 2008. I am also very grateful to Dr. Frank Lemoine for hosting me at Goddard Space Flight Center in the fall of 2010. Thanks to Dr. Shin-Chan Han, Scott Luthcke, Dave Rowlands, and Terry Sabaka for making my visit to Goddard a very memorable and productive one. Thank you also to Dr. Srinivas Bettadpur and Dr. Nico Sneeuw for the many useful discussions. This research was funded by the NSF through the GRFP, the DoD through the NDSEG Fellowship program, and the NASA GRACE Science Team investigation. I am grateful to all three funding agencies.

I would like to express a very special thank you to my parents and siblings. Thank you for believing in me and encouraging me. I never thought I would see the day that my little sister and I would be studying in college simultaneously, but alas, it has come! And finally, to my beautiful and loving wife. While I may not be the kind of doctor that helps people, or makes any money, your support has helped me get to this point today. Thank you.

Contents

Chapter

Tables

Table

Figures

Figure

Chapter 1

Introduction

1.1 Why do we care about Gravity Measurements?

Isaac Newton first formulated the law of universal gravitation, stating that the force of gravity between two point masses is a function of the mass of the two objects and the square of the distance between them. Extending this problem to the Earth, which is not a point mass, the gravitational force at any point on or above the Earth's surface must be computed taking into account the inhomogeneous mass distribution of the Earth. If one takes multiple measurements of gravity at the same location but at different times, then time-variable gravity can be studied; that is, how gravity changes over time. This change in gravity is directly related to how mass is being redistributed within the Earth system, primarily in the form of water. Quantifying this mass redistribution is of interest to many scientific disciplines and areas of study, some of which are listed below [*Sneeuw et al.*, 2005].

- *Solid Earth Sciences* - monitoring glacial isostatic adjustment, core motion, and plate tectonics.
- *Hydrology* - monitoring ground water transport, soil moisture, and precipitation.
- *Oceanography* - determining mean flow, coastal currents, bathymetry, and bottom currents.
- *Sea Level* - monitoring global ocean mass change.
- *Glaciology* - monitoring melting and/or accumulation of polar ice caps, making ice mass balance estimates.
- *Geodesy* - determining precise geoid heights, aiding in orbit determination and inertial navigation by creating better static gravity field models.

Each of these areas of interest has very different spatial and temporal scales. Figure 1.1 gives a detailed breakdown of the different spatial and temporal scales associated with geophysical processes on the Earth. Any single satellite mission dedicated to recovering the gravity field cannot determine the full range of spatial and temporal scales necessary to benefit all areas of science included in Figure 1.1. Thus, the targeted spatial and temporal resolution of a gravity mission directly affects which areas of science will benefit.

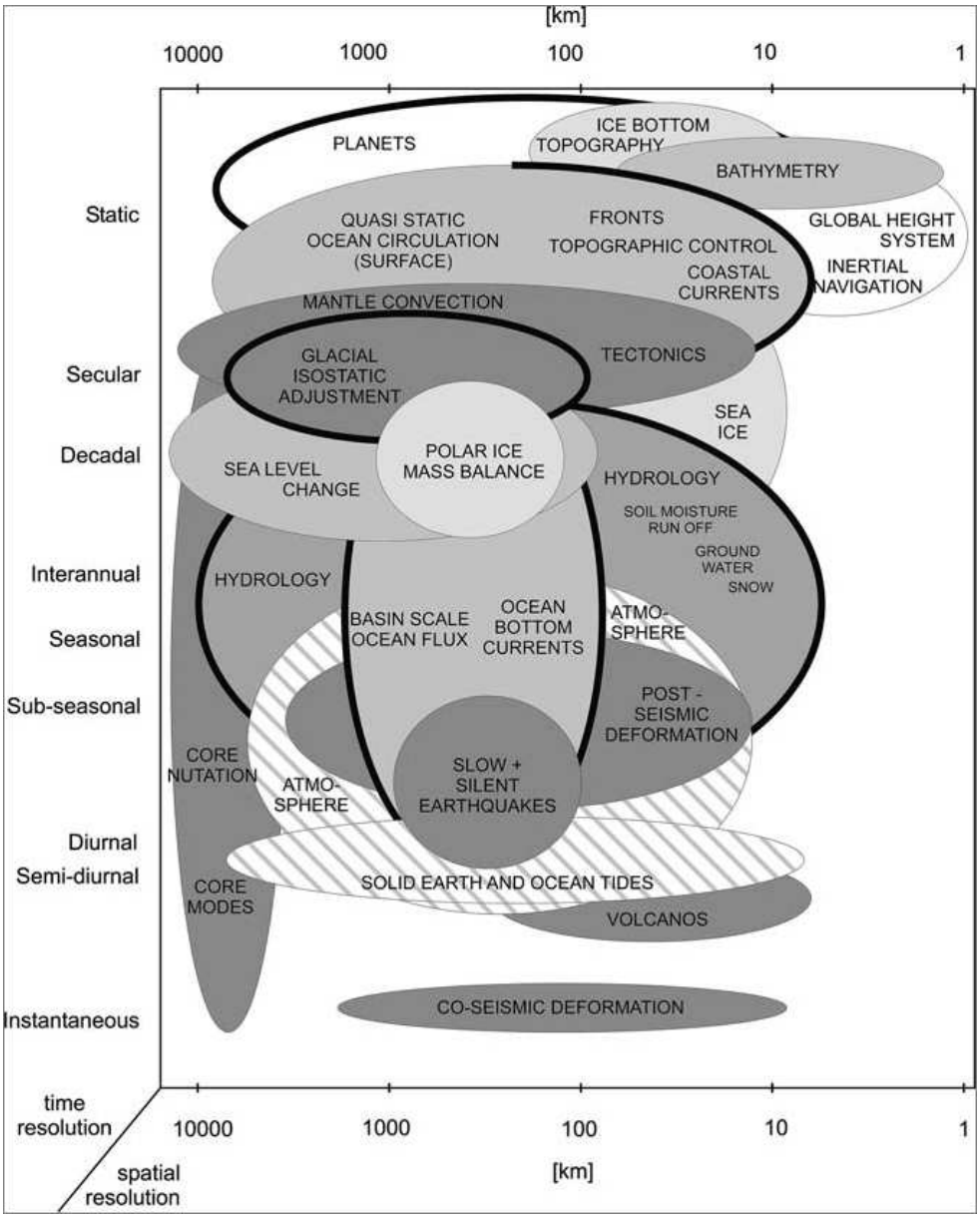

Figure 1.1: Temporal and spatial scales of geophysical processes, taken from *Sneeuw et al.* [2005]

1.2 History of Gravity Measurements

Most of the scientific areas of study listed in Section 1.1 involve the study of the Earth as a dynamic system, thus a time-series of gravity measurements are beneficial. Global time-variable gravity measurements allowing for the study of many of the phenomena shown in Figure 1.1 were not available until recently, when the Gravity Recovery and Climate Experiment (GRACE) satellites were launched in 2002. However, prior to GRACE, many efforts were made to take gravity measurements and create a static gravity field model of the Earth.

Prior to the space age, gravity measurements had to be taken either on the land, using terrestrial gravimetry techniques, or through the air, using airborne gravimetry. Both of these processes were painstaking, and often hampered by both political and geographical boundaries [*Nerem et al.*, 1995].

The launch of Sputnik in 1957 marked the advent of satellite geodesy, and offered an easier way to create a global gravity model of the Earth by tracking satellites and measuring perturbations in their orbits. Through the mid-1960s, satellite cameras, radio Doppler, and radio interferometry were primarily used to track satellites. The mid-1960s saw the development of the satellite laser ranging (SLR) technique, which greatly increased satellite tracking accuracy, but was limited both spatially and temporally, as there were a limited number of satellites in desirable orbits as well as a sparse distribution of tracking stations around the globe. Gravity field models of the Earth were developed using these data, but all were limited in their spatial resolution [*Nerem et al.*, 1995].

Satellite altimetry further advanced the spatial resolution in the gravity field models. A measurement of geoid height (an equipotential surface) was made simply by measuring the height of the oceans and applying corrections to the measurements due to tidal and pressure variations. Data from GEOS 3 (1975), Seasat (1978), Geosat (1985), ERS 1 (1991) and ERS 2 (1995), and TOPEX/POSEIDON (1991), Jason-1 (2001), and Jason-2 (2008) all have provided improvements in the determination of the static gravity field [*Nerem et al.*, 1995].

The early 1990s brought with it two separate systems which quickly advanced the field of

satellite geodesy by offering continuous, accurate satellite tracking: the French Doppler Orbitography and Radiopositioning Integrated by Satellite (DORIS) system, and the Global Positioning System (GPS). DORIS is a network of over fifty groundstations operated by France, offering near continuous tracking of satellites by measuring Doppler shifts of radio signals. GPS took the idea of global coverage one step further by placing a constellation of satellites in Medium Earth Orbit (MEO) to provide continuous tracking of any satellite with a GPS receiver onboard [*Nerem et al.*, 1995]. These technologies allowed for much more accurate static gravity field models of the Earth to be created. In 1998, EGM96 was released, representing the most accurate gravity model to date. EGM96 was the result of a joint collaboration between between NASA Goddard Space Flight Center (GSFC) and the National Imagery and Mapping Association (NIMA) using years of satellite tracking and terrestrial gravity measurements [*Lemoine et al.*, 1998].

In July of 2000, the Challenging Mini Satellite Payload (CHAMP) satellite was launched with one goal being to quantify the Earth's gravity field using a high precision GPS receiver. CHAMP was found to be able to quantify annual and semiannual variations in the Earth's gravity field when combined with SLR ranging data to different satellites, including the Laser Geodynamics Satellites (LAGEOS), out to approximately spherical harmonic degree 5 [*Moore et al.*, 2005]. With more recent improvements in data processing, CHAMP has been shown to recover time-variable gravity in monthly intervals out to degree 10 [*Flechtner*, 2010], making it truly the first satellite to measure time variable gravity beyond J_2, as LAGEOS has already done.

However, there was still room for improvement after the launch of CHAMP. It was first pointed out in 1969 that a low-low system, consisting of measurements between two satellites in Low Earth Orbit (LEO), would provide better accuracy than that of a high-low system (such as LEO satellites being tracked by GPS) [*Wolff*, 1969]. In 2002, GRACE became the first dedicated low-low satellite mission dedicated to measuring the Earth's gravity field. Along with it came the first time-variable gravity measurements ever for higher degrees, allowing for increased spatial resolution in determining mass movement about the Earth. The original mission lifetime of GRACE was through 2007, but it has been running on an extended mission since then. Barring instrument

failure, it is expected that the GRACE mission could continue performing through 2019 before fuel runs out and the satellites deorbit due to atmospheric drag forces. However, at the time of publication, failure of the batteries are of prime concern limiting the mission lifetime [*Beerer and Massmann*, 2010]. The success of the GRACE mission has scientists from many different disciplines calling for a follow-on mission to extend the time series of measurements. While a follow-on mission has been scheduled in the NASA decadal survey with a tentative launch date around 2020, it is also expected that additional funding for a gap-filler mission with a launch date of 2016 will be appropriated. The tentative scheduling of these two missions leaves the scientific community hopeful of the continuation of the time series of gravity measurements, allowing for discrimination between secular signals and those with decadal periods.

The latest satellite mission which is dedicated to studying the gravity field is the Gravity Field and Steady-State Ocean Circulation (GOCE) mission, which was launched in March of 2009 by the European Space Agency (ESA). Unlike GRACE, GOCE is not designed to focus on time-variable gravity, but instead aims to gain a much more accurate static gravity field model of the Earth [*Drinkwater et al.*, 2007]. The preliminary results from the GOCE mission have been extremely encouraging.

This research focuses on the design of a follow-on mission to GRACE with the primary scientific objective being the measurement of time variable gravity. Thus, future discussions will involve the GRACE satellite mission.

1.3 GRACE: Mission Overview and Scientific Results

GRACE consists of two identical satellites in nearly circular polar orbits (inclination= 89.5^o) at an altitude of approximately 500 km. The two satellites are separated in the along-track direction by approximately 220 km. GRACE has no altitude control system, so the altitude of the satellites continually decays due to atmospheric drag forces. The two satellites are linked by a highly accurate K-Band microwave ranging system [*Dunn et al.*, 2003], which can measure the distance between the spacecraft to the micron level. Each spacecraft is equipped with a high precision accelerometer

[*Touboul et al.*, 1999] along with GPS receivers. The accelerometers are necessary because the mission objective of GRACE is to be able to isolate the motion of the satellites due to the Earth's gravitational field only; thus, the accelerometers allow one to measure and remove the effect of all non-conservative forces (i.e. atmospheric drag, solar radiation pressure, Earth radiation pressure, etc.) acting on the spacecraft in post-processing of the data. The GPS receivers allow for precise orbit determination of the satellites along with precise time-tagging of the inter-satellite range-rate measurements [*Tapley et al.*, 2004a]. The chief observable of the GRACE mission is the set of inter-satellite range-rate measurements. These measurements, when combined with the GPS and accelerometer data, are put into a weighted least-squares filter to solve for the spherical harmonics coefficients which define the Earth's gravitational field in monthly intervals. Some groups have pushed the temporal resolution of GRACE, solving for gravity fields every ten days [*Bruinsma et al.*, 2010; *Sabaka et al.*, 2010], while the University of Bonn has adapted a Kalman filter to solve for gravity fields in daily intervals [*Kurtenbach et al.*, 2009].

GRACE has been a very successful mission to date, providing static gravity models more than an order of magnitude better at long and mid-range wavelengths than their predecessors, including EGM96 [*Tapley et al.*, 2004a]. More importantly, scientists have used the GRACE data to quantify temporal variations in important geophysical processes across the Earth. An entire book could be written on the scientific accomplishments of the GRACE mission. While there is not room for this account here, some of the more prominent accomplishments of GRACE are that scientists have been able to measure ice mass loss in Greenland [*Wu et al.*, 2010; *Velicogna*, 2009; *Luthcke et al.*, 2006], Antarctica [*Chen et al.*, 2009], and the Alaskan glaciers [*Luthcke et al.*, 2008], as well to monitor terrestrial water storage in some of the world's largest river basins [*Han et al.*, 2005; *Rodell et al.*, 2007] and depleting water tables in India [*Rodell et al.*, 2009; *Tiwari et al.*, 2009]. Furthermore, sea level rise [*Leuliette and Miller*, 2009] and ocean bottom pressure variations [*Chambers and Willis*, 2010] have been studied with the GRACE data along with large earthquake signals, including the 2004 Sumatra-Andaman earthquake [*Chen et al.*, 2007; *Panet et al.*, 2007; *Han and Simons*, 2008] and the 2010 Maule, Chile earthquake [*Han et al.*, 2010; *Heki and Matsuo*, 2010]. A good summary

of the accomplishments of the GRACE mission up through 2009 can be found in *Loomis* [2009].

1.4 Improving upon GRACE

When one thinks of quantifying the performance of the GRACE mission, one can think in terms of temporal and spatial resolution of the derived gravity fields; that is, how often does GRACE provide a global gravity field estimate, and what is the spatial resolution of this estimated global gravity field? Traditionally, the temporal resolution of GRACE is 30 days, as a new gravity field estimate is made every month. As mentioned previously, however, some groups have managed to get ten-day solutions and even daily solutions from the GRACE data. The daily solutions are not independent from one another, however; they are tied together via a Kalman filter using constraints on apriori information. Quantifying the spatial resolution of GRACE is a bit more complicated, as the spatial resolution for signals across the globe can be different based on the density of the groundtracks in the area, the magnitude of the geophysical signal, as well as the magnitude of the errors in the particular location. Typically, however, users tend to view 400 km as a lower limit on the spatial resolution of the GRACE data. It should be noted that the spatial resolution of the derived static gravity field (gained from combining years of GRACE data) is considerably higher than that of the monthly gravity fields.

When designing a follow-on mission, it is desirable to understand the limiting sources of error for GRACE such that one can design a new mission to gain improved spatial and temporal resolution of the solutions. Unfortunately, the limiting error source for GRACE is not yet fully understood [*Visser et al.*, 2010]. However, what one can do in this circumstance is to isolate each individual source of error in a simulation environment, predict what the limiting source of error will be for future missions, and study methods to gain better spatial and temporal resolution. Currently, it is thought the largest errors associated with GRACE are due to the microwave ranging instrument, the accelerometers, attitude errors, orbit errors, and temporal aliasing errors due to undersampling geophysical signals of interest as well as mis-modelling unwanted signals [*Loomis et al.*, 2010]. Each of these error sources will be discussed in the following paragraphs.

One possible way to increase the spatial resolution for a follow-on mission which has been discussed for some time is to replace the microwave ranging instrument with a laser interferometer [*Bender*, 1992; *Colombo and Chao*, 1997; *Bender et al.*, 2003; *Aguirre-Martinez and Sneeuw*, 2002; *Pierce et al.*, 2008], allowing the distances between the spacecraft to be measured with greater accuracy. The K-band microwave ranging instrument measures the inter-satellite baseline distances to the micrometer level; a laser interferometer is expected to make the measurements with approximately 3 orders of magnitude greater precision, down to the nanometer level.

Another possible way to improve mission performance is to use a drag-compensation system (flying "drag-free") rather than using accelerometers to measure non-gravitational forces. The advantage of drag-free operation is that rather than measuring non-gravitational forces acting on the satellite, a shielded proof mass is used as a reference point for the inter-satellite measurements. A thruster system then operates to counteract non-gravitational forces acting on the satellite to keep it centered about the proof mass. The proof mass acceleration noise is lower than in the case of an accelerometer since the uncertainty associated with accelerometer scale factor is avoided. The GOCE mission is the first mission to successfully implement single-axis drag-free control [*Drinkwater et al.*, 2007]. Further development of drag-free technology is under way for the Laser Interferometer Space Antenna (LISA) mission [*Dolesi et al.*, 2003] as well. Implementing drag-free technology may also allow the spacecraft to fly at lower altitudes, giving better sensitivity to short wavelength features in the gravity field [*Aguirre-Martinez and Sneeuw*, 2002]. The disadvantage to flying at lower altitudes is that atmospheric drag forces increase exponentially at lower altitudes, thus, limiting the lifetime of the satellites. For example, GOCE was designed for an approximate 2-year mission lifetime at an altitude of 255 km. Conversely, the GRACE mission was designed for a 5-year mission lifetime at 480 km. It should be mentioned, however, that due to the extended solar minimum, GOCE is expected to continue performing long beyond its expected mission lifetime [*Fehringer et al.*, 2010], and, as mentioned previously, GRACE is currently in its ninth year of operations.

Another potential source of error is the attitude of the satellites. This was not considered a potential limiting source of error until recent investigations [*Horwath et al.*, 2011; *Bandikova*

et al., 2010]; as such, it has not been considered in this study. Attitude information is necessary to calculate corrections to the geometric center of the inter-satellite ranging measurements as well as to orient the accelerometers. Attitude information can be improved with better star trackers.

Errors in determining the absolute spacecraft positions are also a source of error in the mission. The GRACE orbits are known to approximately 1 cm. To improve upon this, one would need better GPS receivers onboard or more sophisticated orbit determination strategies when solving for the orbits.

Temporal aliasing errors are also considered to be a leading error source for GRACE [*Thompson et al.*, 2004; *Han et al.*, 2004; *Zenner et al.*, 2010], and arise from undersampling geophysical signals which have a period less than twice the sampling period of the mission, according to the Nyquist sampling theorem. These signals can subsequently be categorized into those with no a priori information, and thus, alias fully, and those for which a priori information from a model is available, mitigating the effect of aliasing. When the GRACE data are processed, the contribution from the atmosphere, oceans, and tides are removed from the data using a set of models, leaving all other signals in the solution (primarily hydrology and ice). Thus, hydrology and ice signals alias fully into the solutions, while the aliasing errors from the atmosphere, oceans, and tides are mitigated by the modelling. There are three primary methods which one can hope to reduce the effect of temporal aliasing errors. The first is by sampling more frequently, which can be achieved using multiple pairs of satellites. The second is to improve the atmosphere, ocean, and tide models, and the third is to co-estimate parameters which vary at high frequencies, such as a set of spherical harmonic coefficients defining these high frequency variations. This study focuses on mitigating temporal aliasing errors via a combination of sampling more frequently with a second pair of satellites, and co-estimating high frequency parameters that define temporal aliasing errors.

Taking into account the above discussion, Figure 1.2 shows the effect of different error sources in determining the geoid height on a simulated satellite mission over 30 days consisting of one pair of collinear satellites at 475 km altitude separated by 220 km. The satellites are in circular, polar orbits, and fly a 30-day repeating groundtrack. These parameters were chosen to be similar to the

current GRACE mission, with the exception of having an exact repeating groundtrack. For this simulation, each source of error was isolated such that its individual effect could be quantified.

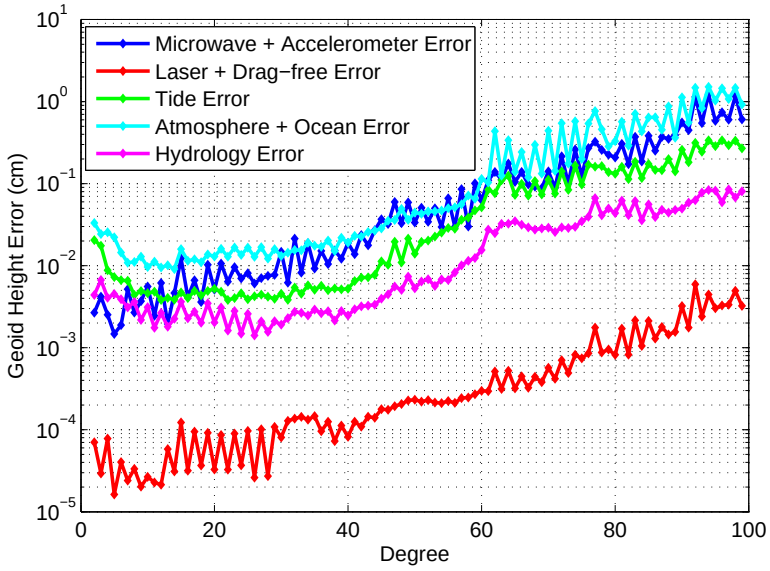

Figure 1.2: Geoid height error as a function of spherical harmonic degree for different isolated sources of error

Two different levels of measurement system errors are considered in Figure 1.2: one case is similar to GRACE with a microwave ranging instrument and accelerometers, and the other case assumes the spacecraft are flying drag-free and the microwave ranging instrument has been replaced with a laser interferometer. Each case is contaminated with 1 cm RMS orbit error. The noise on the microwave ranging instrument is taken to be 1.8 $\mu m/\sqrt{Hz}$ and the accelerometer error is that described in *Loomis et al.* [2010], resembling the level of error in GRACE. The noise on the laser interferometer is taken to be 5 $nm/\sqrt{Hz}$ [*Alnis et al.*, 2008; *Mueller et al.*, December 2005; *Wiese et al.*, 2009; *Young et al.*, 1999], and the noise on the drag-free system is .01 $nm/s^2/\sqrt{Hz}$, which is approximately the level of error of the GOCE accelerometers [*ESA*, 1999]. The atmosphere, ocean, and tide errors are given by the difference between two sets of models, defined in Table 3.1, and the hydrology error is due to undersampling of the GLDAS hydrology model.

Figure 1.2 shows that when only measurement system errors are considered, flying drag-free with a laser interferometer offers several orders of magnitude improvement in determining the height of the geoid over the current GRACE mission. However, the level of errors for undersampling hydrology, and mis-modelling the atmosphere, ocean, and tides are substantially higher than the level of error from the laser interferometer and drag-free system. This indicates that to see an improvement from the laser interferometer and drag-free system, one must first lower the level of errors due to temporal aliasing. Hence, this becomes the motivation for our study. Note that orbit errors at the present level of accuracy are not a limiting source of error.

Additionally, there are two ever present problems associated with the GRACE data that must be addressed: 1) Errors at high degrees tend to dominate the gravity solutions, and (2) correlations between coefficients of a particular order and the same parity of degree lead to longitudinal striping in the gravity solutions. The correlations of (2) arise because the polar orbiting two-satellite collinear architecture that GRACE uses has little East-West sensitivity to variations in the gravity field. These correlated coefficients become difficult to separate during the estimation process, and manifest as North-South errors in the gravity solutions (known as 'stripes'). Several methods have been devised to handle (1) and (2) both collectively and independently. Techniques for handling (1) independently involve spatial smoothing of the data [*Jekeli*, 1981; *Wahr et al.*, 1998; *Han et al.*, 2005; *Chen et al.*, 2006; *Guo et al.*, 2010]. These techniques can reduce the effects of (2) as well if a large enough smoothing radius is selected. Filters devised to handle (2) independently (some of which simultaneously address (1)), can be classified into two categories: empirical filters not reliant on outside information [*Swenson and Wahr*, 2006; *Chambers*, 2006; *Chen et al.*, 2007; *Schrama et al.*, 2007; *Wouters and Schrama*, 2007; *Davis et al.*, 2008; *Duan et al.*, 2009], and filters which make use of error-covariance information [*Kusche*, 2007; *Klees et al.*, 2008; *Save*, 2009]. Each of these techniques has advantages and disadvantages: some reducing errors more than others, and some requiring less computation time than others. Due to lack of error-covariance information and desiring a relatively easy and computationally efficient process to account for the errors, typical users of the GRACE data tend to remove correlated errors via an empirical filter similar to *Swenson*

and Wahr [2006] and reduce errors at high degrees via Gaussian smoothing [*Jekeli*, 1981].

It should additionally be noted that aliasing errors cause striping in the estimated gravity fields; these stripes are referred to as *striations*. They occur because the satellites will pass very near the same location perhaps 10 days apart, but get very different measurements of gravity due to changes that have taken place on short time scales within the 10 days (tides, atmosphere, hydrology, oceans). These different measurements at the same location, but at different times, appear as *striations* in the monthly estimate of the gravity field.

From a design standpoint, it would be desirable to adopt a mission architecture such that the resulting gravity solutions do not require the post-processing techniques discussed above. One way to do this is to fly an alternative satellite formation where measurements in more than one direction are made. For example, measurements made by satellites in a cartwheel formation are directed in a continually-varying combination of along-track and radial directions, thus enhancing the spatial resolution of the derived gravity fields and reducing the longitudinal striping [*Sharifi et al.*, 2007; *Wiese et al.*, 2009; *Elsaka*, 2010]. Another option would be to have multiple collinear satellite pairs, one of which is at a lower inclination, thus adding East-West information to the observable and reducing correlations between coefficients [*Bender et al.*, 2008].

1.5 Previous Investigations of Future Missions

Due to the success of the GRACE mission, there has been considerable interest in exploring mission architectures for the next generation of missions dedicated to measuring time variable gravity. A comprehensive analysis by *Loomis et al.* [2010] explored on a regional level the benefit that flying a collinear formation (similar to GRACE) drag-free with a laser interferometer would provide in determining temporal gravity variations. It was found that with the improved instrumentation suite, extremely minor improvements in performance were found over what the current GRACE mission provides. Temporal aliasing errors were shown to be the limiting source of error, agreeing with the results presented in Figure 1.2.

Several authors have studied the idea of flying a different satellite formation, rather than the

collinear formation that GRACE employs. The benefit to an alternate formation is that measurements in more than one direction could be made, thus enhancing the information in the observable and reducing the longitudinal striping. *Sneeuw and Schaub* [2005] discussed the formation dynamics assosiated with possible alternate formations, including the cartwheel formation, pendulum formation, and a LISA-type formation. In the cartwheel formation, the satellite orbits are designed such that they perform relative 2:1 elliptical motion in the radial/alongtrack plane of the satellite's motion. Hence, one gains measurements in the alongtrack as well as the radial directions. In a pendulum formation, the satellites are slightly offset from each other in the node as well as mean anomaly, creating a formation where measurements are made in the crosstrack and alongtrack directions. Both of these formations were shown to be stable over long time periods. The LISA-type formation was shown to be unstable; hence, it will not be discussed here.

Building upon this work, *Sharifi et al.* [2007], *Sneeuw et al.* [2008], and *Encarnacao et al.* [2008] ran numerical simulations comparing each formation type, contaminating the observations with realistic noise levels. The results from each study were consistent in that the cartwheel and pendulum formations were shown to have lower errors, more isotropic error spectrums, and reduce the level of striping in the solutions. While the results from these studies were promising, they did not account for temporal aliasing errors in the numerical simuations. A study by *Wiese et al.* [2009] expanded upon this work, comparing the abilities of the cartwheel and collinear formations in recovering temporal gravity variations in the presence of temporal aliasing errors due to mismodelling of atmosphere and ocean mass variations. This study also assumed that the spacecraft took advantage of new technologies (i.e. flying drag-free with a laser interferometer). The results showed that while the cartwheel formation did reduce the longitudinal striping in the solutions, the overall level of errors between the two formations were equal. The conclusion was that while the cartwheel formation does offer improved sensitivity to gravity variations, the formation dynamics do not aid in reducing the level of temporal aliasing errors.

A more recent study by *Elsaka* [2010] offered the most comprehensive analysis of different formation types and their abilities to detect temporal gravity variations. Temporal aliasing errors from

all sources were considered in the study (hydrology, atmosphere, ocean, tides), along with different levels of instrument noise. A cartwheel, pendulum, collinear, and a combined collinear-pendulum formation consisting of three satellites was explored. The results differed from *Wiese et al.* [2009] in that the different formation types were shown to provide improvements in determining gravity variations even when temporal aliasing errors were considered. The reason for the discrepancy between the results could result from two factors: (1) different models were used to define temporal aliasing errors, and (2) the two studies used completely different solution strategies to solve for gravity variations. Preliminary investigations into the discrepancies suggest that the differences in results arise primarily because of (2). *Elsaka* [2010] used a short-arc method developed at the University of Bonn in which data is accumulated in 30 minute arcs, to avoid build-up of unmodeled disturbances, such as temporal aliasing errors. Conversely, *Wiese et al.* [2009] used daily arcs of data, similar to the processing that is employed at other GRACE processing centers including the Center for Space Research (CSR), GeoForschungsZentrum (GFZ), Jet Propulsion Laboratory (JPL), and Goddard Space Flight Center (GSFC). Currently, it appears that the short-arc method reduces the accumulation of temporal aliasing errors, allowing one to take advantage of the improved dynamics that other formations offer. This conclusion is still under investigation, however.

In addition to being more technologically challenging to implement, flying different satellite formations also have the common disadvantage of having the same temporal sampling characteristics as a collinear formation given the same number of satellite pairs. From *Dirac* [1958], the Heisenburg uncertainty principle of spatio-temporal sampling states that the product of spatial sampling and temporal sampling is a constant; that is, one cannot gain better spatial resolution without sacrificing temporal resolution and vice-versa. The only way to improve both simultaneously is to add additional satellite pairs, which was demonstrated in *Reubelt et al.* [2008]. The concept of adding an additional pair of collinear satellites in a polar orbit was explored in *Wiese et al.* [2009], *Elsaka* [2010], and *Visser et al.* [2010]. Each study showed that temporal aliasing errors were reduced; however, longitudinal stripes still dominated the solutions.

[*Bender et al.*, 2008] first suggested the idea of having a polar pair of satellites coupled with

a lower inclined pair of satellites. The advantage to such an architecture is three-fold: (1) the temporal resolution of the mission is increased, (2) the addition of the lower inclined pair adds East-West information to the observable which should reduce the longitudinal striping, and (3) the groundtrack pattern of such an architecture is more homogeneous than an architecture consisting of only polar pairs of satellites. The study by *Visser et al.* [2010] explored the option of having such an architecture; with a polar-orbiting pair in a 5-day repeat period coupled with a lower inclined pair at 117^o in a 23-day repeat period. The results averaged over shorter time periods were encouraging from this formation. However, this study was limited in the sense that it was a point case study; examining only a single architecture of this type, and did not attempt to optimize such an architecture. Additionally, it focused solely on temporal aliasing errors from ocean tides.

1.6 Project Overview

In April of 2007, a workshop on the future of satellite gravimetry was held in Noordwijk, Netherlands, from which several conclusions and recommendations were reached. One of the resolutions reads: "Medium term priority should be focused on higher precision and higher resolution in space and time. This step requires (1) the reduction of the current level of aliasing (of high frequency phenomena, in particular tides, into the time series), (2) the elimination of systematic distortions (caused by the peculiar non-isotropic sensitivity of a single pair low-low SST), and (3) the improvement of the separability of the observed geophysical signals" [*Koop and Rummel*, 2007]. This resolution, coupled with the results from previous studies discussed above, have given direction to this dissertation.

The main goal of this resarch project is to reduce temporal aliasing errors through the use of multiple satellite pairs in a collinear formation. In the process of doing so, we aim to show that the "systematic distortions" (longitudinal stripes) can also be reduced. While one could theoretically reduce temporal aliasing errors to near-zero by flying dozens, if not more, pairs of satellites (although the problem of signal separation would still exist given this scenario), this option is, of course, cost-prohibitive at the moment. As such, we study the more economically feasible option of optimizing

the orbits given two pairs of satellites, and quantifying the expected improvements in determining geophysical signals of interest (hydrology, ice mass variations, ocean bottom pressure variations, earthquakes). Additionally, alternate processing methodologies are explored in an effort to further reduce temporal aliasing errors.

The remainder of this dissertation is divided into six additional chapters. A brief description of the contents of each chapter is listed below. Additionally, this work has been compiled into three journal articles: *Wiese et al.* [2011c] corresponding to Chapter 4, *Wiese et al.* [2011b] corresponding to Chapter 5, and *Wiese et al.* [2011a] corresponding to Chapter 6.

- *Chapter 2* - This chapter contains the mathematical foundation necessary for describing the Earth's gravity field in terms of spherical harmonic coefficients. Mathematical descriptions of the performance metrics (both globally and regionally) used in this study are provided.

- *Chapter 3* - This chapter contains definitions of the measurement system errors used in this study as well as temporal aliasing errors. Details of the numerical simulation process are given. All models (hydrology, ice, atmosphere, ocean, tides) are defined in this chapter.

- *Chapter 4* - This chapter discusses an alternate processing methodology in which low resolution gravity fields are estimated at high frequencies in an effort to reduce temporal aliasing errors is explored. The effectiveness of this process is quantified for the case of a single pair of satellites, two polar pairs of satellites, and a polar pair of satellites coupled with a lower inclined pair of satellites.

- *Chapter 5* - This chapter deals with the process of optimizing a mission architecture consisting of two pairs of collinear satellites. A Monte-Carlo analysis of numerical simulations is used reduce the search space, and appropriate mission architectures are recommended.

- *Chapter 6* - This chapter quantifies the expected scientific improvements in recovering hydrology, ice mass variations, ocean bottom pressure signals, and earthquakes that having a near-optimal architecture consisting of two satellite pairs provides over a one-pair architecture. Results are analyzed on global and regional scales.

- *Chapter 7* - This chapter provides a summary of the dissertation, including recommendations.

Chapter 2

Theory

2.1 Introduction

This chapter provides a mathematical formulation of the Earth's gravity field in terms of spherical harmonic functions, along with definitions necessary to understand the results shown in this work. Definitions of global and regional analysis techniques used to quantify mission performance are also provided.

2.2 Definitions

This section of text contains definitions necessary to understand the results presented in this dissertation. Included in this section are a mathematical representation of spherical harmonic functions used to represent the Earth's gravity field along with mathematical definitions for the geoid as well as surface mass density, two quantities which are useful to characterize temporal gravity variations.

2.2.1 Spherical Harmonics

The Earth's gravitational field is traditionally expressed in spherical harmonics. This notation is convenient and natural due to the shape of the Earth. This section provides a brief introduction to spherical harmonics. For a more detailed derivation and discussion, the reader is referred to *Kaula* [1966]; *Seeber* [2003]; *Torge* [2001].

For any point mass outside the surface of the Earth, the gravitational potential, V, of the object must be satisified by LaPlace's equation [*Kaula*, 1966]:

$$\nabla^2 V = \frac{\partial^2 V}{\partial x^2} + \frac{\partial^2 V}{\partial y^2} + \frac{\partial^2 V}{\partial z^2} = 0. \tag{2.1}$$

Equation 2.1 is expressed in cartesian coordinates. It is much more natural to work in spherical coordinates given the shape of the Earth. The conversion from cartesian to spherical coordinates is given by the following:

$$\begin{aligned} x &= r\cos\phi\cos\lambda, \\ y &= r\cos\phi\sin\lambda, \\ z &= r\sin\phi, \end{aligned} \tag{2.2}$$

where r is the distance from the center of mass of the Earth to the point mass, ϕ is the latitude, and λ is the longitude. Figure 2.1 gives a graphical representation of the Earth-Centered-Earth-Fixed (ECEF) coordinate system described in spherical coordinates.

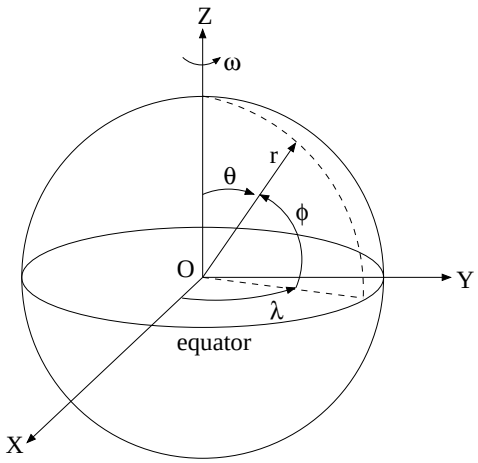

Figure 2.1: ECEF frame in spherical coordinates

Using the relationships in Equation 2.2, LaPlace's equation can be rewritten in spherical coordinates as

$$\nabla^2 V = \frac{1}{r^2}\frac{\partial}{\partial r}\left(r^2\frac{\partial V}{\partial r}\right) + \frac{1}{r^2\cos\phi}\frac{\partial}{\partial\phi}\left(\cos\phi\frac{\partial V}{\partial\phi}\right) + \frac{1}{r^2\cos^2\phi}\frac{\partial^2 V}{\partial\lambda^2} = 0. \tag{2.3}$$

To solve Equation 2.3 for the gravitational potential, V, it would be convenient if V had the form (separation of variables)

$$V = R(r)\,\Phi(\phi)\,\Lambda(\lambda)\,. \tag{2.4}$$

Assuming the solution has this form, and after many mathematical steps, one ultimately finds that the gravitational potential can be expressed as [*Seeber*, 2003]

$$V = \frac{GM}{r}\left(1 + \sum_{n=1}^{\infty}\sum_{m=0}^{n}\left(\frac{r_E}{r}\right)^n P_{nm}(\sin\phi)(C_{nm}\cos m\lambda + S_{nm}\sin m\lambda)\right). \tag{2.5}$$

In Equation 2.5, $P_{nm}(\sin\phi)$ are the associated Legendre functions, C_{nm} and S_{nm} are the spherical harmonic coefficients, r_E is the radius of the Earth, G is the gravitational constant, and M is the mass of the Earth. Note that n and m are the degree and order, respectively, of the spherical harmonic coefficients.

The associated Legendre functions can be calculated using the following [*Kaula*, 1966]:

$$P_{nm}(\sin\phi) = \cos^m\phi\sum_{t=0}^{k} T_{nmt}\sin^{n-m-2t}\phi, \tag{2.6}$$

where

$$T_{nmt} = \frac{(-1)^t(2n-2t)!}{2^n t!\,(n-t)!\,(n-m-2t)!}, \tag{2.7}$$

and k is the integer part of $(n-m)/2$.

In Equation 2.5, the geopotential coefficients C_{nm} and S_{nm} are referred to as unnormalized gravity field coefficients. The Legendre associated functions are also unnormalized. It is conventional practice to define and use a set of fully normalized geopotential coefficients and fully normalized associated Legendre functions. These are defined as [*Torge*, 2001]:

$$\overline{P}_{nm}(\sin\phi) = \left[\frac{k(2n+1)(n-m)!}{(n+m)!}\right]^{1/2} P_{nm}(\sin\phi), \tag{2.8}$$

$$\begin{Bmatrix}\overline{C}_{nm}\\ \overline{S}_{nm}\end{Bmatrix} = \left[\frac{(n+m)!}{k(2n+1)(n-m)!}\right]^{1/2}\begin{Bmatrix}C_{nm}\\ S_{nm}\end{Bmatrix}, \tag{2.9}$$

with $k = 1$ for $m = 0$, and $k = 2$ for $m \neq 0$.

Substituting the normalized definitions into Equation 2.5, the gravitational potential can be expressed as

$$V = \frac{GM}{r}\left(1 + \sum_{n=1}^{\infty}\sum_{m=0}^{n}\left(\frac{r_E}{r}\right)^n \overline{P}_{nm}(\sin\phi)(\overline{C}_{nm}\cos m\lambda + \overline{S}_{nm}\sin m\lambda)\right). \tag{2.10}$$

Possibly the most important property of spherical harmonics is that they are orthogonal to each other [*Kaula*, 1966], making them the natural means for representing a function over a spherical surface. This orthogonality can best be seen by defining different types of spherical harmonics. When the order $m = 0$, the harmonics are referred to as *zonal harmonics*. For $m > 0$, $m \neq n$, they are referred to as *tesseral harmonics*, and when $m = n$, they are called *sectorial harmonics* [*Torge*, 2001]. Figure 2.2 shows the three types of harmonics graphically.

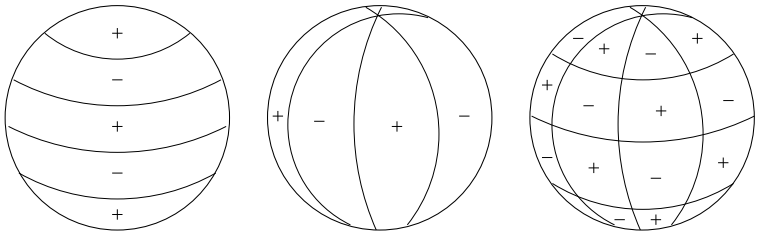

Figure 2.2: Examples of harmonic types: (i)Zonal (ii)Sectorial (iii)Tesseral.

Figure 2.2 shows that any geopotential coefficient, C_{nm}, has $n - m$ zeroes, or nodal lines of latitude, in a distance π along a meridian. Additionally, it will have exactly m zeroes in the same distance along the line of latitude; that is, it has m nodal lines of longitude along a distance π measured around a line of latitude. For example, in Figure 2.2, the C_{40} coefficient is the zonal harmonic example, the C_{33} coefficient is the sectorial harmonic example, and the tesseral harmonic example is given by the C_{63} coefficient.

2.2.2 Geoid Definition

The geoid is defined as a surface of constant potential energy which coincides with mean sea level over the oceans. The height of the geoid, N, is defined with respect to a reference ellipsoid, as seen in Figure 2.3.

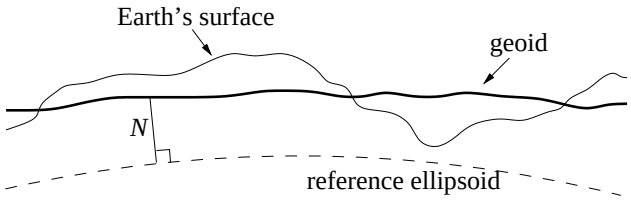

Figure 2.3: Definition of the geoid height N

Note that the geoid does not coincide with the Earth's surface, but can lie above or below it depending on the potential energy at the location of interest. The reference ellipsoid, which describes to first order the shape of the Earth, is described with a flattening coefficient given by

$$f = \frac{a-b}{a}, \tag{2.11}$$

where a and b are the equatorial radius and polar radius, respectively. The current accepted value of f is 1/298.257 [*Vallado*, 2001].

Remember that potential energy at any point on the reference ellipsoid, or on the geoid, is defined by both the gravitational potential energy (V) as well as the potential energy associated with the rotation of the Earth. The absolute potential energy, called the potential of gravity, is defined as [*Kaula*, 1966]

$$W(r,\phi,\lambda) = V(r,\phi,\lambda) + \frac{1}{2}\omega^2 r^2 \cos^2\phi, \tag{2.12}$$

where ω is the rotation rate of the Earth.

The potential associated with the reference ellipsoid is defined as the normal potential, U_P, while the potential on the geoid is defined as the actual potential, or potential of gravity, W_P. One can then define a disturbing potential, T_P, as the difference between the actual potential and the normal potential, [*Torge*, 2001],

$$T_P = W_P - U_P. \tag{2.13}$$

Since both W_P and U_P have the same rotational term in them (seen in Equation 2.12), this term differences out and the disturbing potential is given by [*Torge*, 2001]

$$T_P = \frac{GM}{r}\sum_{n=2}^{\infty}\sum_{m=0}^{n}\left(\frac{r_E}{r}\right)^n \overline{P}_{nm}(\sin\phi)(\overline{C}^*_{nm}\cos m\lambda + \overline{S}_{nm}\sin m\lambda), \tag{2.14}$$

with

$$\overline{C}^{*}_{nm} = \overline{C}^{obs}_{nm} - \overline{C}^{ref}_{nm}.$$

The $\overline{C}^{ref}_{nm}$ values are the spherical harmonic coefficients of the reference ellipsoid. The reference ellipsoid is often defined using only $\overline{C}_{20}$, $\overline{C}_{40}$, and $\overline{C}_{60}$, but additional zonal terms can be included if desired. Note that Equation 2.14 assumes the origin of the coordinate system has been placed at the center of mass of the Earth, as this makes all $n = 1$ terms go to zero.

The geoid height, N, can then be calculated from the disturbing potential by [*Torge*, 2001]

$$N = \left.\frac{T_P}{\gamma}\right|_{r=r_E}, \tag{2.15}$$

where

$$\gamma = \frac{GM}{r^2}. \tag{2.16}$$

Note that this definition for γ uses a spherical approximation for the Earth, but in reality, γ is taken from the reference ellipsoid.

Finally, evaluating Equation 2.15 gives the definition for geoid height as [*Torge*, 2001]

$$N = r_E \sum_{n=2}^{\infty} \sum_{m=0}^{n} \overline{P}_{nm}(\sin\phi)(\overline{C}^{*}_{nm} \cos m\lambda + \overline{S}_{nm} \sin m\lambda). \tag{2.17}$$

In practice, one would not sum to infinity, but to some finite value of $n = n_{max}$ in Equation 2.17.

A primary goal of this project is to determine time variations in the Earth's gravity field. The change in gravitational signal from one time to the next, can be expressed in terms of geoid height as

$$\Delta N = r_E \sum_{n=2}^{\infty} \sum_{m=0}^{n} \overline{P}_{nm}(\sin\phi)(\Delta\overline{C}_{nm} \cos m\lambda + \Delta\overline{S}_{nm} \sin m\lambda). \tag{2.18}$$

Note that the denotation for the reference ellipsoid has dropped since it will difference out from one time to the next.

2.2.3 Surface Mass Density

Equation 2.18 expresses changes in the Earth's gravity field in terms of geoid height. A more common way to express these changes is in terms of surface mass density. Assume that a change

in geoid, given by Equation 2.18, is caused by a density redistribution $\Delta\rho(r,\phi,\lambda)$ concentrated in a thin layer of thickness H at the Earth's surface. For applications to the GRACE data, this layer must be thick enough to include all significant mass variations, including ground water storage, ice caps, atmosphere, and oceans. A typical thickness for this layer would be on the order of 10-15 km. The change in surface density, $\Delta\sigma$, can then be defined as [*Wahr et al.*, 1998]

$$\Delta\sigma(\phi,\lambda) = \int_{layer} \Delta\rho(r,\phi,\lambda)dr. \tag{2.19}$$

Assuming that $(n_{max}+2)H/r_E << 1$, and recognizing that the change in geoid comes not only from the gravitational attraction of the surface mass, but also from the elastic response of the Earth deforming to the load, it can be shown that [*Wahr et al.*, 1998]

$$\Delta\sigma(\phi,\lambda) = \frac{r_E\rho_E}{3}\sum_{n=0}^{\infty}\sum_{m=0}^{l}\frac{2n+1}{1+k_n}\overline{P}_{nm}(\sin\phi)(\Delta\overline{C}_{nm}\cos m\lambda + \Delta\overline{S}_{nm}\sin m\lambda) \tag{2.20}$$

In Equation 2.20, ρ_E is the average density of the Earth, and k_n are the elastic Love numbers as computed by *Han and Wahr* [1995] describing the deformation of the solid Earth to a load. Finally, it is common to express changes in gravity in terms of equivalent water height (EWH). The change of surface mass in terms of EWH is simply $\Delta\sigma/\rho_w$, where ρ_w is the density of water (assumed to be 1000 kg/m^3).

2.3 Analysis Techniques

There are a variety of tools which can be used to analyze GRACE data. This section of text describes the tools used in this paper, for both global and regional analysis.

2.3.1 Global Techniques

2.3.1.1 Geoid Degree Error

This study quantifies gravity field errors globally using a geoid degree difference, which allows for easy comparison of results. One can first define a degree difference variance as [*Kim*, 2000]

$$\sigma_n^2(\Delta) = \sum_{m=0}^{n}(\Delta\overline{C}_{nm}^2 + \Delta\overline{S}_{nm}^2) \tag{2.21}$$

where

$$\Delta\overline{C}_{nm} = (\overline{C}_{nm})_{estimate} - (\overline{C}_{nm})_{truth},$$
$$\Delta\overline{S}_{nm} = (\overline{S}_{nm})_{estimate} - (\overline{S}_{nm})_{truth}.$$

Note that the degree difference variance is only valid for simulations, as the truth cannot be known in reality.

For this study, it is useful to present the errors in terms of geoid height. Multiplying the degree difference variance given in Equation 2.21 by the square of the radius of the Earth, r_E, forms the geoid degree difference variance, given as [*Torge*, 2001]

$$\sigma_n^2(\Delta N) = r_E^2\sigma_n^2(\Delta) = r_E^2\sum_{m=0}^{n}(\Delta\overline{C}_{nm}^2 + \Delta\overline{S}_{nm}^2). \tag{2.22}$$

It is furthermore useful to present this error in units of length, thus requiring one to take the square root of Equation 2.22. The expression for the geoid degree difference, ΔN_n is then defined as

$$\Delta N_n = \sqrt{\sigma_n^2(\Delta N)} = r_E\sqrt{\sum_{m=0}^{n}(\Delta\overline{C}_{nm}^2 + \Delta\overline{S}_{nm}^2)}. \tag{2.23}$$

Equation 2.23 is used to create geoid degree error plots for this study. This analysis allows one to quantify the amount that each degree contributes to the geoid height error. Alternately, one can also express the errors as a function of order, rather than degree, using a slightly modified expression as that in 2.23.

2.3.1.2 Spatial RMS

The geoid degree difference, given in Equation 2.23 represents the errors of the gravity field in the spectral domain. The end users of the GRACE data are typically more interested in what is happening in the spatial domain; i.e. the accuracy to which certain geophysical signals are being determined. As such, it is useful to define a global performance metric in the spatial domain. A rather rudimentary, but effective method of doing so, is to define a spatial RMS. This is simply done by differencing a spatial plot of the recovered signals from a spatial plot of the truth signals,

creating a spatial plot of errors. The spatial RMS is then calculated simply by taking the RMS of the spatial plot of errors, given a predefined grid (such as $1^o \times 1^o$), and weighting by area.

2.3.1.3 Empirical Orthogonal Functions

Several studies have made use of empirical orthogonal functions (EOFs) to analyze GRACE data. In a general sense, EOFs are used to capture the dominant modes of a time series of data, both spatially and temporally. Given a time series with N points and M spatial locations, we define a matrix Z with M columns and N rows, where

$$Z = A\zeta^{1/2}E^T. \tag{2.24}$$

In Equation 2.24, A is a matrix with the principal components (the time part) and E is a matrix with the eigenfunctions, or basis functions (the space part). ζ is a diagonal matrix with the main diagonal elements being the eigenvalues, and are proportional to how much variance is carried by each basis function.

We can now define a scatter matrix, S, as [*Preisendorfer*, 1988]

$$S = Z^T Z = E\zeta^{1/2}A^T A\zeta^{1/2}E^T = E\zeta E^T. \tag{2.25}$$

This is a well-known eigenvalue problem, and one can easily solve for E and ζ, given this equation. Once E is obtained, the principal components, A, can be solved for via substitution into Equation 2.24.

As such, given a time series of spatial gravity field maps, one can solve for the dominant spatial modes (given by E), along with the respective time signatures of the modes (given by A). The percent variance that each mode captures is provided by ζ.

2.3.2 Regional Techniques

While global analyses are useful for a first-order approximation of performance, they are insufficient by themselves, as they disregard the different spatial distributions of signals and errors,

as pointed out by *Han and Ditmar* [2008]. As such, regional analyses are necessary to more accurately quantify the expected mission performance. While there are a host of techniques available to perform regional analyses, the two used in this dissertation are averaging kernels and spatiospectral localization.

2.3.2.1 Averaging Kernels

Averaging kernels are traditionally used to quantify mass variations in a region of interest over a specified amount of time. From *Swenson and Wahr* [2002], an exact averaging kernel representing the shape of a basin is given by

$$\vartheta(\phi,\lambda) = \begin{cases} 0 \text{ outside the basin} \\ 1 \text{ inside the basin} \end{cases} \tag{2.26}$$

One can then represent the change in vertically integrated water storage over a region as

$$\overline{\Delta\sigma}_{region} = \frac{1}{\Omega_{region}} \int \Delta\sigma(\phi,\lambda)\vartheta(\phi,\lambda)d\Omega, \tag{2.27}$$

where Ω is the area of the region. Substituting the expression for surface density from Equation 2.20 into Equation 2.27, the average surface mass density over a region is given by [*Swenson and Wahr*, 2002]

$$\overline{\Delta\sigma}_{region} = \frac{r_E\rho_E}{3\Omega_{region}} \sum_{n=0}^{\infty}\sum_{m=0}^{n} \frac{2n+1}{1+k_n}(\vartheta^c_{nm}\Delta\overline{C}_{nm} + \vartheta^s_{nm}\Delta\overline{S}_{nm}) \tag{2.28}$$

where ϑ^c_{nm} and ϑ^s_{nm} are the spherical harmonic coefficients describing $\vartheta(\phi,\lambda)$, given by

$$\vartheta(\phi,\lambda) = \frac{1}{4\pi}\sum_{n=0}^{\infty}\sum_{m=0}^{n} \overline{P}_{nm}(\sin\phi)(\vartheta^c_{nm}\cos m\lambda + \vartheta^s_{nm}\sin m\lambda) \tag{2.29}$$

$$\begin{Bmatrix} \vartheta^c_{nm} \\ \vartheta^s_{nm} \end{Bmatrix} = \int \vartheta(\phi,\lambda)\overline{P}_{nm}(\sin\phi) \begin{Bmatrix} \cos m\lambda \\ \sin m\lambda \end{Bmatrix} d\Omega. \tag{2.30}$$

In practice, one would not sum n to ∞ in Equation 2.28, but rather would truncate at some specific degree, n_{max}. Truncating introduces an error, as not including all values of n results in an inaccurate representation of the basin shape, and causes ringing around the boundaries of the

basin known as the Gibbs phenomenon. Alternately, one can define an approximate averaging kernel, W, by replacing ϑ^c_{nm} and ϑ^s_{nm} in Equation 2.28 with W^c_{nm} and W^s_{nm}. This new kernel can be computed a variety of ways; *Swenson and Wahr* [2002] compute it using Gaussian smoothing as well as with a Legendre multiplier method. The disadvantage to introducing an approximate averaging kernel, given by W, is that while it does decrease truncation error by suppressing short wavelength coefficients, it introduces leakage error into the solution. In this study, we use both exact averaging kernels and Gaussian smoothed averaging kernels.

2.3.2.2 Spatiospectral Localization

The principle behind spatiospectral localization is simply to apply an isotropic windowing function that maximizes the ratio of energy of the function within the defined region of interest to that of the entire sphere to obtain a localized representation of the signal. In general, we wish to solve for a localized version ($y(\Omega)$) of a global signal ($f(\Omega)$) given by the following

$$y\left(\Omega\right) = h\left(\phi\right) f\left(\Omega\right), \tag{2.31}$$

where $h(\phi)$, is an optimal zonal windowing function. The spherical harmonic coefficients describing $y(\Omega)$ are given by *Wieczorek and Simons* [2005] as

$$y_{nm} = \sum_{j=0}^{N_h} \sum_{i=|n-j|}^{n+j} h_j f_{im} \sqrt{\left(2i+1\right)\left(2j+1\right)\left(2n+1\right)} \left(-1\right)^m \begin{pmatrix} i & j & n \\ 0 & 0 & 0 \end{pmatrix} \begin{pmatrix} i & j & n \\ m & 0 & -m \end{pmatrix}. \tag{2.32}$$

The matrix symbols in parentheses in Equation 2.32 are Wigner 3-j functions. The only unknown parameter in Equation 2.32 is the term h_j which are the coefficients of the windowing function, and it is left to the user to define an optimal set. *Wieczorek and Simons* [2005] elaborate on how to choose an optimal windowing funtion. It is done by maximizing the value ψ, which defines the ratio of energy of the function within the region of interest (whose area is given by Ω_o) to the energy over the entire sphere, given by

$$\psi = \int_{\Omega_o} h^2\left(\Omega\right) d\Omega \Big/ \int_{\Omega} h^2\left(\Omega\right) d\Omega. \tag{2.33}$$

The solution for ψ is attained by solving for the eigenvalues of a matrix given by Equation 13 in *Wieczorek and Simons* [2005]. The matrix ultimately depends on user-selected values for the radius of the spherical cap, θ_o, along with the maximum degree of expansion, N_h. A Shannon number given by N_o is defined as [*Han and Ditmar*, 2008]

$$N_o = (N_h + 1)\,\frac{\theta_o}{\pi}. \tag{2.34}$$

It is important to choose N_h and θ_o such that N_o is close to 2, since typically $N_o - 1$ gives the number of well-concentrated windows.

Furthermore, one can calculate the localized degree-RMS using the calculated coefficients $\overline{C}^y_{nm}$ and $\overline{S}^y_{nm}$ which describe y_{nm} by [*Han and Ditmar*, 2008]

$$V^y(n) = \sqrt{\sum_{m=0}^{n} (\overline{C}^y_{nm})^2 + (\overline{S}^y_{nm})^2}. \tag{2.35}$$

Multiplying Equation 2.35 by r_E gives a localized geoid degree error, similar in representation to Equation 2.23. It is important to note that the range of permissible values for the localized coefficients is limited to $n_{max} - N_h$; thus, the spatial resolution is decreased by the degree of expansion of the windowing function. Additionally, degrees lower than N_h have the potential to carry a significant bias, as discussed in *Wieczorek and Simons* [2005] in Section 5.1. As such, it is optimal to choose small values for N_h, which means this technique is particularly useful for examining mass variations with large spatial scales. It has also be shown to be effective in studying earthquake signals [*Han and Ditmar*, 2008]. For more details on the spatiospectral localization technique, the reader is referred to *Wieczorek and Simons* [2005]; *Simons et al.* [2006]; *Han and Ditmar* [2008]; *Han and Simons* [2008].

Chapter 3

Simulation Procedure and Model Definitions

3.1 Introduction

Numerical simulations are necessary to compare the expected performance of each mission architecture in recovering the gravity field. This chapter discusses measurement system errors introduced in the simulation, the different hydrology, ice, tide, atmosphere, and ocean models used in the simulations, and the simulation procedure itself. The simulations are performed using GEODYN [*Pavlis et al.*, 2010], a precise orbit determination and geodetic parameter estimation software package, SOLVE [*Ullman*, 1997], a large linear systems solver, and solvepa, a modified version of SOLVE. GEODYN and SOLVE have been provided by NASA Goddard Space Flight Center while solvepa has been provided by the Department of Earth Observation and Space Systems (DEOS) at TU Delft University.

3.2 Measurement System Errors

As discussed in Section 1.4, there are four primary sources of measurement error associated with GRACE: the inter-satellite range measurement, the measurement of non-conservative forces acting on the spacecraft, the measurement of the satellite positions, and the measurement of the attitude of the spacecraft. This section discusses the errors assumed for each of these measurements except for the measurement of the spacecraft attitude. It was not realized until recently [*Horwath et al.*, 2011; *Bandikova et al.*, 2010] that this could be a limiting source of error, and as such, it has been disregarded from this study.

All simulations assume that the spacecraft fly drag-free and perform inter-satellite ranging with a laser interferometer. Given this scenario, it has been shown that temporal aliasing errors dominate the error budget [*Loomis et al.*, 2010] (see also Figure 1.2). Hence, any improvements that certain architectures offer over other architectures in this study can be attributed to lowering the level of temporal aliasing errors, which is the ultimate goal of this study.

The laser interferometer instrument would replace the microwave ranging system currently used by GRACE. The design and testing of a laser ranging system which could be used for a follow-on mission has been completed through NASA's Instrument Incubator Program. The instrument is now classified as Technology Readiness Level (TRL) 6, meaning a prototype has been developed and tested in a relevant environment. The dominant error source associated with the laser interferometer is the laser frequency noise [*Pierce et al.*, 2008].

Another major source of error is the measurement of non-gravitational forces acting on the spacecraft which must be removed when processing the data. As mentioned in Section 1.3, GRACE measures these forces using an accelerometer. Alternately, it has been proposed that future missions could fly drag-free, such that non-conservative forces acting on the spacecraft are measured and compensated for in real-time, similar to how the GOCE mission operates. This technique generally results in lower residual accelerations versus having an accelerometer onboard the spacecraft. For this study we assumed the use of drag-free technology similar to that of the GOCE mission.

Figure 3.1 shows the power spectrum of the laser frequency noise and errors from the drag-free system plotted as range-rate displacements. Note that the orbit frequency shown in the plot corresponds to an altitude of 300 km, and the maximum frequency in the recovered gravity field corresponds to degree 60. Errors from the drag-free system are shown to dominate at lower frequencies while the laser frequency noise dominates at high frequencies.

The laser frequency noise shown in Figure 3.1 is derived primarily from laser frequency stabilization work done for LISA [*Mueller et al.*, December 2005]. For a 100 km separation distance in spacecraft, *Mueller et al.* [December 2005] showed a frequency independent noise level of 10 $nm/\sqrt{Hz}$ down to 0.001 Hz, and an inverse relationship to frequency for lower frequencies. More

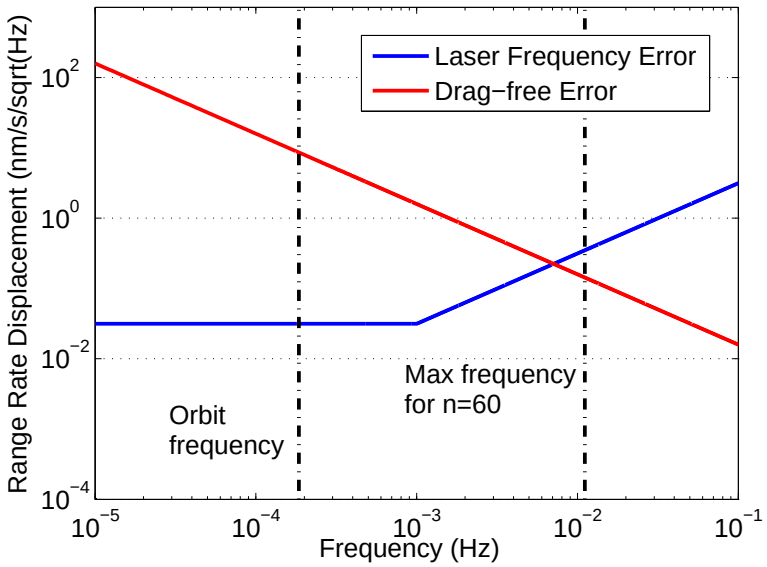

Figure 3.1: Power spectrum of measurement system errors used in simulations

recent experiments have shown laser performance more than an order of magnitude better than *Mueller et al.* [December 2005] [*Alnis et al.*, 2008]. We use a frequency independent laser frequency noise in range of 5 $nm/\sqrt{Hz}$ down to 0.001 Hz, and include the inverse correlation to frequency due to thermal effects at low frequencies. This level of error is between *Mueller et al.* [December 2005] and *Alnis et al.* [2008]. The drag-free error curve is taken such that the error is commensurate with what GOCE experiences (*Fehringer, 2010, personal communication*), and is given by .01 $nm/s^2/\sqrt{Hz}$. Note that this error is approximately two orders of magnitude higher than what is targeted for the drag-free system being implemented on the LISA Pathfinder mission [*Dolesi et al.*, 2003].

This power spectrum of range-rate errors in Figure 3.1 has to be converted to the time domain for the simulations. To accomplish this, a frequency spectrum is defined as

$$f_l = l\Delta f, \qquad l = 1, 2, ..., N \tag{3.1}$$

where

$$\Delta f = \frac{1}{2N\Delta t} \tag{3.2}$$

is the frequency sampling rate. In Equation 3.2, N is the number of data points in the time series, and Δt is the sampling rate in the time domain. Note that N is given by the desired time period, T, divided by the sampling rate, Δt. The frequency spectrum has been defined such that all frequencies are positive.

The power spectral density functions shown in Figure 3.1 are then evaluated at each discrete frequency, multiplied by the square root of T, and divided by the sampling rate, Δt. We divide by Δt because we are using a discrete Fourier transform, and we multiply by T because the power spectral density function has previously been divided by T. Each point is then multiplied by $e^{i\phi}$ where ϕ is a random phase in the range from $[-\pi, \pi]$ [*Ebisuzaki*, 1997]. Since a real time series is desired, only the real part of this is kept, and an inverse Fourier transform is performed to convert it to the time-domain. Thus, a time-series of range-rate measurement errors is created. The RMS of the time-series of simulated measurement errors is 4.72 nm/s. It should be mentioned that the errors from the drag-free system dominate the error budget by approximately one order of magnitude.

Furthermore, errors in the spacecraft position are introduced in the simulation by adding 1 cm RMS white noise to each directional component of the spacecraft position. This is the same level of error that GRACE orbits are known to. This is a simplistic method of introducing error in GPS measurements without the need to model all GPS satellites and estimate parameters such as clock biases and drifts, as is necessary with the real GRACE data.

3.3 Model Definitions and Aliasing Errors

Since GRACE requires on average 30 days of data for global coverage (in reality this number depends on the desired spatial resolution and the evolution of the orbit since it is a non-repeating groundtrack), mass variations with time scales shorter than 60 days are undersampled via the Nyquist Sampling Theorum. There are six primary sources for high frequency mass variations within the Earth system: tides(ocean and atmosphere), atmosphere, ocean, continental hydrology, and ice mass variations. The non-tidal high frequency mass variations in the atmosphere and ocean

are caused by weather systems on Earth (i.e. redistribution of atmospheric pressure).

One should think of GRACE as giving a picture of total mass movement about the Earth. Thus, a hydrologist who is only interested in how hydrology changes over time, will want to remove the effects of tides and atmosphere and ocean. For GRACE data, these unwanted short period mass variations are accounted for by using models fit to atmosphere and ocean observations, and subtracting them from the GRACE estimates. Any errors in these models then alias into the 30-day gravity field solutions. Aliasing is considered to be one of the largest error sources for the GRACE mission [*Thompson et al.*, 2004; *Han et al.*, 2004; *Zenner et al.*, 2010]. There are several models available which can be used to remove the effects of high frequency mass variations. We assume that the difference between these models is representative of their error.

Atmosphere/ocean (AOD) models (independent of tides) are created by combining both an atmospheric and an ocean model [*Flechtner*, 2007]. The two different atmospheric models which are used in this study are the 3-hr European Center for Medium-range Weather Forecast (ECMWF) surface pressure fields, and the 6-hr National Center for Environmental Predictions (NCEP) Reanalysis fields [*Kalnay et al.*, 1996]. The two different ocean models which are used in this study are the 6-hr baroclinic Ocean Model for Circulation and Tides (OMCT) which is currently used as a dealiasing product for GRACE, and the 6-hr MOG2D model [*Carrère and Lyard*, 2003], both of which are forced by ECMWF surface pressure. These models are represented via spherical harmonic coefficients. In the simulations, the difference between (ECWMF + OMCT) and (NCEP + MOG2D) is representative of the aliasing error given by AOD models.

The two tide models used in this study are FES2004 and GOT00. The Finite Element Solution (FES2004) tide model is a hydrodynamic model that is computed using tide gauge data and TOPEX/Poseiden satellite altimetry data [*Lyard et al.*, 2006]. The Goddard Ocean Tide (GOT) model is computed using Topex/Poseiden data and is supplemented in shallow seas and polar seas (latitudes above 66^o) by 81 35-day cycles of ERS-1 and ERS-2 data and uses FES94 as an apriori model [*Ray*, 1999]. In the simulation, the difference between these tide models is considered to be the magnitude of the error in the tide models.

The hydrology model that is used in the simulations is the 3-hr Global Land Data Assimilation System (GLDAS)/Noah land-surface model [*Rodell et al.*, 2004]. Ice mass variations in Greenland and Antarctica are defined via a 6-hr ESA ice model, and was provided by the European Space Agency [*van Dam et al.*, 2008]. There is only one hydrology and one ice model, as these are usually considered to be the signals of interest; therefore we try to recover hydrology and ice rather than using a second model to remove their effects. Temporal aliasing errors from hydrology and ice are introduced in the simulations by mass variations which have a frequency greater than twice the sampling frequency of the mission; i.e. undersampling these signals. It should be noted that ocean bottom pressure (OBP) is also considered to be a signal of interest. It can be recovered simply by treating NCEP and MOG2D as forward models and calculating corrections made to them during the estimation process.

Figure 3.2 shows the power in the GLDAS hydrology model and ESA ice model in terms of geoid height along with the power of the difference between two AOD models (this shows the power in the aliasing error due to the AOD models). Also plotted is the absolute power in the AOD signal (ECMWF + OMCT). Note that the power in the tide errors is not shown on this plot because ocean tides are not traditionally represented in terms of spherical harmonic coefficients, and it is difficult to quantify the magnitude of the error in terms of geoid height. However, *Ray and Luthcke* [2006] performed this analysis and quantified the tide model error (defined as the difference between between the GOT00.2 tide model and the TPXO.6 tide model in their study) in terms of geoid height. The magnitude of the tide model error in *Ray and Luthcke* [2006] is lower than the AOD error in Figure 3.2 until approximately degree 20, where the tide model error then dominates.

Figure 3.2 shows that at approximately degree 45, the magnitude of the difference between two AOD models becomes larger than the magnitude of one of the AOD models. This means that for degrees higher than 45, the AOD model can be considered to be nearly 100% error. The power of the hydrology and ice signals has only slightly more power than the AOD error introduced. This indicates that if one wants to recover hydrology and ice, it may be difficult, as the signal to noise ratio is expected to be low. However, this is perhaps an unfair comparison as hydrology and ice

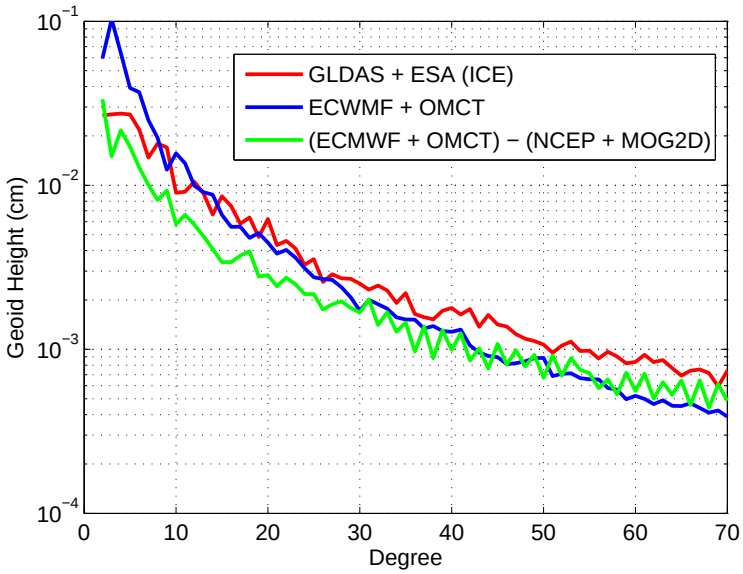

Figure 3.2: Comparison of hydrology signal power and AOD error power

models are constrained to only the continents, so it represents power only over the land, while the AOD error is for the entire globe. Furthermore, it should be noted that the capability of a mission to detect mass variations at a particular location on the globe will depend on the strength of the signal and error in that particular region, not the signal and error averaged over the entire globe. This is why it is important to analyze results on a regional scale, and not rely completely on global metrics. It should additionally be mentioned that a spatial plot of the AOD errors reveals that most of the error occurs in high latitude regions, particularly in Antarctica, where the data used as input to create the models are more sparse.

3.4 Numerical Simulation Procedure

While computationally expensive and time-consuming, numerical simulations provide the capability of estimating large gravity fields while including a variety of force models. To compare the ability of various mission architectures in recovering the gravity field, numerical simulations are necessary. All simulations are run using GEODYN [*Pavlis et al.*, 2010] (a precise orbit determination and geodetic parameter software package), SOLVE [*Ullman*, 1997] (a large linear systems

solve), and solvepa, a modified version of SOLVE. GEODYN and SOLVE have been provided by NASA Goddard Space Flight Center and solvepa has been provided by the Department of Earth Observation and Space Systems (DEOS) at TU Delft. All computations are performed using a cluster of ten Apple Xserve processors with one processor designated to be the headnode and the other nine processors designated as slave nodes. Each Xserve has a Quad Xenon processor, allowing for 36 jobs to be processed simultaneously through the use of Xgrid for the distributed computing. The data is stored in a 7 TB Xserve RAID storage device.

GEODYN implements an iterative weighted least squares estimation algorithm to solve for spherical harmonic coefficients. The least squares algorithm is given by[*Tapley et al.*, 2004b]

$$A\hat{x}_o = b \tag{3.3}$$

with

$$A = H^T W H + \overline{P}_o^{-1} \tag{3.4}$$

and

$$b = H^T W y + \overline{P}_o^{-1} \overline{x}_o. \tag{3.5}$$

where

$\hat{x}_o$ = *state deviation vector*

y = *observation deviation vector*

$\overline{x}_o$ = *a priori estimate of state deviation vector*

H = *matrix of partial derivatives relating the state to the observations*

W = *weighting matrix of observations*

$\overline{P}_o$ = *apriori covariance matrix containing weighting information for state deviation vector.*

A is defined as the information matrix, which is the inverse of the covariance matrix that contains variance information on the state. Note that in our case, the state deviation vector consists of the state of the spacecraft along with the spherical harmonic coefficients that are being solved

for. While we solve for the gravity field in terms of spherical harmonic coefficients, there are other sets of basis functions and other processing methodologies which have been successfully used to characterize gravity field variations. For example several groups have used mass concentration blocks with spatial and temporal constraints to solve for the gravity field [*Rowlands et al.*, 2010], while other groups have used wavelet functions [*Fengler et al.*, 2007]. While other methods have proved useful, all gravity solutions presented in this work have been solved for in terms of spherical harmonic coefficients.

The numerical simulation consists of a *truth* and a *nominal* case which differ from each other. The *truth* case represents the truth; that is, it represents the actual GRACE follow-on mission with measurement system errors as discussed in Section 3.2. The *nominal* case represents our best guess of the GRACE follow-on mission, with appropriate dealiasing models as discussed in Section 3.3. Table 3.1 outlines the models that are input to the *truth* and *nominal* cases. Note that the simulation defined in Table 3.1 is used to recover hydrology and ice mass variations; that is, the goal of the mission is to quantify how well these signals can be recovered in the presence of measurement errors and errors in atmospheric, ocean, and tide models, given by the difference between the two sets of models. When differencing the two sets of atmosphere and ocean models over a particular timespan there will be a static as well as a time variable part. Since we are only interested in including the time variable part of the model differences, the static part is calculated and subtracted from to the mass estimates during the post-processing. If this step were not included, then the recovered hydrology and ice signals would have a bias equal to the static part of the difference between the atmosphere and ocean models. It should be noted that ocean bottom pressure variations can still be estimated using the simulation definition in Table 3.1; one simply treats the NCEP and MOG2D models as forward models and calculates corrections to them. EIGEN-GL04C is a static gravity field model which was created using GRACE and Laser Geodynamics Satellite (LAGEOS) data along with surface data, and was produced by Geo-Forschungs-Zentrum (GFZ) in Potsdam, Germany and Groupe de Recherche de Geodesie Spatiale (GRGS), in Toulouse, France [*Förste et al.*, 2008]. Note that errors in the static gravity field model

are neglected.

Models	Truth	Nominal
Static gravity field	EIGEN-GL04C	EIGEN-GL04C
Ocean tide model	FES2004	GOT00
Atmospheric model	ECMWF	NCEP
Ocean model	OMCT	MOG2D
Hydrological model	GLDAS	none
Ice model	ESA	none

Table 3.1: Simulation and model definitions

The numerical simulation is intiated by running the *truth* case with the models listed in Table 3.1. The epoch elements of the spacecraft are integrated using the appropriate models, and a set of range-rate measurements is generated in five-second intervals. Note that the force models used for integration include only those listed in Table 3.1, with each model expressed to degree and order 100, with the exception of NCEP and MOG2D which are only defined to degree 72. All other forcing parameters are turned off (i.e. no atmospheric drag, solar radiation pressure, Earth radiation pressure) as it was assumed the mission will fly drag-free so these non-conservative forces are accounted for. N-body gravitational effects from the Sun, moon, and other planets, which are conservative forces are also not modelled, as these are well known forcing paramters and their effect is typically removed prior to gravity estimation. Any error in the ephemeris of the other planets is assumed to have a neglible impact on the gravity field estimation. The integration is performed in one-day arcs; thus, if it is desired to simulate one month of data, we end up with 30 one-day sets of range-rate measurements. The measurement noise associated with the laser interferometer and the drag-free system, as described in Section 3.2, is then added to the set of *truth* measurements. Additionally, positions of the spacecraft are written every 10 seconds to simulate GPS measurements, and a white noise distribution of 1-cm RMS in magnitude is added to each component of the spacecraft's position to simulate the error in the GPS measurements.

The next step of the process involves integrating the satellites again, only through the set of *nominal* force models as described in Table 3.1. Again, range-rate measurements are generated

in five-second invervals over one day and spacecraft position measurements are generated every 10 seconds over the day. This becomes the *nominal* set of measurements, and by differencing the *truth* and *nominal* measurements, we are left with a set of range-rate residuals and position residuals. Both sets of residuals are used to solve for corrections to the spacecraft state only. This step is included so the state of the spacecraft can be adjusted to compensate for the change in energy of the system (given by the change in force models), and makes for a more realistic simulation.

The final step is the data reduction step, in which the spacecraft are again integrated through the set of *nominal* force models, only with the new spacecraft position estimates that were generated in the previous step, to form a new set of range-rate measurements. We now use only the newly generated set of range-rate residuals to gain the normal equations (given by Equation 3.3) for each one-day arc, to estimate corrections to both the spacecraft state and the spherical harmonic coefficients. The spacecraft state parameters are converted to baseline elements via [*Rowlands et al.*, 2002], and nine of the twelve parameters are constrained during the estimation process. This allows us to avoid introducing spacecraft position measurements during the estimation process; hence relative weighting issues between the two data types are avoided. Assuming a 30-day solution is desired, SOLVE (or solvepa) is used to combine all 30 days of data into one solution for the gravity field. SOLVE uses a Cholesky decomposition to compute the inverse of the large information matrix given in Equation 3.4. The advantage of using a Cholesky decomposition is that it avoids inverting the information matrix, thus gaining considerable numerical accuracy in the estimation process. Note that no apriori information is introduced for the spherical harmonic coefficients during the estimation.

An alternate methodology was also explored for the data reduction step in which both the range-rate residuals and spacecraft position residuals are used to solve for the gravity field and corrections to the spacecraft state. This step requires that the range-rate measurements be weighted more heavily than the spacecraft position measurements (we used a weight of 1 cm for the GPS measurements and 1 nm for the range-rate measurements). Additionally, the state of the spacecraft are kept in cartesian space during this process. Both processes have been tested and nearly identical

results are obtained. The one discrepancy is that sometimes an unrealistic estimate of J_2 is produced when using both spacecraft position measurements and range-rate measurements to estimate the gravity field; thus a light constraint must be applied to the J_2 coefficient. Figure 3.3 plots the geoid height error obtained from a simulation of a hypothetical mission, with measurement system errors and aliasing errors from AOD and tides models. Figure 3.3 compares the results from processing spacecraft position and range-rate measurements using cartesian elements for the state of the spacecraft, to processing only range-rate measurements while using baseline parameters for the state of the spacecraft. It is seen that both methodologies produce nearly identical results. In order to be consistent, the results in this study have been produced using only range-rate residuals, to avoid optimizing the relative weighting between the two measurement types.

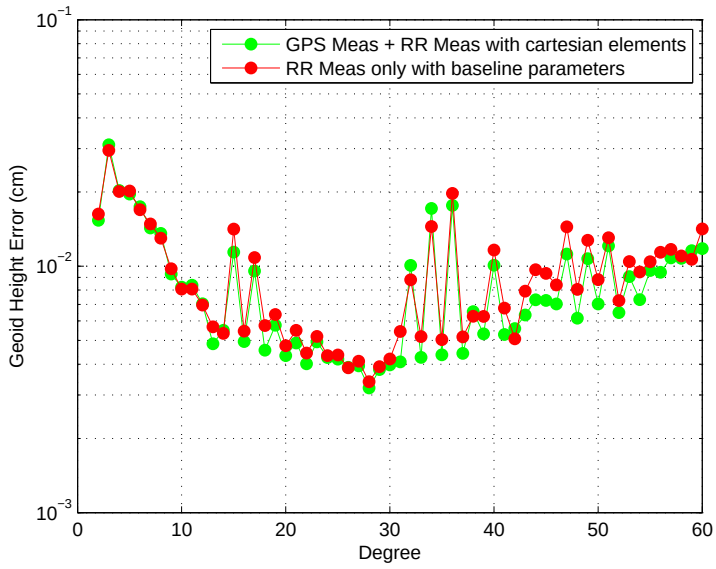

Figure 3.3: Geoid height error for a hypothetical follow-on mission testing two solution strategies

One other caveat with the data processing should be mentioned. Arc lengths of one day were used when processing the data to be consistent with the processing performed at CSR, GFZ, JPL, and GFSC. We also explored the option of having shorter arc lengths of 6 hours and 12 hours. Results indicate that the shorter arc lengths actually result in more accurate estimates of the gravity field. This is presumably due to a better fit of the satellite orbits as well as a reduction

in the amount that temporal aliasing errors are accumulated. However, this study did not attempt to optimize the arc length of the data, and due to increased processing time associated with shorter arcs, we chose to process daily arcs to be consistent with other processing centers. This can be considered a topic for future research, however.

Chapter 4

Estimating High Frequency/Low Resolution Gravity Fields

4.1 Introduction

As disussed in Section 1.4, temporal aliasing errors can be reduced via three methods: (1) increasing the sampling frequency of the mission, (2) improving the dealiasing products (atmosphere, ocean, tides models), and (3) co-estimating parameters which vary at high frequencies. This chapter focuses on a combination of (1) and (3), exploring the feasibility of estimating low resolution gravity fields at high frequencies simultaneously during the inversion process to reduce the effect of temporal aliasing errors from mass variations with large spatial scales. The ultimate goal is to obtain a gravity solution with superior spatial resolution over what a typical post-processed (after destriping and smoothing via *Swenson and Wahr* [2006]) gravity solution would provide. We explore the potential of this estimation scheme for three possible follow-on mission architectures: a single pair of polar orbiting satellites similar to GRACE, two pairs of polar orbiting satellites, and a polar pair of satellites coupled with a lower inclined pair of satellites. The rationale for selecting these architectures for comparison is straight-forward, as they represent a low-cost, mid-cost, and high-cost option, respectively, for a future gravity measuring mission. Since temporal aliasing errors are expected to dominate the error budget of future missions, a relatively simple way to reduce these errors is to sample more frequently by adding a second pair of satellites, hence the rationale for examining the second two cases. The third case is of particular interest, as the addition of a lower inclined pair provides East-West information and is anticipated to reduce longitudinal striping in the solutions, as discussed in *Bender et al.* [2008]. However, this option is higher cost, due to

the requirement of two launch vehicles, and higher risk, as there would be a polar-gap in coverage should the polar pair of satellites fail.

4.2 Motivation: Reducing AOD Errors

Figure 1.2 shows that the dominant source of temporal aliasing error is due to mismodelling of atmosphere and ocean signals (AOD error). Thus, it is desirable to first focus on reducing these errors. Figure 3.2 shows that the majority of the AOD error is at long wavelengths, or low degrees. Since much less data are needed to estimate a gravity field to low degree and order rather than out to high degree and order (as GRACE does), then one can think of estimating low degree and order gravity fields at short time intervals to directly estimate errors due to atmosphere and ocean models. In theory, this should mitigate the effect of temporal aliasing errors on the gravity solution.

The question now arises as to what the optimal frequency is to estimate a low degree and order gravity field to reduce aliasing effects. This will depend on the satellite groundtrack coverage (discussed in Section 4.4) as well as the frequency content of the AOD error. To better understand the latter, Empirical Orthogonal Functions (EOFs) are used to analyze the time series of the atmosphere and ocean models. Figure 4.1 shows the spatial and temporal parts of the first mode expressed in cm of equivalent water height (EWH), which represents 67% of the variance in the model errors over a particular 19-day timespan.

The spatial part of the first mode shows that most of the error is concentrated in high latitude regions, while the time series in Figure 4.1 seems to have a dominant period near 2-3 days. To confirm this, a Fourier analysis is performed on the time series in Figure 4.1, and the frequency content of the error is shown in Figure 4.2. Note that the AOD error has been expressed in terms of period, rather than frequency in this plot. Two dotted lines are plotted and labeled, with everything to the right of the dotted line representing the amount of signal that would be recovered by making one-day and two-day estimates of the gravity field, respectively.

Figure 4.2 shows that nearly all of the power in the AOD error has periods greater than two days. There is a peak in the power at periods of 2, 4, and 8 days, increasing in magnitude at larger

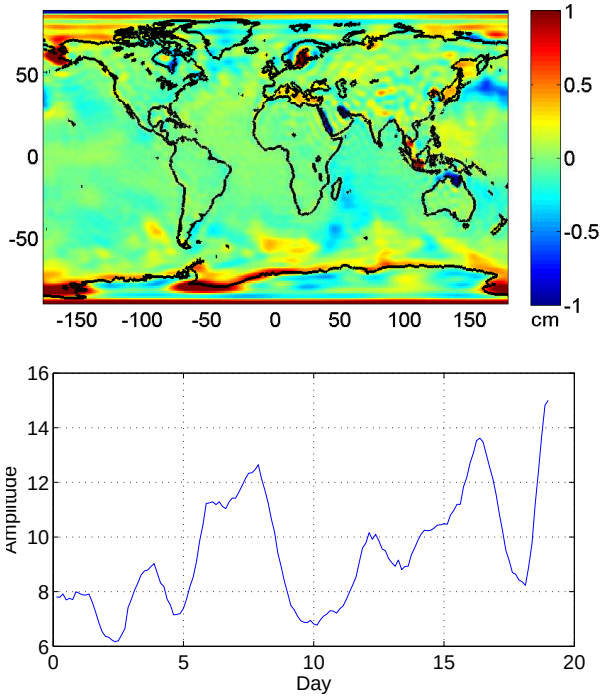

Figure 4.1: Spatial (top) and temporal (bottom) parts of the first mode of the AOD error over a 19-day timespan expressed in cm of EWH

periods. This figure suggests that making daily estimates of the gravity field will provide the largest reduction in temporal aliasing errors, as there is a substantial amount of power between periods of two days and four days; however, two-day estimates of the gravity field should capture much of the variability as well. The signal with periods around 2-4 days is most likely due to mismodelling of fronts and extratropical storms, which typically have periods in this range [*von Storch and Zwiers*, 1999]. While only a single 19-day time span is shown in Figure 4.1, the AOD error was analyzed for other time periods as well. Analyses for other time spans reached similar conclusions as stated above.

4.3 Estimation Process

As discussed in Section 3.4, SOLVE (or solvepa) is used to combine the normal equations for daily arcs of data to gain a final multi-day estimate of the gravity field. SOLVE specifices between arc parameters and global parameters; the former being parameters which change throughout the

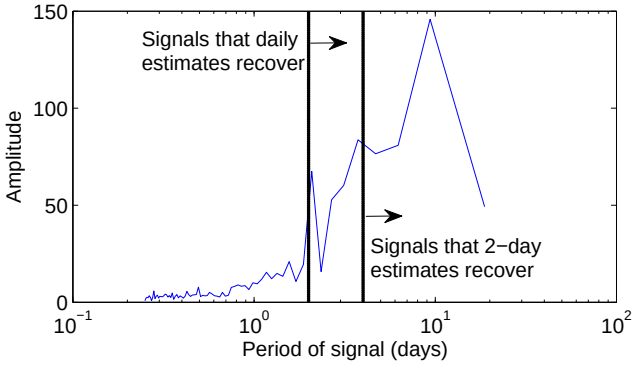

Figure 4.2: Frequency content of the first EOF of the AOD error displayed in Figure 4.1

simulation (such as the position and velocity of the spacecraft), and the latter being parameters that are static throughout the simulation (such as the spherical harmonic coefficients which define the gravity field). The arc parameters are estimated each arc (in this case, each day), while the global parameters are estimated only once for the duration of the simulation. SOLVE was modified to allow the spherical harmonic coefficients to be defined as arc parameters, meaning they would then be estimated each arc along with the state of the spacecraft. This modified version of SOLVE is referred to as solvepa, and was provided by DEOS at TU Delft University. While we use spherical harmonic functions to estimate high frequency gravity field variations, there may be another set of basis functions tailored to the estimation of temporal aliasing errors, such as mascon parameters or wavelets. However, alternate basis functions (aside from spherical harmonic functions) were not included in this study.

The mathematical description of the above process is given in the ensuing derivation. Equation 3.3 can be partitioned to keep arc parameters and global parameters separate during the estimation process. This partitioning leads to

$$\begin{pmatrix} A_{11} & A_{12} \\ A_{21} & A_{22} \end{pmatrix} \begin{pmatrix} x_1 \\ x_2 \end{pmatrix} = \begin{pmatrix} b_1 \\ b_2 \end{pmatrix}, \tag{4.1}$$

where the subscript 1 represents the arc parameters and the subscript 2 represents the global

parameters. One can then multiply the first row of Equation 4.1 by A_{11}^{-1} and subtract $A_{21}A_{11}^{-1}$ multiplied by the first row from the second row, leading to

$$\begin{pmatrix} A_{11}^{-1}A_{11} & A_{11}^{-1}A_{12} \\ A_{21} - A_{21}A_{11}^{-1}A_{11} & A_{22} - A_{21}A_{11}^{-1}A_{12} \end{pmatrix} \begin{pmatrix} x_1 \\ x_2 \end{pmatrix} = \begin{pmatrix} A_{11}^{-1}b_1 \\ b_2 - A_{21}A_{11}^{-1}b_1 \end{pmatrix}, \tag{4.2}$$

which reduces to

$$\begin{pmatrix} I & A_{11}^{-1}A_{12} \\ 0 & \overline{A}_{22} \end{pmatrix} \begin{pmatrix} x_1 \\ x_2 \end{pmatrix} = \begin{pmatrix} A_{11}^{-1}b_1 \\ b_2 - A_{21}A_{11}^{-1}b_1 \end{pmatrix} \tag{4.3}$$

when defining $\overline{A}_{22} = A_{22} - A_{21}A_{11}^{-1}A_{12}$.

Solving this system of equations for the arc parameters gives

$$x_1 = A_{11}^{-1}\left[\left(I + A_{12}\overline{A}_{22}^{-1}A_{21}A_{11}^{-1}\right)b_1 - A_{12}\overline{A}_{22}^{-1}b_2\right]. \tag{4.4}$$

It is in this process where the user can define the low degree and order part of the gravity field as arc parameters, and solve for them each arc. Once this process is completed, assuming 19 days of data are processed in 1-day arcs, the user is left with 19 1-day estimates of the gravity field to low degree and order, and one 19-day estimate of the gravity field for the higher degrees. The benefit to this approach is obvious: the daily low-degree gravity field estimates provide a place for high frequency mass variations to be estimated; thus, reducing temporal aliasing errors and improving the higher degrees. At this point, the final data product released to the community could simply be a 19-day average of higher degree coefficients and daily solutions of lower degree coefficients. These daily solutions with low spatial resolution could aid in improving atmospheric models, and possibly be beneficial to the oceanography community as well, as many of these signals have large spatial scales with high frequencies.

However, the primary goal of this project is to increase the spatial resolution (better determination of higher degrees) of the final 19-day gravity field estimate. As such, we are not as interested in the daily solutions themselves, but, for simplicity, desire a data product with a 19-day solution for all coefficients. We gain a single 19-day estimate of the low degrees by running SOLVE once more (specifying only the spacecraft state as arc parameters), with the higher degrees of the

gravity field constrained such that they are not allowed to vary, to then gain a 19-day estimate of the low degree part of the solution. Alternately, one could simply average the 19 1-day low degree solutions together to gain a 19-day estimate of the low degrees, leading to near equivalent results.

It should be noted that this method of estimation is fundamentally different than that described in *Kurtenbach et al.* [2009]. This method provides daily estimates of the gravity field to low degree and order which are uncorrelated from each other. The daily solutions gained in *Kurtenbach et al.* [2009], alternately, are correlated between each other due to the Kalman filter approach and are biased towards an a apriori hydrology model. Their approach allows for much greater spatial resolution in the daily solutions than what is provided here. Again, it should be stressed that the primary goal of this project is not to gain daily solutions, but to improve estimates of high degrees terms by simultaneously estimating low resolution gravity fields at a high frequency to reduce temporal aliasing errors.

4.4 Groundtrack coverage

As mentioned in Section 4.2, the ability to estimate a low degree and order gravity field at a particular frequency is a strong function of the groundtrack pattern of the satellite. According to the Columbo-Nyquist [*Colombo*, 1984] rule, the maximum resolvable degree in the gravity field is equal to half of the number of revolutions of the pair of satellites, given homogeneous spacing between the tracks. This rule has recently been revised in *Visser et al.* [2011], to state that the Colombo-Nyquist rule holds for gravity solutions that are homogeneous as a function of longitude. However, solutions are possible when estimating to degrees larger than half the number of orbital revolutions; they are just not guaranteed to be homogeneous in the longitudinal direction. In fact, the maximum resolvable degree for low-low satellite-to-satellite tracking is equal to approximately twice the number of orbital revolutions. Thus, in theory, given a polar pair of satellites that completes sixteen revolutions in one day, one should be able to solve for a gravity field out to degree and order 32 or so. The quality of the solutions will not, however, be homogeneous as a function of longitude. For a homogeneous solution in longitude, the maximum resolvable degree

would be equal to 8.

For the purposes of validating this process, three mission architectures are considered: a single pair of polar orbiting satellites, two pairs of satellites both in polar orbits, and a pair of satellites in a polar orbit coupled with a pair of satellites in a lower inclined orbit. For the case of a single pair of satellites in a polar orbit, the satellites are separated by 100 km at an altitude of 315 km in an 18.95-day repeating groundtrack. For the case of having two pairs of satellites in polar orbits, a second pair of satellites is added to the previously mentioned pair, only offset in the node by approximately 180^o (see Equation 5.15 for exact offset). This type of configuration ensures that the second pair of satellites will cross near the equator in the same location that the first pair of satellites did approximately one-half of a revolution later in time, and was found to be optimal, as discussed in Section 5.4.5. Finally, for the case of having a lower inclined pair and a polar pair of satellites, a pair of satellites at an altitude of 291 km and an inclination of 76^o in an 18.85-day repeating groundtrack is added to the pair of polar orbiting satellites. For the simulations, 19 days of data are processed to estimate a 100x100 gravity field. The repeat periods of the satellites will be referred to as 19 days for the remainder of the dissertation, since both repeat periods are nearest to this integer.

The polar pair of satellites described above completes 15.86 revolutions in one day, meaning that one should be able to estimate a homogeneous 8x8 gravity field using one day of data, while two pairs enables the user to estimate close to a 16x16 gravity field in one day, provided interleaved groundtracks. Figure 4.3 shows the groundtracks over one day for the polar pair of satellites alone, the two pairs of polar satellites, and the polar pair of satellites coupled with the lower inclined pair of satellites. This figure shows that over one full day, each case has fairly homogeneous coverage over the Earth, lending itself well to making daily estimates of the gravity field to low degree and order.

While Figure 4.3 shows the groundtracks of the satellites over one day, it is also interesting to consider the coverage over the Earth for time scales both shorter and longer than this. It is easily seen that one day is a lower limit on the amount of time it takes to provide homogeneous coverage

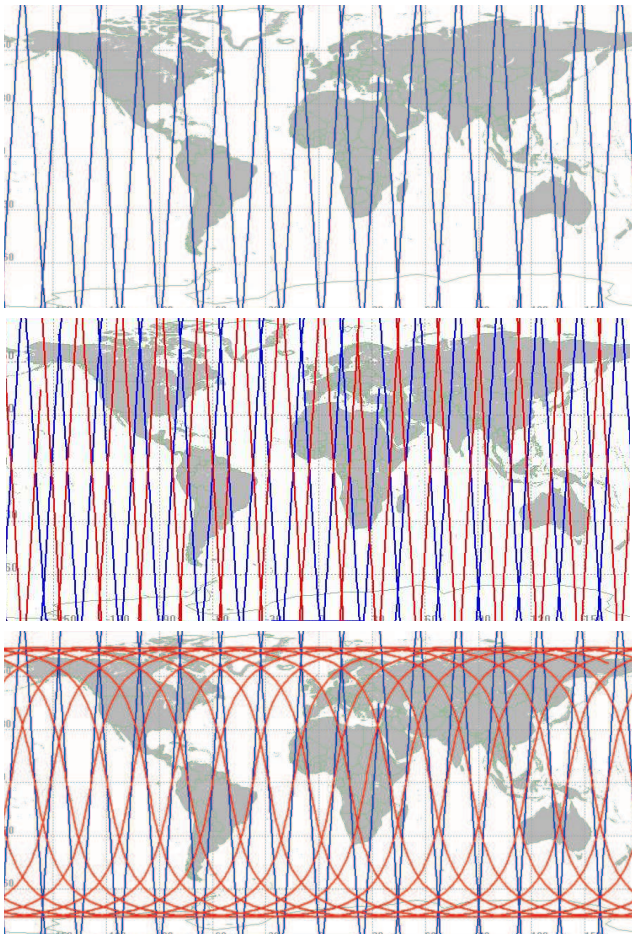

Figure 4.3: Groundtracks over one day for a single pair of polar orbiting satellites (top), two pairs of polar orbiting satellites (middle), and a polar pair of satellites coupled with a lower inclined pair of satellites (bottom)

over the Earth, since it takes a full day for the Earth to rotate 360^o underneath the satellites. To gain homogeneous coverage on time scales shorter than one day, multiple pairs of polar satellites would have to be used in a proper configuration. Since the frequency content of the AOD error shown in Figure 4.2 suggests that there would be minimal benefit in estimating gravity fields at time scales shorter than one day, this case was not considered in the dissertation.

If one thinks of estimating low degree and order gravity fields using more than one day of data, for example two days of data, the most improvement in the solution will be seen if the groundtracks provide homogeneous coverage over two days. For this criterion to be met, the satellites must perform an integer number of revolutions over one day plus one half of another

revolution, i.e. near 15.5 revolutions in one day. This guarantees that homogeneous coverage over two days would then exist, as the groundtracks on the second day would fill in the gaps between the groundtracks on the first day. Simple orbital mechanics quickly shows that for this criterion to be met, the satellites would need to be flown at an altitude near 420 km.

Given the nature of the groundtracks of the satellites, coupled with the fact that the AOD temporal aliasing error has substantial power with 2-4 day periods, it is expected that estimating low degree and order gravity fields with daily resolution will provide the best results.

4.5 Results

To analyze the effectiveness of estimating low resolution gravity fields at a high frequency, the quality of the low resolution gravity fields is studied along with the benefit that these estimates provide to the final gravity solution. The following results show the quality of both one-day and two-day estimates for the three cases examined. Then, improvements in determining hydrology, ice mass variations, and ocean bottom pressure signals that estimating the high frequency gravity fields provides is studied. The degree of the high frequency estimate of the gravity field is also optimized.

4.5.1 Quality of the Estimated High Frequency Gravity Fields

4.5.1.1 Daily Estimates

Figure 4.4 shows the quality of the daily estimates for one pair of satellites estimating a 6x6 gravity field (top), two pairs of polar orbiting satellites estimating a 14x14 gravity field (middle), and a polar pair coupled with a lower inclined pair of satellites estimating a 14x14 gravity field (bottom) each day. Estimating the fields out to degree and order 6 and 14, respectively, were chosen to ensure gravity solutions that are homogeneous as a function of longitude, in accordance with the Colombo-Nyquist rule described in Section 4.4. The plots show a series of truth and recovered signals for different days spaced nine days apart, reading left to right sequentially in

time with results from Jan. 1, 2003; Jan. 10, 2003; and Jan. 19, 2003 shown. The top row of plots is the difference between the truth and nominal signals. For this case, the ocean tides and ice signals have been removed from the simulation in Table 3.1 to focus solely on the AOD error along with undersampling of hydrology. Hence, the top plots represent a one-day average of the GLDAS hydrology signal added to the atmosphere and ocean error, defined as the one-day average of (ECMWF + OMCT) - (NCEP + MOG2D). This is the temporal aliasing error that we are trying to directly estimate. The bottom row of plots shows the recovered signal for each selected day. In essence, one is hoping to match the top and bottom plots, thus giving a good estimate of the temporal aliasing error every day out to low degree and order.

There are several things to notice from Figure 4.4. First, as the truth signals increase in time from left to right, one can see how much temporal variability there is in hydrology and the AOD error over 19 days. If these signals were static over the 19-day timespan, then it would be simple to estimate them. The variability is what leads to a degradation in the gravity solutions. Next, it is easily seen that one pair of satellites does a poor job of making daily estimates of the gravity field to degree and order six. While some of the spatial patterns in the truth signals are recovered decently in the polar regions (where the coverage is more dense), the solutions degrade substantially over the equatorial regions. When another pair of polar satellites is added, doubling the number of observations, it is seen that the two polar pairs together do a fairly decent job of estimating the gravity field each day out to degree and order 14. When a lower inclined pair, rather than a second polar pair, is added to the polar pair of satellites, it is seen that the quality of the daily estimates improves even more. This is due to the addition of East-West information that the lower inclined pair adds to the solution.

Table 4.1 gives the spatial RMS of the power in the signal, along with the spatial RMS of the errors in the recovered signal for estimating daily gravity fields to different degree and order for both one pair and two pairs of satellites. The spatial RMS of the error is calculated by differencing the spatial plots of the truth and recovered signals, and calculating an RMS of the spatial plot of errors, as discussed in Section 2.3.1.2. All RMS values are expressed in terms of cm of equivalent

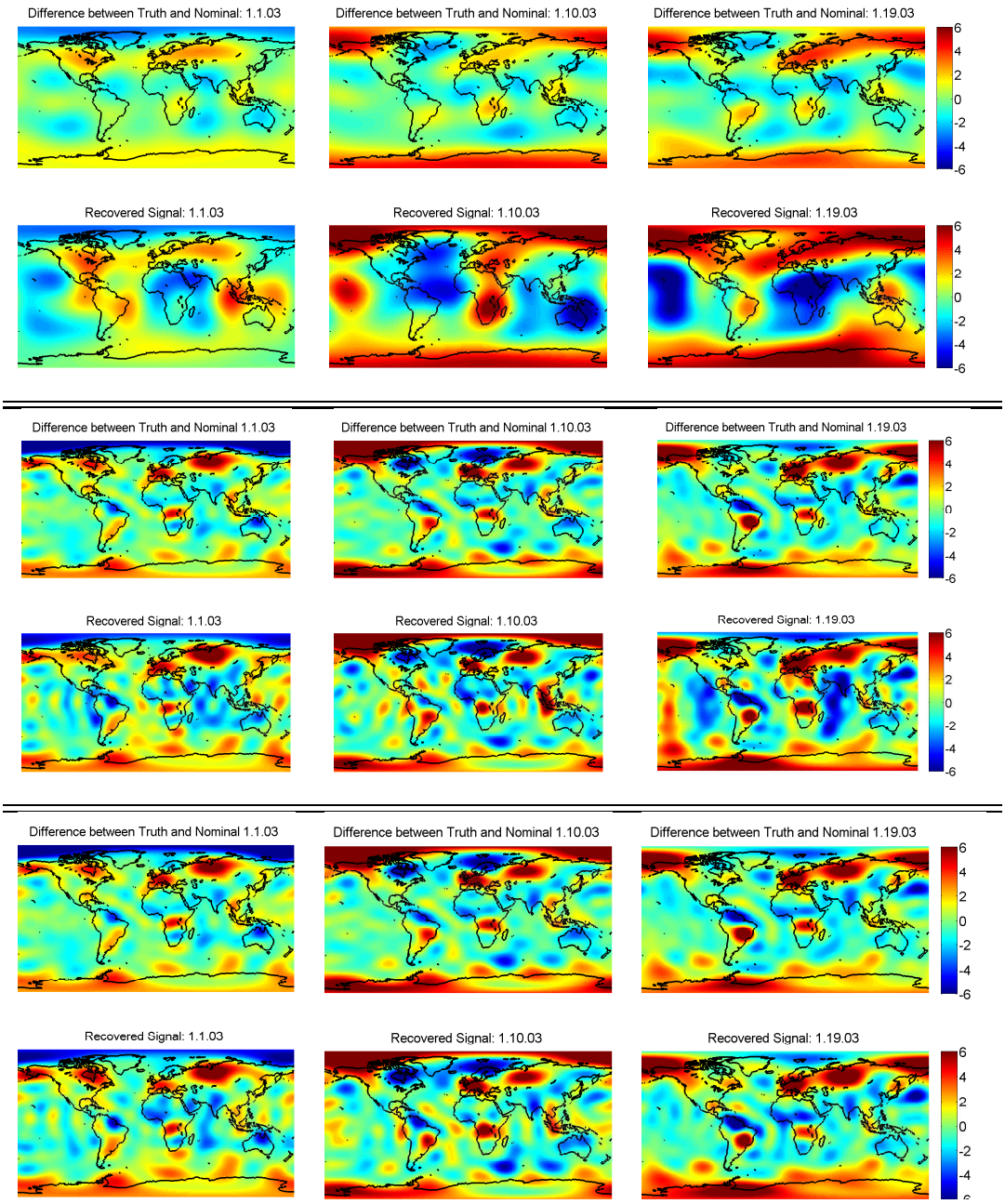

Figure 4.4: There are three sets of results in this figure: one pair of satellites estimating a daily 6x6 (top), two pairs of polar orbiting satellites estimating a daily 14x14 (middle), and two pairs of satellites (one polar and one lower inclined) estimating a daily 14x14 (bottom) gravity field model. The top row of plots shows the difference between the *truth* and *nominal* cases; for this example it is the GLDAS hydrology signal plus the AOD aliasing error. Hence, the top row of plots represents the signals we are trying to recover with the daily estimates. The bottom row of plots shows the recovered signals for each day. The plots are arranged from left to right sequentially for different days spaced 9 days apart: Jan. 1, 2003; Jan. 10, 2003; and Jan. 19, 2003. Units are in cm of equivalent water height (EWH).

water height (EWH). The RMS values were obtained by averaging the RMS values for each day over the 19-day time span. Daily estimates beyond degree 22 are not shown as the results tend to degrade past this point. The RMS values are not shown for the one pair case beyond degree 14, as the errors were too high to be near reasonable.

Degree of Daily Estimate	**Signal RMS**	**Error RMS**		
		One Pair	**Two Polar Pairs**	**Polar Pair + Lower Inc. Pair**
6	1.68	1.77	0.76	0.81
10	2.20	2.07	0.77	0.75
14	2.44	3.04	1.32	0.86
18	2.58	–	1.32	0.61
22	2.76	–	3.18	0.74

Table 4.1: 19-day average of the daily RMS values of signal and error for the cases of one pair and two pairs of satellites for different degrees of a daily gravity field estimate. Units are in cm of EWH.

Table 4.1 shows that given a single pair of polar orbiting satellites, the signal to noise ratio is nearly always less than one no matter what degree the daily gravity field is estimated to. This shows the inability of a single pair of polar orbiting satellites to make a low degree and order estimate of the gravity field with only one day of measurements. Two pairs of polar orbiting satellites are capable of estimating daily gravity fields out to degree 18 or so, but when the solution extends to degree 22, the signal to noise ratio drops below one. At this point, the gravity solution is not guaranteed to be homogeneous as a function of longitude. The case of having a polar pair of satellites coupled with a lower inclined pair of satellites provides the best results, with daily estimates of the gravity field beyond degree 10 having much greater accuracy than the case of two polar pairs. This result shows the benefit of having East-West information in the gravity solution in addition to the North-South information that the polar pair of satellites provides.

4.5.1.2 Quality of Two-Day Estimates

Results from Section 4.5.1.1 showed the inability of one pair of satellites to estimate a low degree and order gravity field each day. While estimating a gravity field at daily intervals is preferred, Figure 4.2 indicates that making two-day estimates of the gravity field could also provide a reduction in the level of temporal aliasing errors. The number of measurements that are accumulated over two days with a single pair of satellites will equal the number of measurements that two pairs of satellites provide over one day. Thus, it is hypothesized that one pair of satellites will be able to estimate a low degree and order gravity field every two days with error levels similar to those realized by two pairs of satellites over one day. Since two pairs of satellites show sufficient ability to estimate a low degree and order gravity field over one day, the case of having two pairs of satellites making two-day gravity field estimates is not explored in this section.

One limitation with performing estimates every two days is the fact that the groundtracks are not guaranteed to be near-homogeneous, as discussed in Section 4.4. Thus, two architectures are examined to explore the benefit of making two-day estimates of the gravity field using a single pair of polar orbiting satellites. The first is using the same pair of satellites as was used in Section 4.5.1.1, at 315 km altitude, performing 15.86 revolutions in one day. This guarantees inhomogeneous coverage in the groundtrack pattern over two days. The second architecture examined is a polar pair of satellites in a 19-day repeating groundtrack, but at 421 km altitude, performing 15.49 revolutions per day. This configuration provides near-homogeneous coverage over two days. Figure 4.5 shows the groundtracks of both cases plotted over two days. The difference in homogeneity of the groundtracks between the two cases is easily seen. It is expected that having homogeneous coverage, albeit at a higher altitude, should provide improved results in making the two-day estimates.

To analyze the ability of both cases to accurately estimate a low degree and order gravity field every two days, ten two-day estimates were analyzed, for a total of 20 days of data. Table 4.2 shows the 20-day average of the two-day signal and error RMS values for the higher and lower altitude cases in making two-day estimates of the gravity field to different degrees. The RMS values

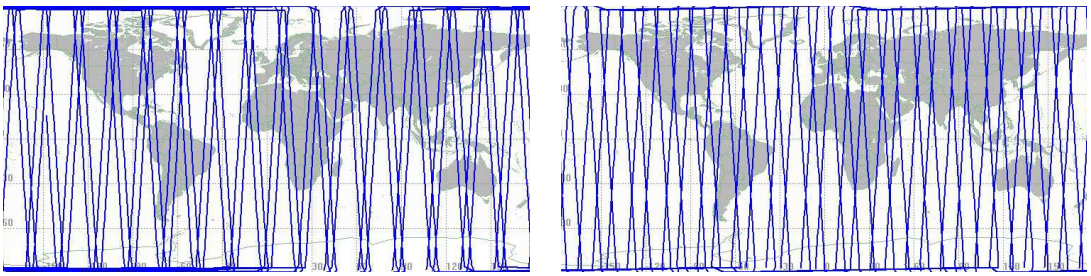

Figure 4.5: Groundtracks over two days for a single pair of polar orbiting satellites at 315 km altitude (left), and a polar pair of satellites at 421 km altitude (right)

are expressed in cm of EWH.

The first thing that can be noticed from the results in Table 4.2 is how much difference having two days of data makes in the ability to estimate a low degree and order gravity field. Comparing the one-pair, 315 km altitude results with those from Table 4.1 using only one day of data to make the estimates shows the improvement that adding a second day of data provides. Furthermore, as expected, the results from the pair of satellites at 421 km altitude, with near-homogeneous groundtrack coverage over two days, are better than the results from the pair of satellites at 315 km with non-homogeneous coverage over two days, despite being at a higher altitude. This attests to the benefit in having near-homogeneous coverage over the time span of interest. Finally, when the results from one pair of satellites at 421 km altitude using two days of data are compared with the results from two polar pairs of satellites using one day of data, shown in Table 4.1, only slight differences are seen due to the different spatio-temporal sampling characteristics of the two cases. Again, it is seen that making daily estimates using a lower inclined pair coupled with a polar pair provides the most accurate estimates of the low resolution gravity fields.

It should also be noted that other frequencies were explored for making the low resolution estimates of the gravity field besides just one and two days. Results showed that daily solutions provided the most accurate results, which was expected from the discussions in Sections 4.2 and 4.4.

Degree of Two-Day Estimates	Signal RMS	Error RMS	
		One Pair/315 km	One Pair/421 km
6	1.65	1.36	0.87
10	2.15	1.36	0.97
14	2.38	1.65	1.17
18	2.51	1.57	1.23
22	2.67	2.10	2.16

Table 4.2: 20-day average of the two-day RMS values of signal and error for the cases of one pair of satellites at 315 km and 421 km altitude for different degrees of a two-day gravity field estimate. Units are in cm of EWH.

4.5.2 Improvements in Recovering Geophysical Signals

The primary purpose of estimating high frequency low degree and order gravity fields is to provide improved spatial resolution in the final multi-day gravity field estimate by reducing the effect of temporal aliasing errors. It still remains to be seen what effect estimating high frequency gravity fields has on the final solution, as well as what degree of the estimate is optimal. This section will address both of these issues for all three cases examined. It should be noted that the remainder of the results include ocean tide aliasing errors as well as an ice model, as outlined in Table 3.1, for a more comprehensive analysis. All analyses in this section are performed on a global scale, i.e. examining signals and errors globally.

4.5.2.1 One Pair of Satellites

Sections 4.5.1.1 and 4.5.1.2 showed that one pair of satellites is not capable of providing accurate low degree and order estimates of the gravity field on a daily time scale. However, when measurements are accumulated for two days, the situation improves considerably. Thus, results in this section will focus on the ability of one pair of satellites to recover geophysical signals of interest while estimating low degree and order gravity fields every two days.

Table 4.3 shows the spatial RMS of the errors in recovering hydrology signals, ice mass variations (defined as Greenland and Antarctica), and ocean bottom pressure (OBP) signals, over 20 days, for one pair of satellites at 421 km altitude making two-day estimates of the gravity field

to low degree and order. The results are obtained from differencing the truth and recovered signals spatially, truncated at degree and order 60. This truncation was performed as degrees higher than 60 were deemed to have too much noise to be reasonable for all cases considered. All numbers are expressed in cm of EWH. Note that the power of the hydrology, ice, and OBP signals are given under each label, and are 4.75 cm, 2.08 cm, and 2.67 cm, respectively.

Degree of Two-Day Estimates	**Hydrology RMS = 4.75**	**Ice RMS = 2.08**	**OBP RMS = 2.67**
none	26.28	31.02	29.08
6	17.70	11.90	19.52
10	21.19	11.19	22.20
14	20.07	10.86	20.24
18	17.93	6.58	17.16
22	22.37	7.00	20.33

Table 4.3: Spatial RMS of errors for one pair of satellites at 421 km altitude using different degrees of two-day estimates of the gravity field. Results are truncated at degree 60 and represent 20 days of data. Units are in cm of EWH.

Table 4.3 shows a sizeable reduction in the RMS of the errors when estimating two-day gravity fields to low degree and order, particularly for ice mass variations. Estimating two-day 18x18 gravity fields is shown to provide the most benefit in reducing the errors, providing a 32% reduction in the level of error in determining hydrology, a 79% reduction in ice mass variation errors, and a 41% reduction in OBP errors. The reason that ice mass variation errors are reduced more than errors in hydrology and OBP is twofold: first, this is the region where the groundtracks are the most dense, and second, it is also the region where AOD temporal aliasing errors dominate spatially. Thus, estimating high frequency gravity fields is expected to benefit the polar regions the most. It should be noted, however, that while the percentage of reduction in the level of errors is substantial, the magnitude of the errors is still much larger than the power in the signal.

Recall that the results presented in Table 4.3 were for one pair of satellites at 421 km, which have near-homogeneous groundtrack spacing over two day periods. Section 4.5.1.2 showed that this scenario provided more accurate estimates of the two-day gravity fields to low degree and order

than in the case of one pair of satellites at 315 km altitude which had inhomogeneous groundtrack spacing over two-day periods. We now would like to see if two-day estimates of the gravity field provide any benefit for the case of one pair of satellites at 315 km altitude. Table 4.4 shows these results.

Degree of Two-Day Estimates	**Hydrology RMS = 4.75**	**Ice RMS = 2.08**	**OBP RMS = 2.67**
none	14.89	18.23	15.69
6	7.84	5.09	6.47
10	7.80	4.53	6.16
14	7.78	4.94	6.31
18	8.60	4.96	7.54
22	11.21	5.80	9.78

Table 4.4: Spatial RMS of errors for one pair of satellites at 315 km altitude using different degrees of two-day estimates of the gravity field. Results are truncated at degree 60 and represent 20 days of data. Units are in cm of EWH.

Table 4.4 shows a substantial reduction in the RMS of the errors when estimating two-day gravity fields to low degree and order, despite the fact that the groundtracks are inhomogeneous over two day periods. The best results are given when two-day gravity field estimates are made to degree and order 10, providing a 48% reduction in the level of error in determining hydrology, a 75% reduction in ice mass variation errors, and a 61% reduction in OBP errors. The fact that 10x10 two-day estimates are optimal for this scenario versus 18x18 two-day estimates being optimal for the 421 km case with near-homogeneous groundtrack coverage over two days attests to the benefit that proper groundtrack spacing provides, as discussed in Section 4.4.

It is interesting to note that both the absolute level of errors is lower, and the percentage reduction in the level of errors is greater for this case than for the case at 421 km altitude with near-homogeneous groundtrack coverage. Both of these results are a direct consequence of flying at a lower altitude. Thus, this result indicates that estimating low degree and order gravity fields has a greater impact for satellite missions flying at a lower altitude than those flying at a higher altitude. This result was confirmed via separate simulation studies that are not shown here.

It should furthermore be noted that the level of errors in Table 4.4, while much lower than those in Table 4.3, is still much higher than the power in the signal. While this process shows a reduction in the amount of error in the solution, what significance does this have if the error is still larger than the signal? To answer this question, it can be instructive to look at the errors in the spectral domain, as a function of degree. Figure 4.6 shows the power in the hydrology and ice signals, along with the error in recovering those signals for the case of one pair of satellites at 315 km altitude. This plot compares the error when a standard solution strategy is employed (no two-day gravity field estimates), and when two-day 10x10 gravity fields are estimated. The plot on the left is when no post-processing on the gravity solutions is performed, and the plot on the right is after the solutions have been destriped via *Swenson and Wahr* [2006], and smoothed with a 300 km Gaussian smoothing radius.

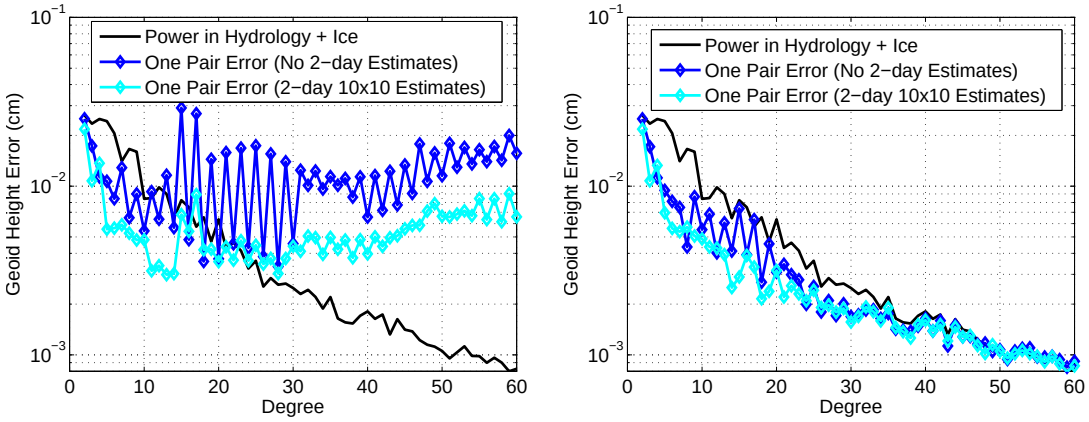

Figure 4.6: Error as a function of degree for one pair of satellites at 315 km altitude showing the effect of estimating a 10x10 gravity field every 2 days with no post-processing (left), and destriped and smoothed with a 300 km Gaussian smoothing radius (right)

The left plot in Figure 4.6 shows that the error curve for the case of not estimating any two-day gravity fields more or less exceeds the power in the signal at degree 14 (1500 km half-wavelength). When 10x10 gravity fields are estimated every two days, the error curve more or less exceeds the power in the signal at degree 22 (900 km half-wavelength). Thus, the spatial resolution of the gravity fields on a global scale has been improved from approximately 1500 km to 900 km. When the solutions are destriped and smoothed, the right plot of Figure 4.6 shows that much of

the error in the solution at higher degrees is diminished. This is due to the downweighting of higher degree coefficients and is a direct consequence of smoothing the solutions. It is seen that the error curve does not intersect with the power in the signal until approximately degree 40 (500 km half-wavelength), thus improving the spatial resolution in the gravity fields over what is provided by estimating two-day 10x10 fields. This indicates that it would simply be a waste of resources to estimate two-day gravity fields given a single pair of polar satellites, since one can ultimately obtain solutions with better spatial resolution simply by destriping and smoothing them.

4.5.2.2 Two Pairs of Polar Orbiting Satellites

It was shown in Section 4.5.1.1 that two pairs of satellites both in polar orbits are capable of providing daily estimates of the gravity field to low degree and order. Table 4.5 shows the spatial RMS of the errors in determining hydrology, ice mass variations, and OBP signals for different degrees of daily estimates for a 19-day gravity field solution. All numbers are expressed in cm of EWH.

Degree of Daily Estimate	**Hydrology RMS = 4.73**	**Ice RMS = 2.08**	**OBP RMS = 2.65**
none	8.73	8.91	9.84
6	4.58	3.31	4.89
10	4.61	3.23	4.66
14	5.12	3.13	5.27
18	4.83	2.97	4.70
22	5.43	2.95	5.38

Table 4.5: Spatial RMS of errors for two pairs of polar orbiting satellites at 315 km altitude using different degrees of daily estimates of the gravity field. Results are truncated at degree 60 and represent 19 days of data. Units are in cm of EWH.

Table 4.5 shows that estimating a 10x10 gravity field each day provides a 47% reduction in the level of errors in determining hydrology, a 64% reduction in ice mass variation errors, and a 53% reduction in OBP errors. It should be noted that the level of error in determining hydrology is approximately equal to the amount of power in the signal, but the error in determining ice mass

variations and OBP is still higher than the power in the signal.

Figure 4.7 examines the error in the spectral domain as a function of degree. The plot on the left is for no post-processing of the data and the plot on the right is when the solutions have been destriped and smoothed with a 300 km Gaussian averaging radius. The case of not making any daily estimate of the gravity field is compared with the case of estimating daily 10x10 gravity fields.

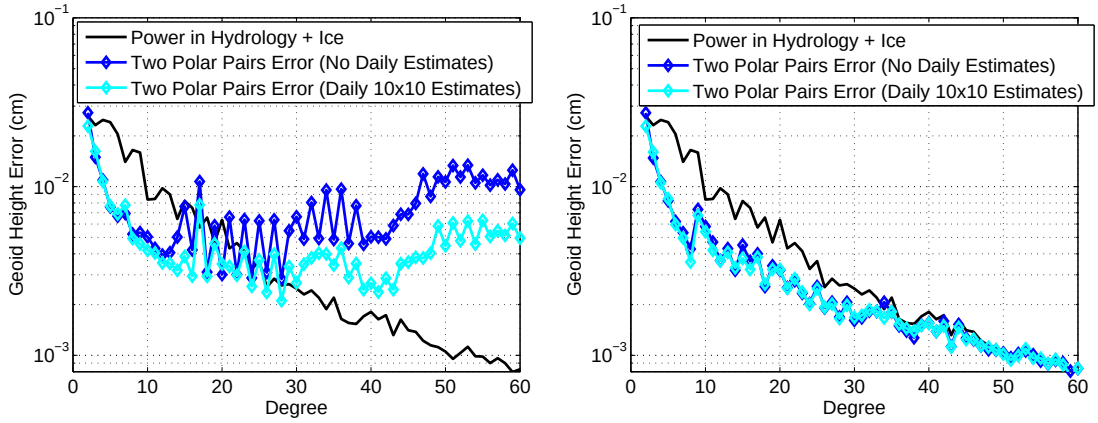

Figure 4.7: Error as a function of degree for two polar pairs of satellites showing the effect of estimating 10x10 gravity fields every day with no post-processing (left), and destriped and smoothed with a 300 km Gaussian smoothing radius (right)

The left plot in Figure 4.7 shows that when no daily estimates are made, the error exceeds the power in the signal at approximately degree 22 (900 km half-wavelength). When daily 10x10 gravity fields are estimated, the error exceeds the power in the signal at more or less degree 28 (700 km half-wavelength). This indicates the improvement in spatial resolution that estimating daily 10x10 gravity fields provides. However, the plot on the right shows that when the solutions are destriped and smoothed, any benefit that estimating the daily 10x10 gravity fields provided is eliminated, with both solutions performing equally. Additionally, destriping and smoothing the solutions has improved the spatial resolution globally over what estimating daily gravity fields provides, showing that the signal and error curves intersect at approximately degree 40 (500 km half-wavelength). Again, this indicates for the case of two polar pairs, this technique has no practical applications.

While it has been shown that destriping and smoothing the solutions reduces the benefit

that estimating daily gravity fields provides, one might ask if this is a necessary step. Figure 4.8 shows the spatial representation of the hydrology and ice signals we are trying to recover along with the recovered signals, truncated at degree and order 60, for the case of two polar orbiting pairs of satellites. Shown are the 19-day average of the truth hydrology and ice signals (top-left), the recovered signals after being destriped and smoothed (top-right), the recovered signal with no post-processing and without estimating daily gravity fields (bottom-left), and the recovered signal when daily 10x10 gravity fields are estimated (bottom-right). Figure 4.9 shows the same spatial representation for recovering OBP signals.

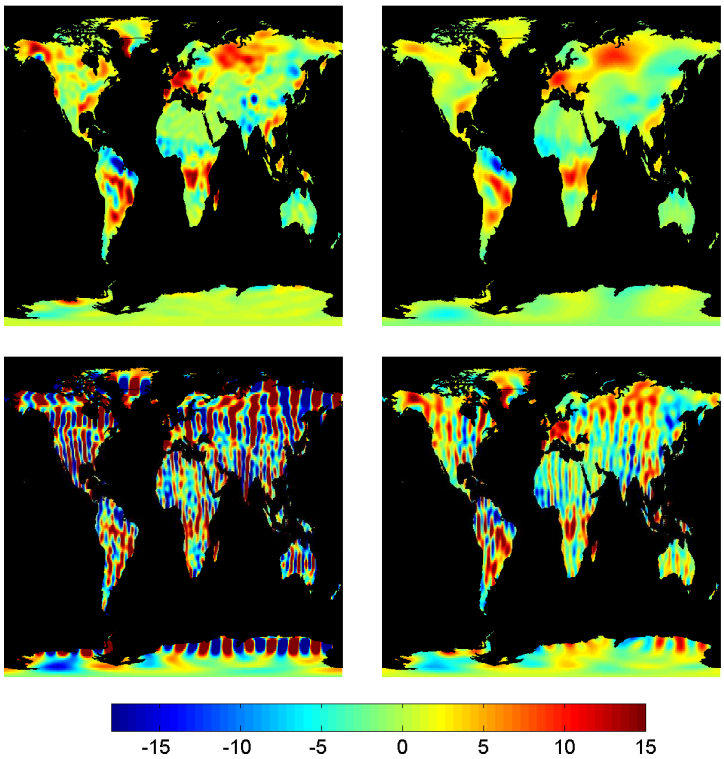

Figure 4.8: 19-day average of the truth hydrology and ice signals (top-left), recovered signals after destriping and smoothing (top-right)), making no daily estimates (bottom-left), and while estimating daily 10x10 gravity fields each day (bottom-right). Units are in cm of EWH, and results are truncated at degree 60.

While estimating daily 10x10 gravity fields greatly reduces the level of error in recovering hydrology, ice, and OBP signals, it is seen that there are a substantial amount of stripes left in the

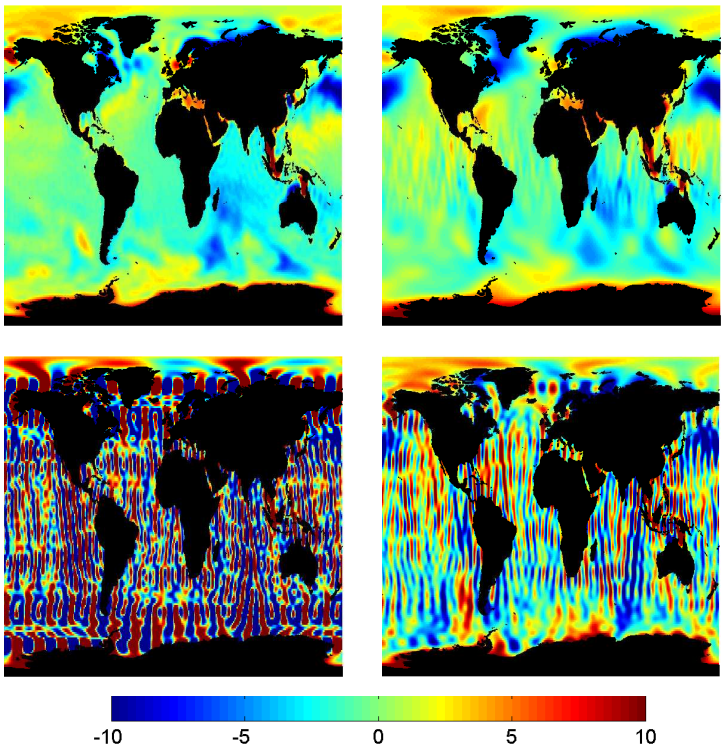

Figure 4.9: 19-day average of the truth OBP signals (top-left), recovered signals after destriping and smoothing (top-right)), making no daily estimates (bottom-left), and while estimating daily 10x10 gravity fields each day (bottom-right). Units are in cm of EWH, and results are truncated at degree 60.

solutions. The destriped and smoothed solutions have substantially less error in them and are a more accurate representation of the truth signal, agreeing with the results presented in Figure 4.7. Thus, estimating daily gravity fields does not improve the spatial resolution over what is offered by simply destriping and smoothing for the case of two polar pairs of satellites. While Figure 4.8 shows the signals out to degree 60, one could truncate at a lower degree, say degree 30, which is approximately where the signal and error curves intersect in the left plot of Figure 4.7 for the case of estimating daily 10x10 gravity fields. If this were done, it is found that the solutions do not need to be destriped and smoothed when daily gravity solutions are estimated; however, the extra spatial resolution that destriping and smoothing provides is sacrificed.

Similar spatial plots could be shown for the case of one pair of satellites, as discussed in Section 4.5.2.1, but results are similar to those shown in Figure 4.8, only with larger errors.

4.5.2.3 Two Satellite Pairs: One Polar + One Lower Inclined

Section 4.5.1.1 showed that a polar pair of satellites coupled with a lower inclined pair of satellites was able to estimate low degree and order gravity fields on a daily time scale. Furthermore, this was the most capable type of architecture, able to estimate daily gravity fields to the highest degree with lower errors than the other cases considered.

Table 4.6 shows the spatial RMS of the errors in recovering hydrology, ice mass variations, and OBP signals. Like previous results, units are in cm of EWH and all results are truncated at degree and order 60.

Degree of Daily Estimate	**Hydrology RMS = 4.73**	**Ice RMS = 2.08**	**OBP RMS = 2.65**
none	2.93	6.47	3.33
6	3.11	5.40	3.35
10	2.97	5.35	3.18
14	2.81	4.28	2.90
18	1.97	4.00	2.28
22	2.28	3.15	2.38

Table 4.6: Spatial RMS of errors for two pairs of satellites (one polar + one lower inclined) using different degrees of daily estimates of the gravity field. Results are truncated at degree 60 and represent 19 days of data. Units are in cm of EWH.

The results in Table 4.6 are different than those for one pair of satellites and two pairs of polar orbiting satellites in that the level of error when not estimating any daily gravity fields is quite low. In fact, the level of error in hydrology is lower than the power in the signal. This attests to the benefit of having East-West information in the gravity field solution. When 18x18 gravity fields are estimated each day, the errors in recovering hydrology are reduced by 33%, the errors in recovering ice mass variations are reduced by 38%, and the errors in recovering OBP signals are reduced by 32%. While this is a more modest reduction in the percentage of the errors over the other cases considered, the absolute level of error is substantially lower.

Figure 4.7 examines the error in the spectral domain as a function of degree. The plot on the left is for no post-processing of the data and the plot on the right is when the solutions have

been destriped and smoothed with a 300 km Gaussian averaging radius. The case of not making any daily estimate of the gravity field is compared with the case of estimating daily 18x18 gravity fields.

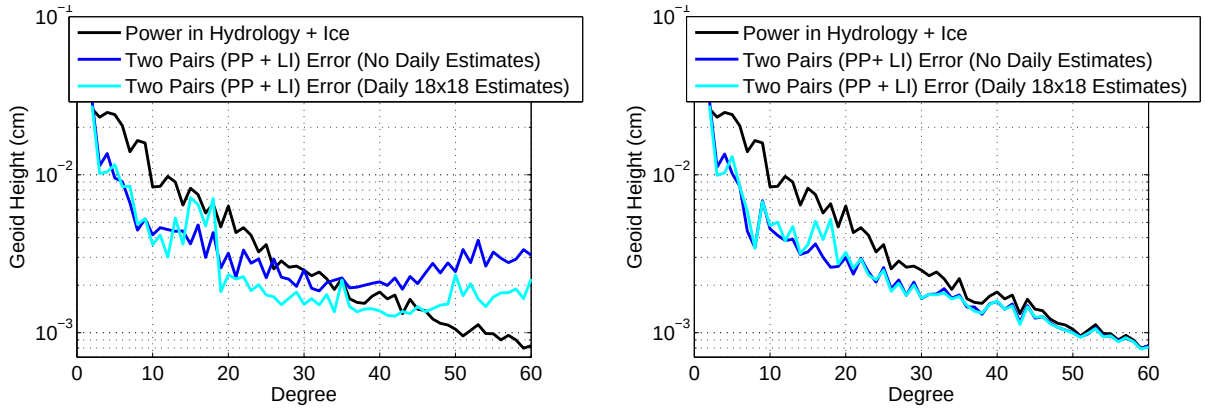

Figure 4.10: Error as a function of degree for a polar pair of satellites coupled with a lower inclined pair of satellites showing the effect of estimating a 18x18 gravity field every day with no post-processing (left), and destriped and smoothed with a 300 km Gaussian smoothing radius (right)

Figure 4.10 shows the spatial resolution in the estimated gravity fields is approximately 570 km, and improves to 440 km when daily 18x18 gravity fields are estimated. Destriping and smoothing affects each solution similarly as it did the previous two cases: the spatial resolution of the destriped and smoothed solution is shown to be roughly 500 km (corresponding to degree 40). This indicates that estimating daily 18x18 gravity fields offers a slight improvement in spatial resolution over what is offered by simply destriping and smoothing for the case of a polar pair of satellites coupled with a lower inclined pair of satellites.

To gain a better insight into this, Figure 4.11 shows the spatial representation of the 19-day average of the truth hydrology and ice signals (top-left), along with the recovered signals for destriped and smoothed solutions (top-right), no post-processing and without making daily estimates of the gravity field (bottom-left), and after estimating daily 18x18 gravity fields (bottom-right). Figure 4.12 shows the same series of plots only for recovering OBP signals. The plots are represented to degree and order 60 and are displayed in cm of EWH.

Figures 4.11 and 4.12 show improvements in determining hydrology, ice mass variations,

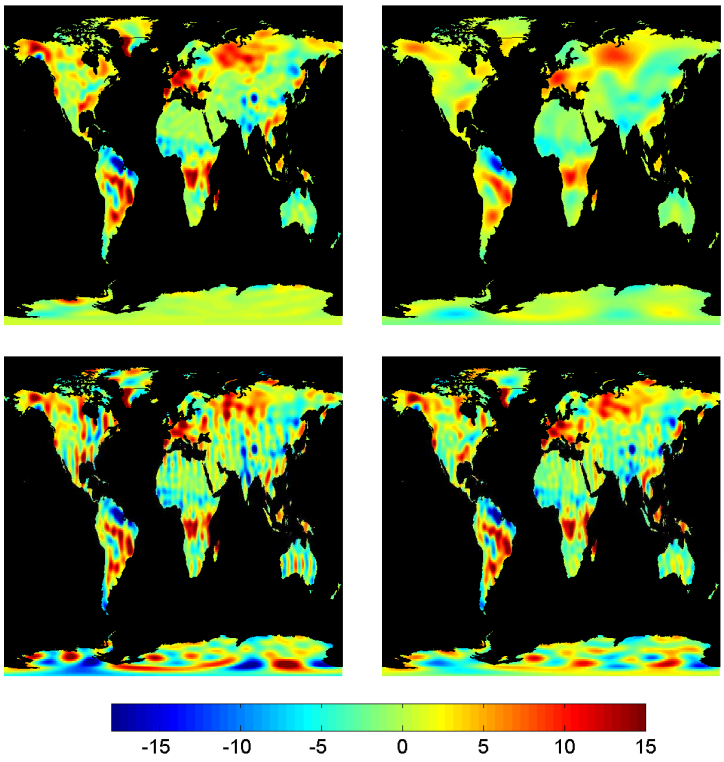

Figure 4.11: 19-day average of the truth hydrology and ice signals (top-left), recovered signals after destriping and smoothing (top-right)), making no daily estimates (bottom-left), and while estimating daily 18x18 gravity fields each day (bottom-right). Units are in cm of EWH, and results are truncated at degree 60.

and OBP signals when daily 18x18 gravity fields are estimated. Both longitudinal stripes and spurious errors (particularly at high latitude regions) are reduced by making the daily estimates. The solutions obtained when estimating daily 18x18 gravity fields are superior to those obtained after destriping and smoothing, as much more spatial information is retained (for instance, see North America and Greenland in Figure 4.11). This illustrates the very important fact that given a mission architecture consisting of a polar pair coupled with a lower inclined pair, one gains two substantial advantages : (1) the quality of the solution is intrinsically better due the addition of the East-West information (seen by comparing Figures 4.11 and 4.8), and (2) by estimating daily 18x18 gravity fields, the quality of the solution can be improved to such a level that destriping and smoothing the solutions is no longer necessary when examining hydrology and ice signals to

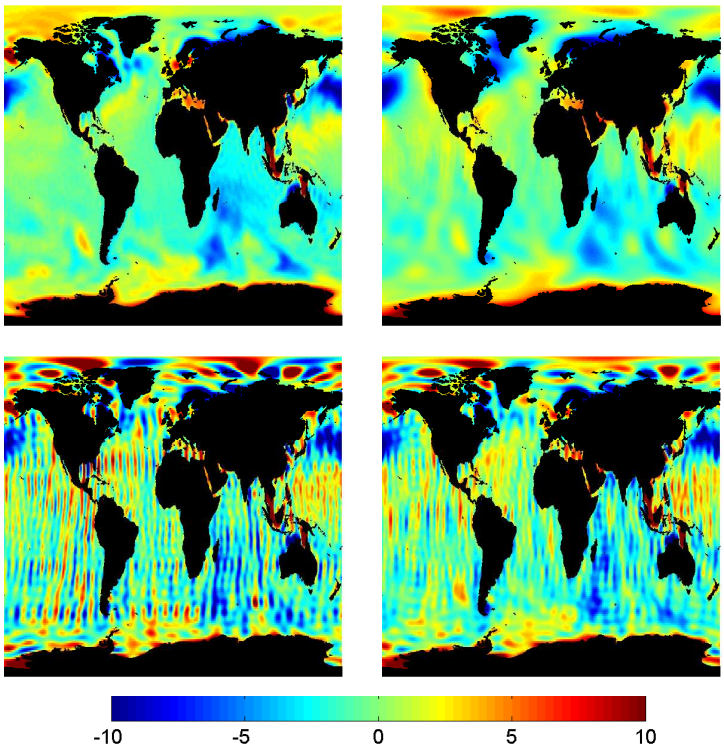

Figure 4.12: 19-day average of the truth OBP signals (top-left), recovered signals after destriping and smoothing (top-right)), making no daily estimates (bottom-left), and while estimating daily 18x18 gravity fields each day (bottom-right). Units are in cm of EWH, and results are truncated at degree 60.

degree and order 60 ($\sim$ 330 km). For OBP signals shown in Figure 4.12, one could argue that the destriped and smoothed solutions are superior to those provided by estimating daily 18x18 gravity fields. The reason that the stripes are more dominant in this case than the case of hydrology and ice signals, is that the magnitude of OBP signals is smaller, hence, we have smaller signal to noise ratios. It is found that applying a simple 200 km Gaussian averaging radius to the solution obtained after estimating daily 18x18 gravity fields provides much better results.

There is one more point which should be illustrated concerning these solutions. Figure 4.10 illustrates that when daily 18x18 gravity fields are estimated, degrees 16-18 actually have more error than if no daily estimates were made. To investigate this more thoroughly, the errors (difference between the truth and recovered) in each coefficient can be examined. Figure 4.13 shows the logarithm of the error in each coefficient for the three cases of not having any daily estimate,

estimating daily 14x14 fields, and estimating daily 18x18 fields. What is most striking in these plots is that once daily 18x18 gravity fields are estimated, the bands of error that are at multiples of the resonant order (16) diminish substantially. While this error is reduced considerably, the error in the coefficients near the resonant order in the daily estimates become extremely high, as is indicated in Figure 4.13. Thus, one gets substantial improvement at the higher degrees with a slight degradation in the coefficients near the resonant order.

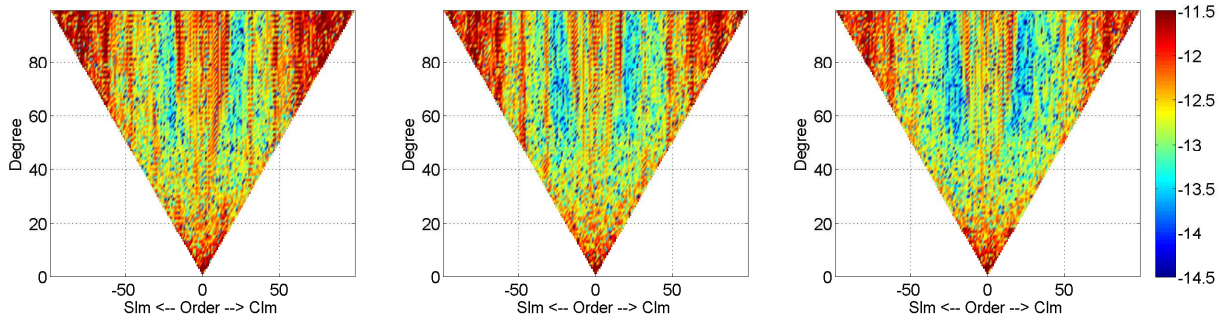

Figure 4.13: Logarithm of the actual error in each coefficient for no daily estimate (left), estimating a daily 14x14 (middle), and estimating a daily 18x18 (right)

This phenomena is also seen when showing the errors as a function of order of the gravity field, displayed in Figure 4.14. The first thing one notices are the large errors at multiples of the resonant order. Estimating daily 18x18 gravity fields reduces the error at the multiples of the resonant orders substantially.

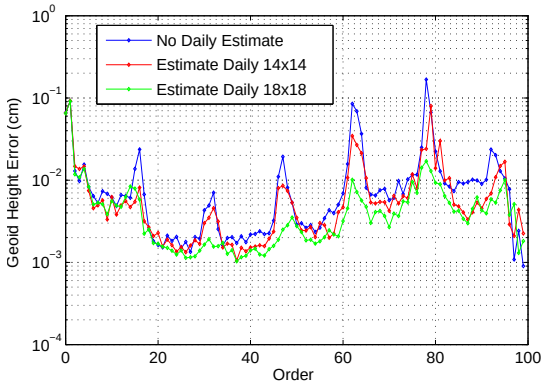

Figure 4.14: Error as a function of order when comparing different degrees of daily estimates using two pairs of satellites (one polar + one lower inclined)

In essence, when one extends the daily estimate to include the resonant order, the daily estimate of the near-resonant order coefficients becomes somewhat of a junk parameter. This is akin to the process of estimating once per revolution and twice per revolution terms in the gravity signal that most centers that process GRACE data employ. Since so much error manifests itself at these frequencies, these parameters are estimated and then thrown away. Thus, when the daily estimate includes the near-resonant order terms, a small number of spherical harmonic coefficients absorb much of the error that would otherwise go to the multiples of the resonant order terms at much higher degree. This could be partially attributed to the fact that on a daily time scale, the satellites are essentially in a 16/1 repeat mode with a resonance frequency at degree 16, hence, leading to the accumulation of error at this degree. Simply put, one gains an improvement at short wavelengths for a slight degradation at longer wavelengths.

It should be mentioned that one could also think of gaining additional benefits by varying constraints on the spherical harmonic coefficients. As was mentioned in Section 3.4, certain spacecraft state parameters are constrained during the estimation process via *Rowlands et al.* [2002], however no constraints are placed on the spherical harmonic coefficients. An optimal set of constraints could be developed for this procedure to enhance the solutions; however, this was not explored in the dissertation.

4.6 Conclusions

In this chapter, we investigated the effect that making high frequency/low resolution estimates of the gravity field has on mitigating temporal aliasing errors and improving the spatial resolution of the derived gravity field models. Three possible mission architectures were examined: one pair of polar orbiting satellites, two pairs of polar orbiting satellites, and one pair of polar orbiting satellites coupled with a lower inclined pair of satellites. Results showed that one pair of satellites does not have the ability to accurately estimate a low degree and order gravity field each day, but can estimate a low degree and order gravity field using two days of data. The quality of the two-day estimates is largely dependent on the homogeneity of the groundtrack coverage over two

days. Conversely, two pairs of satellites were shown to be able to estimate low degree and order gravity fields each day with adequate accuracy. The polar pair coupled with the lower inclined pair provides the most accurate estimates.

All cases considered showed substantial improvements in their ability to estimate hydrology, ice mass variations, and ocean bottom pressure signals when low resolution/high frequency gravity field estimates were made. It was shown that the process of estimating high frequency gravity fields is more effective when the satellites are at a lower altitude due to the increased sensitivity to the gravity field that flying at a lower altitude provides. The cases of one pair of satellites and two pairs of polar orbiting satellites provide anywhere between a 50% and 75% reduction in the level of errors in determining hydrology, ice mass variations, and ocean bottom pressure signals, by making two-day and daily estimates of the gravity field, respectively. The largest benefit was seen in estimating ice mass variations, as these regions have the most dense groundtrack coverage and temporal aliasing errors tend to be larger in the polar regions. While the percentage reduction in the level of errors for these cases is impressive, the overall level of errors is still larger than that of the signal, and many of the errors manifest themselves as longitudinal stripes in the solution. Thus, for use in the scientific communities, the solutions would most likely need to be destriped and smoothed via standard GRACE post-processing techniques, limiting much of the additional spatial information that making the low degree estimates of the gravity field at high frequencies provides.

The case of a pair of polar orbiting satellites coupled with a lower inclined pair of satellites making daily estimates provides a more modest reduction in the level of errors, with errors being reduced anywhere between 30% and 40% in recovering the signals of interest. The level of error is substantially lower than that of the other cases, however, showing the benefit that having East-West information provides to the solution. While this type of architecture by itself increases the accuracy of the gravity solutions over the other cases considered, we show that there is an additional advantage to having a polar pair and a lower inclined pair of satellites: the ability to further mitigate the effect of temporal aliasing errors by making daily low degree and order estimates of the gravity

field. Furthermore, when studying hydrology and ice mass variations, the gravity solutions would not need to be destriped or smoothed, greatly enhancing the spatial resolution of the solutions.

Chapter 5

Design Considerations for Two Satellite Pairs

5.1 Introduction

This chapter focuses on reducing temporal aliasing errors by increasing the sampling frequency of the mission through the addition of a second pair of satellites. In theory, if enough pairs of satellites were placed in proper orbits, one could sample the gravity field at a high enough frequency such that temporal aliasing errors would be largely eliminated. Having a dozen, if not more, satellite pairs to accomplish such a feat is cost-prohibitive at this point. As such, this work focuses on the more interesting question of optimizing the orbits of two pairs of satellites for recovering temporal gravity variations.

5.2 Orbit Design Considerations

The search space for this problem is extremely large, and is further complicated when considering that the selected orbits will be a strong function of the science goals of the mission. For instance, if the primary goal of the mission is to determine continental hydrology (excluding ice) at small spatial scales, then one might place the satellites in orbits with dense coverage over these regions, but less coverage over the polar regions. This would most likely result in decreased sensitivity to determining ice mass variations in Greenland and Antarctica. However, if the primary science objective is to determine ice mass variations in Greenland, then a different mission architecture would be selected. This study assumes that the science goals of the mission are to determine continental hydrology, ice mass variations, and ocean bottom pressure signals over the entire globe

with as high spatial resolution as possible, with each area of science being weighted equally.

Considering strictly the satellite orbits, one can characterize the mission performance, P, given two pairs of collinear satellites, via the following:

$$P = f(X_1, X_2, \Delta\nu_1, \Delta\nu_2, L). \tag{5.1}$$

In Equation 5.1, X_1 and X_2 are the state (position and velocity) of the lead spacecraft of the first and second pair of satellites, respectively, $\Delta\nu_1$ and $\Delta\nu_2$ are the separation distances between the first and second pairs of satellites, respectively, and L is the amount of time that data are collected. It is most convenient to represent the state of the spacecraft in terms of mean Keplerian orbital elements, given in Equation 5.2.

$$\begin{aligned} X_1 &= f\left(a_1, e_1, i_1, \Omega_1, \omega_1, \nu_1\right) \\ X_2 &= f\left(a_2, e_2, i_2, \Omega_2, \omega_2, \nu_2\right) \end{aligned} \tag{5.2}$$

Here, a is the semimajor axis, e is the eccentricity, i is the inclination, Ω is the longitude of ascending node, ω is the argument of perigee, and ν is the true anomaly. Coupling Equations 5.1 and 5.2, one can see that the mission performance of this type of architecture will be directly related to 15 parameters. Adding additional satellites pairs will increase the number of variables by seven for each pair of satellites added. It is desirable to reduce the number of independent variables and narrow down the search space by making appropriate assumptions.

First, the inter-satellite separation distances, defined as $\Delta\nu_1$ and $\Delta\nu_2$, will likely be chosen based on the satellite-to-satellite ranging instrument requirements. Future missions are likely to use a laser interferometer, for which a 100 km separation distance is chosen as a trade-off between instrument performance as well as relative accuracy in determining short wavelength and long wavelength features in the gravity field [*Wiese et al.*, 2009]. Fixing this distance allows us to eliminate two of the variables, $\Delta\nu_1$ and $\Delta\nu_2$, from the search space.

Next, it can be assumed that the spacecraft should fly in circular orbits to minimize any relative changes in distance due to having eccentric orbits, as GRACE does. Fixing the eccentricity to zero eliminates two additional parameters.

Given circular orbits, the argument of perigee, ω, becomes ill-defined. Hence, we can now define the argument of latitude, u, which is equal to the sum of the true anomaly and the argument of perigee ($u = \omega + \nu$). The argument of latitude defines the position of the satellite in its orbit about the Earth with respect to Ω. While this is a parameter that could have an effect on the gravity solution, it is impossible to determine what the optimal satellite position should be due to the extremely complex nature of the problem. For example, it would be optimal if, during a flooding event, the satellite flew over the region of interest. However, it is impossible to know when this event might occur in the future, making it very difficult to optimize.

While optimizing u_1 and u_2 independently is not feasible, one could think of optimizing the relative difference in the argument of latitude between the two pairs of satellites in an effort to meet certain temporal groundtrack crossing constraints (i.e., the second satellite pair will fly over a location on the Earth a specified amount of time after the first satellite pair flew over the same location). The same argument holds for the longitude of ascending node, Ω, in a spatial sense. That is, in an absolute sense it is impossible to determine what the optimal values for Ω_1 and Ω_2 should be, since we cannot predict the time and location of mass variations on the Earth years in advance. However, the relative difference between the ascending nodes of the two pairs of spacecraft could be optimized to provide a required spatial constraint on the combined groundtrack pattern of the two satellite pairs. Thus, Ω_1 and Ω_2, along with u_1 and u_2 can be reduced to two new parameters: $\Delta\Omega_{12}$, and Δu_{12}. The first, $\Delta\Omega_{12}$, provides a spatial constraint on the groundtrack pattern of the two satellite pairs while the second, Δu_{12} provides a temporal constraint on the groundtrack pattern. It is expected that Δu_{12} can only be optimized if the periods of both satellites pairs are equal to each other, which would require that $a_1 = a_2$. Otherwise, there will be a secular drift rate in the time that the two pairs of satellites cross the same location on the Earth which cannot be controlled.

Next, we can consider the inclination of the satellites. In order to provide global coverage of the Earth, at least one of the pairs of satellites must be in a near-polar orbit. Thus, this can be set as a constraint. The inclination of the second pair of satellites, however, is free to vary.

The problem has now been reduced from one with 15 parameters to one with only six, and can be represented via the following:

$$P = f(a_1, a_2, i_2, \Delta u_{12}, \Delta\Omega_{12}, L). \tag{5.3}$$

Let us now discuss the semimajor axis of the two pairs of satellites. As shown in Equation 2.10, the gravitational potential is proportional to r^{-n}; hence, one is more sensitive to the potential at lower altitudes. As discussed in Section 1.4, it is envisioned that future GRACE-type missions will also employ drag-free technology, allowing one to fly at a lower altitude with increased sensitivity to short wavelength features in the gravity field. With this in mind, one can set a minimum bound on the altitude of the spacecraft which depends on many factors, including, but not limited to: the design lifetime of the satellites, the amount of propellant available, the type of thrusters used, the cross-sectional area of the spacecraft, and the magnitude of the atmospheric density. Some work has been done to this end, by *Marchetti et al.* [2008] and *St. Rock et al.* [2006], examining the performance of drag-free control systems in low-Earth orbit, and the mission lifetimes associated with various thrusters. Figure 5.1 depicts the results from each respective paper, along with the initial estimate for the GOCE mission, assuming the same initial mass propellant fraction as the GRACE mission (0.18). Note that the results from *St. Rock et al.* [2006] have been scaled down by a factor of two to account for variable specific impulse and control system use that was not considered in the analysis.

Figure 5.1 illustrates that a 290 km altitude allows the satellites to remain in orbit for 10 years; thus, this was selected as the minimum altitude for this study. Note that this calculation is very approximate, and a rigorous analysis of a control system in the appropriate environment would need to be made to refine the targeted altitude; however, it is valid as a first-order approximation and sufficient for the purposes of this study.

The last parameter which needs to be discussed from Equation 5.3 is L, the length of time that data are collected. The parameter L will depend primarily on the targeted spatial and temporal

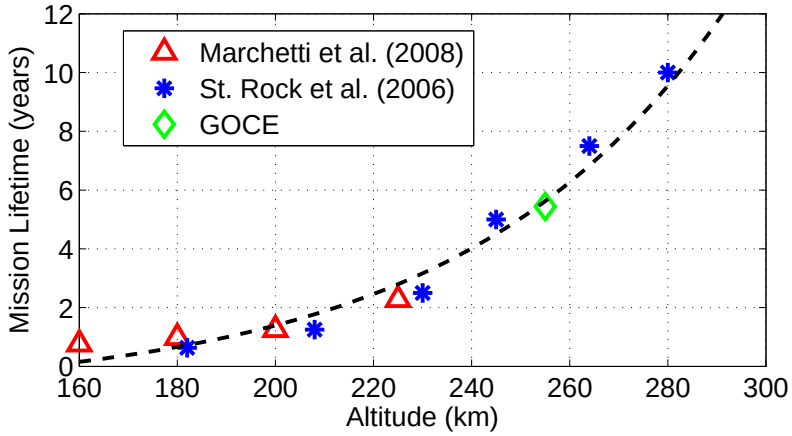

Figure 5.1: Mission lifetime as a function of altitude assuming an initial mass propellant fraction of 0.18

resolution of the mission. In principle, the product of the spatial resolution and temporal resolution of a mission is constant; that is, given a fixed number of satellite pairs, one cannot improve the spatial resolution without sacrificing temporal resolution and vice-versa [*Dirac*, 1958; *Visser et al.*, 2010]. As discussed in Section 4.4, given homogeneous groundtrack spacing, the spatial resolution of a mission can be approximated by the Colombo-Nyquist rule, which states the maximum resolvable degree of the gravity field is equal to half of the number of orbital revolutions of the satellites [*Colombo*, 1984], guaranteeing gravity solutions that are homogeneous in longitude [*Visser et al.*, 2011]. While larger values of L theoretically lead to better spatial resolution, they also allow for greater accumulation of temporal aliasing errors. While some steps can be taken to mitigate the effect of temporal aliasing errors, such as co-estimating high frequency/low resolution gravity fields as discussed in Chapter 4, varying the L parameter should lend insight into proper trade-offs between increasing the spatial resolution of the solutions and mitigating the effect of temporal aliasing errors.

There is one more point to be mentioned concerning L. One drawback of GRACE is the lack of an altitude control system. This leads to variability in the groundtrack pattern of GRACE, and subsequent variability in the quality of the monthly solutions. This was discussed in *Klokocnik et al.* [2008] and *Wagner et al.* [2006], showing the degradation in gravity solutions from GRACE

in the fall of 2004 when the satellites passed through a 61/4 resonance orbit. Due to the success of the GOCE mission implementing a drag-free system and maintaining a constant orbital altitude, it seems advantageous to consider only repeat groundtracks for future missions. Imposing this constraint assures consistent quality in the time-variable gravity solutions.

From *Kaula* [1966], even zonal coefficients in addition to a nonlinear $(J_2)^2$ contribute to the secular rate of the node, $\dot{\Omega}$. However, all terms are second order when compared to the contribution of J_2, thus, we design the repeat groundtracks by considering only this term. Given a desired eccentricity and inclination, there are only certain values for the semimajor axis which will satisfy the conditions for a repeating groundtrack. One can obtain the appropriate values for semimajor axis, a, by solving the following equation [*Vallado*, 2001]:

$$C_2 a^{7/2} + C_1 a^2 + C_0 = 0, \tag{5.4}$$

where

$$\begin{aligned} C_2 &= \frac{l}{k}\omega_e \\ C_1 &= -\sqrt{\mu} \\ C_0 &= \frac{\alpha}{4\epsilon^4}\left[\frac{l}{k}2\cos i + 1 - 5\cos^2 i - \left(3\cos^2 i - 1\right)\epsilon\right], \end{aligned} \tag{5.5}$$

in which

$$\begin{aligned} \alpha &= 3\sqrt{\mu}J_2 r_e^2 \\ \epsilon &= \left(1 - e^2\right)^{\frac{1}{2}}. \end{aligned} \tag{5.6}$$

In these sets of equations, μ is the gravitational constant of the Earth, J_2 is the negative of the unnormalized C_{20} coefficient describing the oblateness of the Earth, ω_e is the rotation rate of the Earth, k is the desired number of nodal days it takes for the satellites to repeat, and l is the number of orbital revolutions the satellites perform in k nodal days. It should be noted that k/l must be irreducible, and l is given by

$$l = \frac{k\left(\dot{\omega} + \dot{M}\right)}{\left(\omega_e - \dot{\Omega}\right)}, \tag{5.7}$$

with

$$\dot{\Omega} = \frac{-3}{2}\frac{\sqrt{\mu}J_2 r_e^2 \cos i}{(1-e^2)^2 a^{\frac{7}{2}}}, \tag{5.8}$$

$$\dot{\omega} = \frac{3}{4}\frac{\sqrt{\mu}J_2 r_e^2 \left(5\cos^2 i - 1\right)}{(1-e^2)^2 a^{\frac{7}{2}}}, \tag{5.9}$$

$$\dot{M} = \frac{\sqrt{\mu}}{a^{\frac{3}{2}}} + \frac{3}{4}\frac{\sqrt{\mu}J_2 r_e^2 \left(3\cos^2 i - 1\right)}{(1-e^2)^{\frac{3}{2}} a^{\frac{7}{2}}}. \tag{5.10}$$

Here, $\dot{\Omega}$, $\dot{\omega}$ and $\dot{M}$ are the secular drift rates of the longitude of ascending node, argument of perigee, and mean anomaly, respectively, due to the oblateness of the Earth considering only the effect of J_2. Note that all Keplerian orbital elements used thus far, including the new semimajor axis, are in mean element space; that is, they are mean orbital elements. All Keplerian orbital elements then need to be converted to osculating elements prior to propagation via *Brouwer* [1959]. This accounts for short term periodic variations in the orbit due to J_2, and allows for the groundtrack to keep its repeat pattern.

Thus, selecting a particular value for L inadvertently imposes an additional constraint on either a_1 or a_2: that the value for a must put the satellite in a repeat orbit. It is not imperative that both satellite pairs have a value of k equal to that of L, but one pair must. It has been pointed out by *Bender et al.* [2008] that perhaps the most effective way to design the architecture would be to have a lower inclined pair in a longer repeat period (RP) coupled with a polar pair of satellites in a shorter RP. This would lead to more homogeneous spacing in the combined groundtrack pattern of the two pairs of satellites, since, by nature, groundtracks are more dense over the poles than the equator. In this scenario, the lower inclined pair would be selected to have a value of k equal to L, while the RP of the polar pair of satellites would be allowed to vary, but would be constrained to be less than that of the lower inclined pair. Thus, all such combinations should be explored.

Finally, taking into consideration the above discussion, Equation 5.3 can be rewritten as

$$P = f(k_1, k_2, i_2, \Delta u_{12}, \Delta\Omega_{12}). \tag{5.11}$$

In Equation 5.11, k_1 is the RP of the polar pair of satellites and k_2 is the RP of the other pair of satellites for which the inclination can vary. Note that the additional constraints which are imposed are that $k_2 = L$ and that $k_1 \leq k_2$. One additional caveat that should be mentioned is that k is expressed in units of nodal days, while L is typically expressed in units of solar days, since the data processing is usually set up to handle daily batches of data. This means that typically a solution will have slightly more data (a few hours) than what is taken during the full repeat period of the satellites. Table 5.1 is a list of all constraints that were imposed to arrive at Equation 5.11.

Parameter	**Constraint**
a_1,a_2	290 km minimum; Repeat Groundtrack
e_1,e_2	0 (Circular Orbits)
i_1	90^o
$\Delta\nu_1$, $\Delta\nu_2$	100 km
L	$L = k_2$; $k_1 \leq k_2$

Table 5.1: Constraints imposed on design criteria to reduce the search space for an optimal architecture

Using the constraints listed in Table 5.1, Equation 5.11 has been reduced from one that initially was a function of 15 variables to one that is now a function of only five variables. Furthermore, it is expected that the values selected for k_1, k_2, and i_2 will have the most influence on how well the mission performs. Δu_{12} and $\Delta\Omega_{12}$ are expected to have much smaller impacts.

It should further be stressed that this type of analysis is considerably biased towards the minimum altitude chosen, in this case, 290 km. To illustrate this, Figure 5.2 shows the closest altitude to 290 km (without going below it) for different values of k_1.

Figure 5.2 illustrates how results could be biased towards the minimum allowable altitude. For example, the closest 8-day RP groundtrack to 290 km exists at an altitude of 291 km, versus 374 km for a 12-day RP. The lower altitude given by the 8-day RP orbit could trump any benefit that collecting data for 12 days versus 8 days might add.

The same analysis can be done if one fixes a value for k_2, but lets i_2 vary. Figure 5.3 shows how the altitude necessary to maintain a 17-day RP orbit changes as a function of inclination.

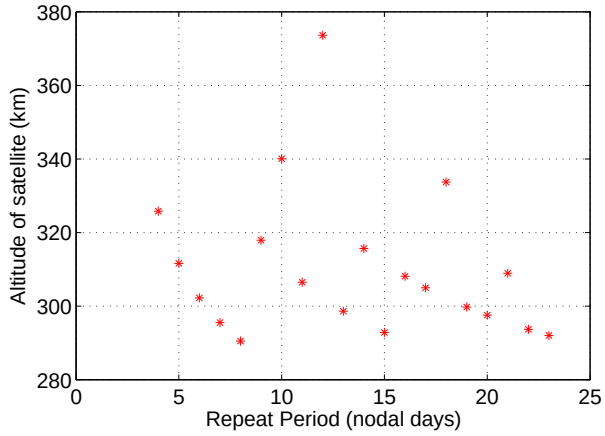

Figure 5.2: Necessary altitude to maintain specific repeat periods for a polar pair of satellites

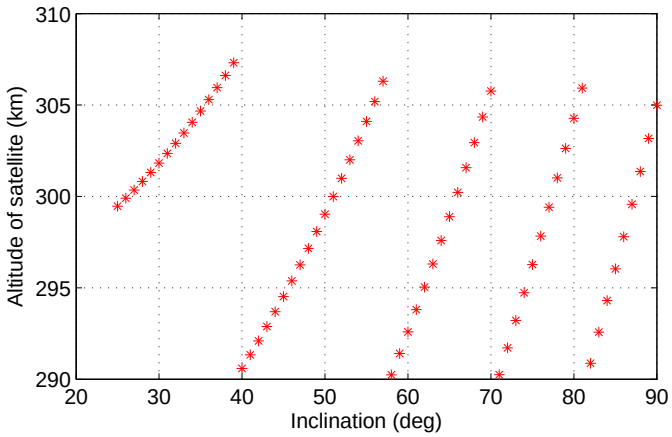

Figure 5.3: Necessary altitude to maintain a 17-day repeat period at different inclinations

Hypothetically speaking, if a 70^o inclination were an optimal value for i_2 speaking strictly in terms of inclination, Figure 5.3 suggests that this study might find that a 71^o inclination is the optimal value for i_2 since this orbit is 16 km lower in altitude than the orbit with a 70^o inclination. This analysis shows how the altitude, repeat period, and inclination are inherently coupled together, and an optimal set of orbital parameters will be a strong function of the mission constraints.

5.3 Methodology

Due to the unpredictable nature of various force models (hydrology, atmosphere, ocean, tides, ice), and the temporal aliasing errors that are associated with them, it was determined that performing a Monte-Carlo analysis using numerical simulations was the most effective way to approach this problem. The primary parameters of interest in Equation 5.11 are k_1, k_2, and i_2. The following are the ranges of values explored for these parameters:

$$k_1, k_2 = [4, 23] \text{ days; } k_1 \leq k_2 \tag{5.12}$$

$$i_2 = [25^o, 90^o] \tag{5.13}$$

A step size of 5^o was used in exploring the range of values for i_2. After the initial results narrowed down a more appropriate range of values for i_2, then a 1^o step size was used. Examining the ranges given in Equations 5.12 and 5.13, one can calculate that 2,940 simulations are necessary to cover the entire search space of the k_1, k_2, and i_2 variables.

Numerical simulations were run via the process described in Section 3.4 using the simulation detailed in Table 3.1. The computation time associated with such a large matrix of simulations is expensive, and increasing the degree of estimation exponentially increases the processing time. As such, a subset of simulations was carried out to both degree 60 and degree 100 to ensure consistency between the two, in hopes of being able to run the matrix of simulations to degree 60. It was expected that the two would correlate; however, the results were surprising, showing smaller correlations than expected. This is discussed in detail in Section 5.4.1. As a result, all simulations were run to degree and order 100.

As discussed in Section 2.3, there are a host of techniques which can be used to quantify the performance P of a gravity recovery satellite mission. P depends substantially on what the scientific goals of the mission are. For this study, we took the liberty of defining the scientific goals of the mission to be increasing the spatial resolution of the recovered hydrology, ice, and ocean bottom pressure signals as much as possible. Each area of science is weighted equally; hence, one

hopes to minimize the error, E, given by

$$E = \frac{E(H) + E(I) + E(O)}{3} \tag{5.14}$$

In Equation 5.14, $E(H)$ represents the error in determining hydrology, $E(I)$ is the error in determining ice mass variations, and $E(O)$ is the error in determining ocean bottom pressure signals. There are many methods and tools which one can use to analyze error and quantify $E(H)$, $E(I)$, and $E(O)$ on both global and regional scales. While regional metrics are preferred, this study is already computationally expensive. It is therefore desirable to use a global metric to quantify E to narrow down the search space and identify a select few mission architectures for further analysis on a regional scale. Since the end user is primarily interested in performance in the spatial domain, it was decided that a spatial RMS (discussed in Section 2.3.1.2 would be used to calculate $E(H)$, $E(I)$, and $E(O)$. While this is not a perfect representation for the performance of a mission by itself, it does give a very good indication of how changing k_1, k_2, and i_2 affects the ability of the satellites to recover the geophysical signals that we are interested in.

Figure 5.4 illustrates how E is calculated, showing the truth signals (left), recovered signals (middle), and error (right), for recovering both hydrology and ice mass variations (top), as well as ocean bottom pressure signals (bottom). This simulation is for a single pair of polar orbiting satellites in a 13-day RP at 299 km. The plots have been truncated at degree 60 and are expressed in cm of equivalent water height (EWH).

When calculating E, one uses the spatial plot of errors, given by the right set of plots in Figure 5.4. Furthermore, one can calculate the power in the truth signals, S, for hydrology ($S(H)$), ice mass variations ($S(I)$), and ocean bottom pressure ($S(O)$) in the same manner that the error is calculated in Equation 5.14. Table 5.2 illustrates the signal and error associated with Figure 5.4 in cm of EWH. In this case, the error exceeds that of the signal since the solutions have not been destriped and smoothed, as typically is done with data of this type.

Note that throughout this chapter, E is obtained by taking the solutions to degree 100 and truncating them at degree 60 to make the spatial maps. The reason for doing this is that it was

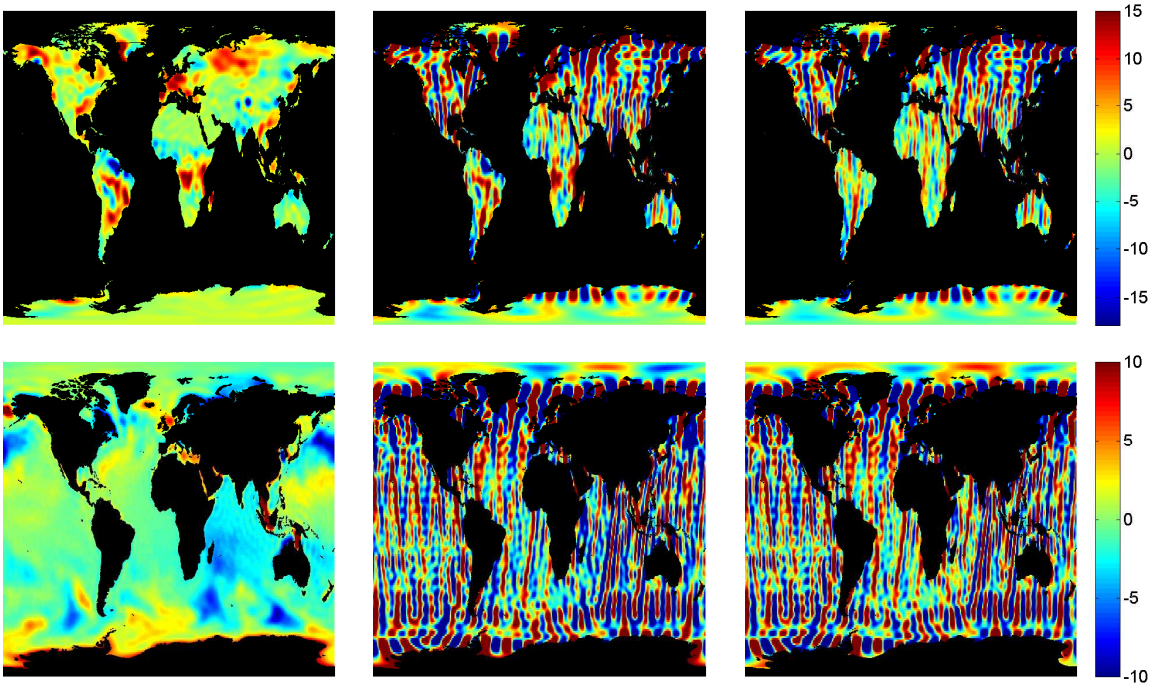

Figure 5.4: Truth signals (left), recovered signals (middle), and the error (right) for recovering hydrology and ice mass variations (top row of plots) and ocean bottom pressure signals (bottom row of plots) given a polar pair of satellites at 299 km in a 13-day repeating groundtrack. Units are in cm of equivalent water height.

	Signal (cm)	**Error (cm)**
Hydrology	$S(H) = 4.67$	$E(H) = 13.97$
Ice	$S(I) = 2.12$	$E(I) = 7.54$
Ocean	$S(O) = 2.46$	$E(O) = 11.04$
Total	$S = 3.08$	$E = 10.85$

Table 5.2: Signal and error associated with Figure 5.4. Units are expressed in cm of EWH.

found that if the results are truncated at degree 60, they generally do not need to be destriped or smoothed for the case of two satellite pairs, resulting in better spatial resolution than if they were.

5.4 Results

This section shows the most important results from the Monte-Carlo analysis in an effort to optimize k_1, k_2, and i_2. Additionally, Section 5.4.5 discusses groundtrack patterns obtained by tuning $\Delta\Omega_{12}$ and Δu_{12}. This section begins with a discussion on the impact of performing

simulations to degree 60 versus degree 100.

5.4.1 Degree of Estimation

It was found that the calculated error, E, varies substantially for certain cases depending on if the simulations are run to degree and order 60 or 100. To explain this, an example case is shown. When simulations are carried out to degree and order 60, one of the better performing mission architectures consists of a polar pair of satellites in an 8-day RP at an altitude of 291 km coupled with a lower inclined pair (72^o) in a 13-day RP at an altitude of 290 km. The error, E, from Equation 5.14, is calculated to be 4.64 cm EWH for this case. Conversely, when the simulations are extended to degree and order 100, but truncated at degree 60 for a fair comparison, the error is calculated to be 10.38 cm EWH. This contradicts the expected results that the error obtained from these two cases should be more or less commensurate with each other. To explain this result, Figure 5.5 presents the logarithm of the actual error in the coefficients as a function of degree and order.

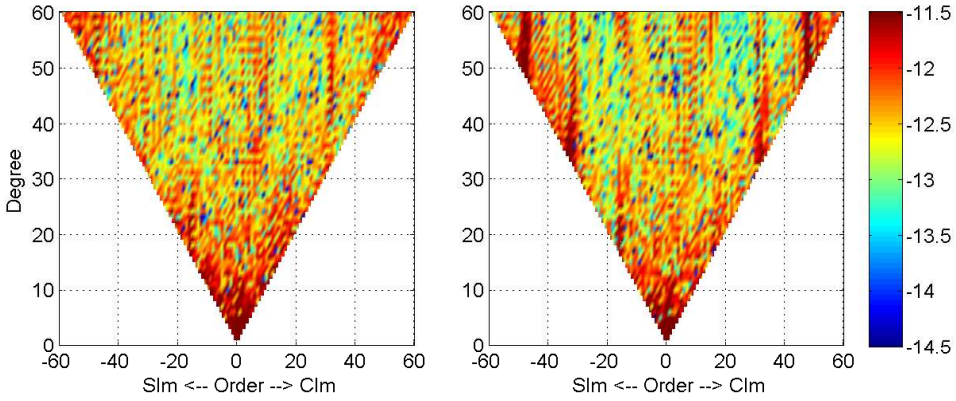

Figure 5.5: Logarithm of the error in the coefficients for a simulation carried out to degree 60 (left) and a simulation carried out to degree 100 (right)

Figure 5.5 shows that when the solution is extended to degree 100, large bands of error show up at two and three times the resonant order that do not exist in the degree 60 solutions. To study why this is the case, the covariance matrix can be analyzed. Figure 5.6 illustrates how

the C(51,51) coefficient is correlated with other coefficients, and was obtained by examining the covariance matrix of a gravity solution involving only the 8-day polar RP orbit over the 13 days of the mission simulation. Note that the correlations with all coefficients are not shown in the plot, as the correlations outside of the window shown are effectively zero, as expected.

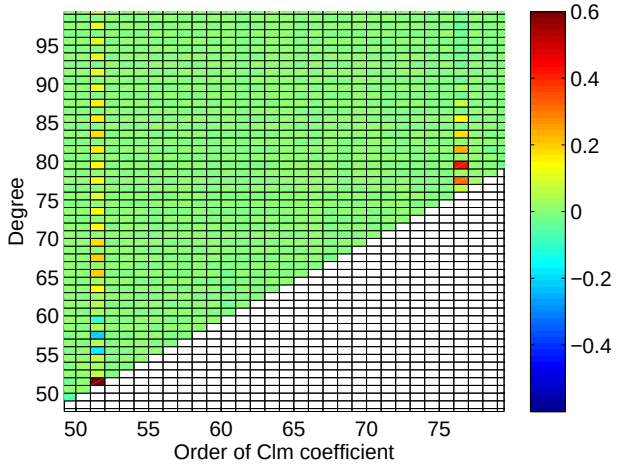

Figure 5.6: Correlations with the C(51,51) coefficient for an 8-day RP polar orbit

Given a spherical harmonic coefficient of a certain order, coefficients of the same order produce orbital element perturbations of identical frequency [*Kaula*, 1966], shown by the correlations at order 51 in Figure 5.6. In this peculiar case, however, the period of a near resonant perturbation at order $m = 51$ is identical to the period of a near-resonant perturbation at $m = 76$, which also manifests itself in Figure 5.6 via the correlations at $m = 76$. Table 5.3 displays the magnitude of the largest perturbation in semimajor axis and the along-track direction $(\omega + M)$ for both $m = 51$ and $m = 76$ along with the period of the perturbation, and was calculated via *Rosborough and Tapley* [1987].

The p and q variables in Table 5.3 are taken from Kaula's standard solution for the gravitational potential in terms of Keplerian orbital elements [*Kaula*, 1966]. The similarity of the perturbation frequencies leads to the filter being unable to separate them, and these bands of coefficients become poorly determined, as is reflected in Figure 5.5. This error then manifests itself in the spatial plot of the recovered signals, leading to a large value of E. Note that similar unexpected

		Period (hours)	Δa (cm)	$\Delta\omega + M$ (deg)
m=51	l=51,53,55,...	7.09	3.87	0.86E-5
	p=24,25,26,...			
	q=0			
m=76	l=77,79,81,...	7.09	0.78	0.67E-6
	p=36,37,38,...			
	q=0			

Table 5.3: Dominant perturbations for m=51 and m=76 for a polar pair of satellites in an 8-day RP at 291 km

correlations exist for orders other than the one shown here for this particular case. The above results demonstrates the importance of performing simulation studies to high degree and order.

5.4.2 Selecting an Inclination

It is expected that the selected value for i_2 will have a large influence on the mission performance. Figure 5.7 shows the formal errors for a 17-day RP polar pair of satellites coupled with a 17-day RP pair of satellites at various inclinations. The logarithm of the formal error of each spherical harmonic coefficient is plotted. Note that the difference in altitude between the satellite pairs at different inclinations will have slight influences on the formal errors. However, if one examines Figure 5.3 which shows the altitude for the various inclinations of a satellite in a 17-day RP, it is seen that the difference in altitude between each of these cases is 15 km at a maximum. Thus, this effect should be minimal on the covariance analysis.

Figure 5.7 shows that for $55^o \leq i_2 \leq 65^o$, higher degree and order tesseral harmonics are perhaps the best determined. Sectorial and near-sectorial coefficients tend to have larger errors as i_2 increases. Studying the covariance matrices alone might lead one to conclude that an inclination of approximately 60^o is near-optimal in the sense that the overall errors of the coefficients is lowest and the covariance matrix is fairly isotropic (no order dependence). However, geographically speaking, if the second pair of satellites flies at an inclination of 60^o, it is seen that it provides no coverage over Greenland, and does not cover a substantial amount of landmass in the northern hemisphere, including Alaska, northern Canada, northern Russia, and the Scandinavian countries. Should the

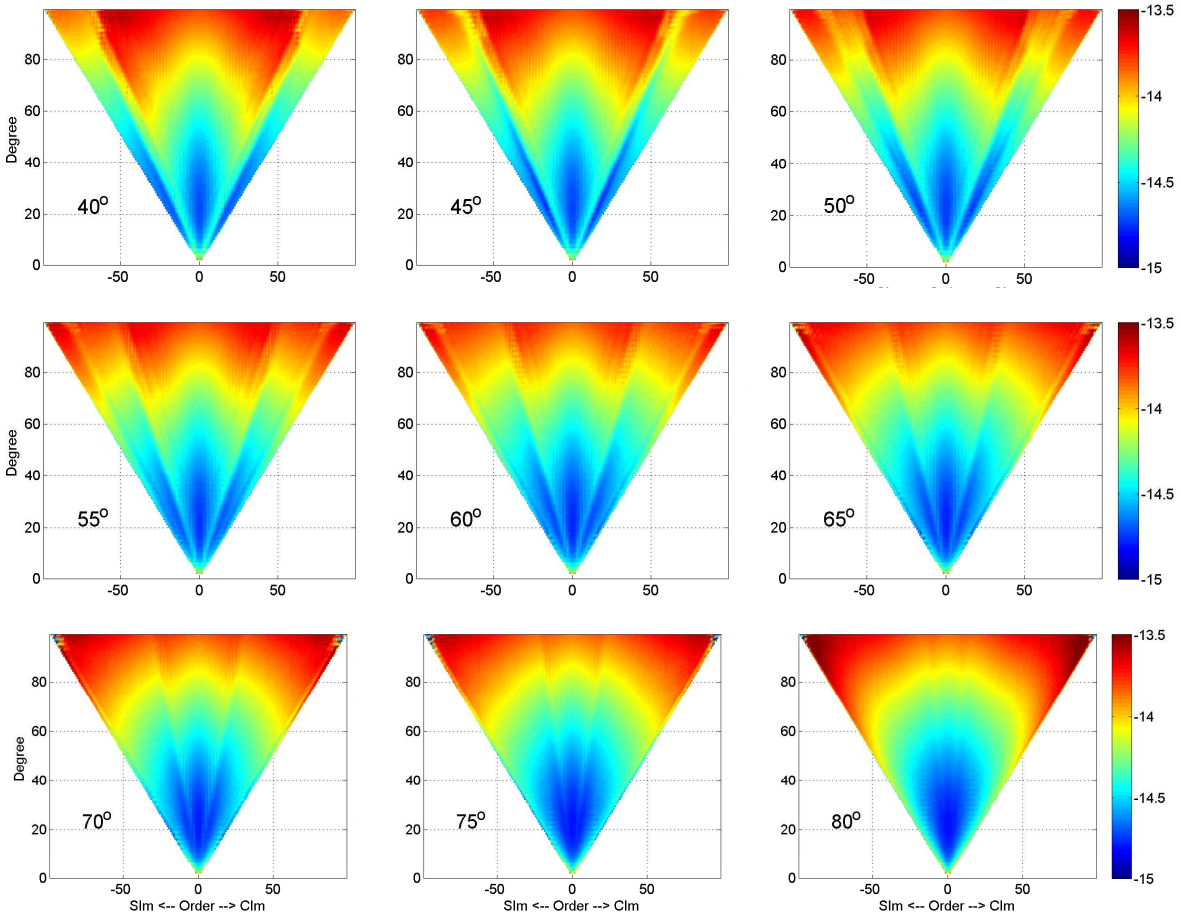

Figure 5.7: Covariance analysis for a 17-day RP polar pair coupled with a 17-day RP pair of satellites at various inclinations. The logarithm of the standard deviation of the coefficients is plotted.

second pair of satellites provide coverage over these regions, it could improve the determination of mass variations in these areas even though this is not reflected in the covariance analysis.

Therefore, it is useful to compare the error metric, E, as discussed in Section 5.3, between different inclinations. Figure 5.8 shows E for a pair of satellites at different inclinations in a 17-day RP coupled with a polar pair of satellites in different repeat periods (15, 16, and 17 days).

Figure 5.8 shows that whether the lower inclined pair of satellites is coupled with a 15, 16, or 17-day RP polar pair of satellites, the general trend in the error as a function of inclination is the same. Typically, the error reaches a minimum between 70^o and 75^o. This is not surprising since a pair of satellites at this inclination gets fairly good coverage over the Earth while still

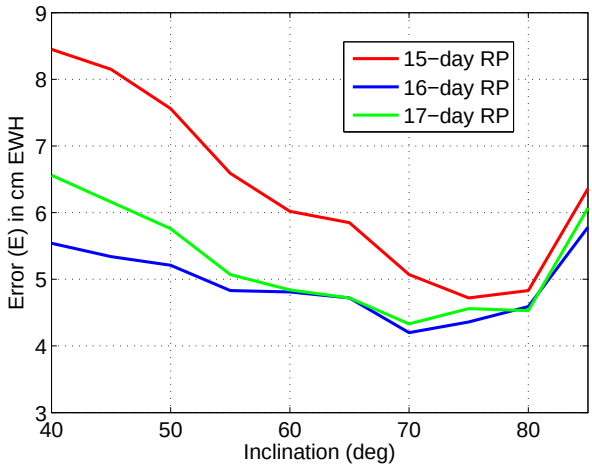

Figure 5.8: Error as a function of inclination for a lower inclined pair in a 17-day RP coupled with a polar pair in 15, 16, and 17-day repeat periods

maintaining a significant East-West component in the observable. The results from two polar pairs of satellites were not placed on this figure as the errors were so high they would distort the scale. This attests to the strength of the East-West information in the observable. While Figure 5.8 shows an extremely small subset of the results that have been analyzed, the general trend of having the best performance for values of i_2 between 70^o and 75^o was consistent across all cases examined.

5.4.3 Coupling of Repeat Periods

Bender et al. [2008] suggested that having a polar orbiting pair in a shorter RP than a lower inclined pair would provide more homogeneity in the groundtrack coverage over the Earth, and thus, result in better solutions. The polar pair of satellites with a shorter RP could reduce the level of temporal aliasing errors in the polar regions as well.

Figure 5.9 illustrates the error as a function of different repeat periods for the polar pair of satellites coupled with a lower inclined pair of satellites $(70^o, 71^o, 75^o, 80^o)$ in a 17-day RP. Note that the range of inclinations examined in this plot is consistent with the range of inclinations that minimized the error as seen in Figure 5.8.

Figure 5.9 shows that generally the error decreases when the lower inclined pair of satellites

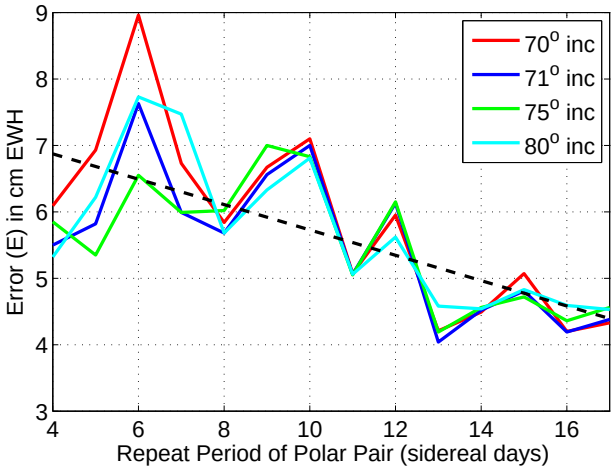

Figure 5.9: Error as a function of the repeat period of a polar pair of satellites being coupled with lower inclined pair in a 17-day RP

is coupled with a polar pair of satellites in longer repeat periods. Note that this trend exists outside of the differences in altitude between the polar pairs of satellites. In fact, plotting the error as a function of altitude of the polar pair rather than the repeat period of the polar pair does not show significant trends. It can then be assumed that the error is a stronger function of the repeat period of the polar pair of satellites than the altitude. Thus, one can assume that coupling two satellite pairs with the same repeat period will provide near-optimal results. One could argue that a global minimum may not be achieved by setting the repeat periods of the two pairs equal to each other, based on the fact that in Figure 5.9 it appears that slightly smaller errors exist when the polar pair is either in a 13-day RP or a 16-day RP versus the 17-day RP that we have recommended. While this is true, the differences in performance between the cases is extremely small. In an effort to reduce the search space for this type of mission we feel that invoking a $k_1 = k_2$ constraint leads to near-optimal results while reducing the amount of computation time necessary to study all possible combinations of k_1 and k_2. Additional simulation results for repeat periods other than 17 days validate this statement.

5.4.4 Selecting a Repeat Period

After selecting a range of near-optimal inclinations for the second pair of satellites as well as enforcing the constraint that $k_1 = k_2 = L$, the search space for an optimal value of L is substantially reduced. Table 5.4 shows the ten cases for which results will be displayed. Each of these cases has a lower inclined pair with an inclination around $70^0 - 75^o$, selected to provide the closest altitude to 290 km. Note that the case number corresponds to the RP of the satellite pairs for convenience. It is evident that there are several repeat periods that are not shown. If a particular repeat period is not shown, for example, 12 days, this is because the altitude of one of the satellite pairs was too high for the results to be competitive with those listed. Generally speaking, due to the constraint that k/l must be irreducible, repeat periods that are prime numbers have a larger range of altitudes to choose from.

Case	**Lower Inclined Pair**			**Polar Pair**		
	Rep. Per. (days)	**Inclination (deg)**	**Altitude (km)**	**Rep. Per. (days)**	**Inclination (deg)**	**Altitude (km)**
9	9	74	291	9	90	318
11	11	70	300	11	90	306
13	13	72	290	13	90	299
14	14	75	290	14	90	316
15	15	70	298	15	90	293
17	17	71	290	17	90	305
19	19	76	291	19	90	300
21	21	71	291	21	90	309
22	22	73	291	22	90	294
23	23	75	291	23	90	292

Table 5.4: Mission architectures examined to optimize the selection of a repeat period

Figure 5.10 shows the error for each of the cases listed in Table 5.4. The blue bars are the solutions obtained using the processing methodology outlined in Section 3.4. Comparing these solutions, it is seen that having a repeat period in the range of 11 to 14 days provides the lowest error, with a global minimum provided by $L = 13$ days. This range of values for L strikes an optimal balance between having enough data to form a good solution, but a short enough time

frame where the accumulation of temporal aliasing errors is mitigated.

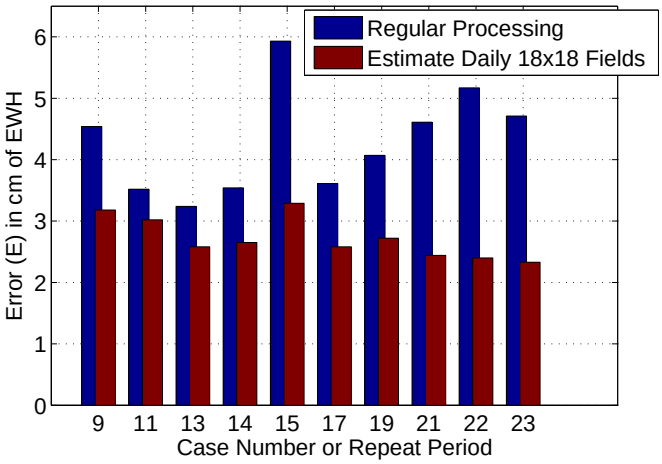

Figure 5.10: Error for the cases listed in Table 5.4 comparing regular processing and estimating daily 18x18 gravity fields

The red bars in Figure 5.10 are obtained by invoking an alternate processing methodology where daily 18x18 gravity fields are estimated in an effort to reduce the level of temporal aliasing errors, described in Chapter 4. It is seen that estimating the daily gravity fields reduces the error substantially for all cases considered. It is also interesting to note that with this processing methodology invoked, the longer repeat periods provide the lowest errors. This makes sense, as for the case with no temporal aliasing errors, the total amount of error should decrease as the square root of the number of observations. However, the reduction in errors that a 23-day RP provides over the 13-day RP case is small when one considers that 10 days of temporal resolution are sacrificed.

5.4.5 Groundtrack Patterns

The three primary variables in Equation 5.11 have been optimized. The last two variables, $\Delta\Omega_{12}$, and Δu_{12} are not expected to have as large of an influence on the solution, as they only change the space-time sampling characteristics of the orbit. One thing that can be examined, however, is if certain groundtrack patterns between the two satellite pairs can be developed which will lower the errors.

In this work, it was noticed that for the case of having two polar pairs of satellites in the same RP and at the same altitude, the best solutions are obtained when $\Delta\Omega_{12}$ is set such that

$$\Delta\Omega_{12} = \delta + \epsilon, \tag{5.15}$$

where

$$\delta = \pi \left(1 + \omega_e \sqrt{\frac{a^3}{\mu}}\right), \tag{5.16}$$

and

$$\epsilon = \frac{2\pi}{l}\left(\frac{1}{2} - \left(\frac{l\delta}{2\pi} - \left\lfloor \frac{l\delta}{2\pi} \right\rfloor\right)\right), \tag{5.17}$$

In Equation 5.15, δ shifts the relative node between the two satellite pairs exactly 180° from each other plus the distance it takes for the Earth to rotate during one-half of a satellite revolution. The ϵ term is added as a correction factor such that the groundtracks of the second pair of satellites will fill in the gaps at the equator from the groundtracks of the first pair of satellites, resulting in more dense coverage. This architecture guarantees that the mutual crossing location of both satellite pairs will be at a constant low latitude ($\sim 7°$), rather than at the equator. This configuration appears to have substantial benefits in the case of two polar pairs of satellites, reducing the errors at the resonant orders considerably. The same magnitude of improvement is not provided when applying it to the case of a polar pair coupled with a lower inclined pair, however. The reason for this is twofold: (1) the periods of the two satellite pairs are different, and (2) the inclinations of the two pairs are different, meaning that the drift rate of the node ($\dot{\Omega}$), given in Equation 5.8 is different between the two cases. These two differences mean that there are no consistent crossings between the two satellite pairs in either space or time. However, there are still minor improvements seen when invoking Equation 5.15 to the cases in Table 5.4. Figure 5.11 shows the reduction in the level of error that this shift provides. Since $\Delta\Omega_{12}$ will not be constant for the duration of the mission due to $\dot{\Omega}$ for the lower inclined pair, the reduction in the level of errors seen in Figure 5.11 represents the natural variability in the quality of the solutions due to the precession of $\Delta\Omega_{12}$.

One can now begin to think of developing a spatial groundtrack pattern for the case of having a polar pair coupled with a lower inclined pair that is consistent, as is the case when there are two

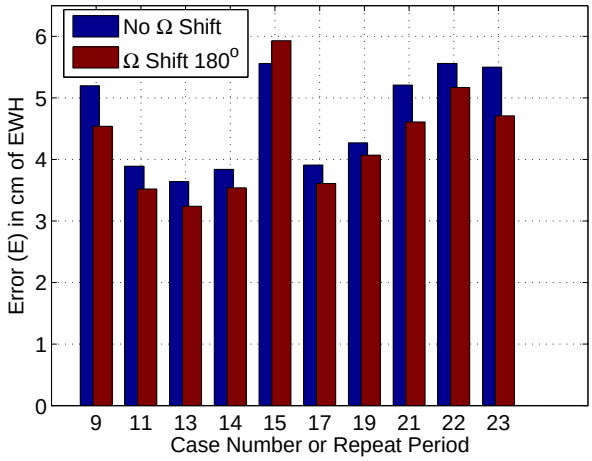

Figure 5.11: Error for the cases listed in Table 5.4 comparing the effect of shifting the longitude of ascending node

polar pairs. Note that we are only interested in developing a spatial pattern ($\Delta\Omega_{12}$), and not a temporal one (Δu_{12}), since the difference in periods between the two satellites pairs causes a secular drift rate in this parameter ($\Delta\dot{u}_{12}$) which cannot be controlled. One can, however, raise the altitude of the polar pair of satellites such that its period increases enough to compensate for the nodal drift rate of the lower inclined pair, thus, ensuring consistent crossings at the equator in the spatial domain by solving the following equation:

$$\dot{\Omega}_{li} T_{li} = \omega_e (T_{pp} - T_{li}) \tag{5.18}$$

with

$$T = \dot{M} + \dot{\omega}. \tag{5.19}$$

In Equations 5.18 and 5.19, *li* stands for "lower inclined" and *pp* stands for "polar pair". The period of the satellites is given by T. The constraint given in Equation 5.18 guarantees that both pairs of satellites complete the same number of orbital revolutions in the same number of nodal days ($l_1 = l_2$), and ensures that the groundtracks of the satellites will cross each other at constant lines of latitude. Unlike the case of two polar pairs, however, the crossings will not have consistency in the time domain due to the discrepancy in periods between the two satellite pairs. Figure 5.12

shows the groundtrack of two pairs of satellites over South America. The groundtrack displayed in blue is from the polar pair of satellites while the groundtrack displayed in red is from the lower inclined pair of satellites. It can be seen how the two pairs always cross at the same latitude.

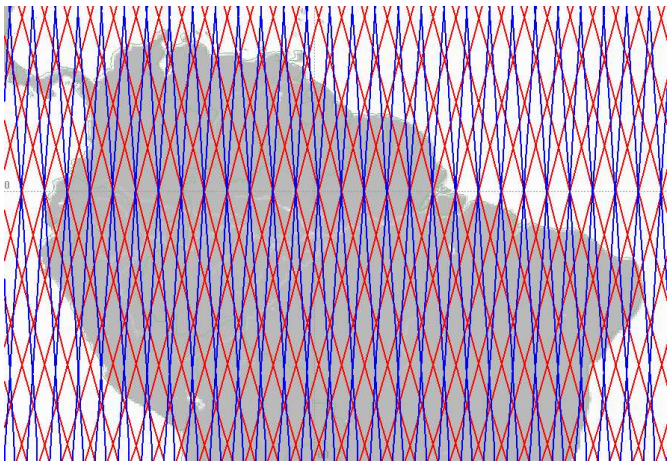

Figure 5.12: Complementary groundtrack pattern shown over South America, arrived at by invoking Equation 5.18

Table 5.5 shows the modified architectures necessary to obtain the complementary groundtrack patterns described above. Note that the altitude of the polar pair for each case, with the exception of Case 9 and Case 14, has been raised by approximately 20-30 km. Cases 9 and 14 are the same between Table 5.4 and Table 5.5 by the fact that the polar pair selected was already at the appropriate altitude necessary for a complementary groundtrack pattern.

Figure 5.13 shows the error comparing the orbits from Table 5.4, with the lowest altitude polar pair possible, with those from Table 5.5, with a complementary groundtrack pattern but a slightly higher altitude for the polar pair of satellites.

Figure 5.13 shows a minor degradation in performance for five of the cases considered and a minor improvement in performance for three of the cases considered. Cases 9 and 14 have the same performance since they involve the same orbits. It is difficult to draw conclusions from these results. Possible benefits from flying the satellites with a complementary groundtrack pattern include the fact that the polar pair of satellites is at a higher altitude which means increased longevity due to lower atmospheric drag forces. Also, the crossings at lines of constant latitude could prove beneficial

Case	Lower Inclined Pair			Polar Pair		
	Rep. Per. (days)	Inclination (deg)	Altitude (km)	Rep. Per. (days)	Inclination (deg)	Altitude (km)
9	9	74	291	9	90	318
11	11	70	300	11	90	332
13	13	72	290	13	90	320
14	14	75	290	14	90	316
15	15	70	298	15	90	331
17	17	71	290	17	90	322
19	19	76	291	19	90	315
21	21	71	291	21	90	322
22	22	73	291	22	90	319
23	23	75	291	23	90	317

Table 5.5: Mission architectures examined with complementary groundtrack patterns

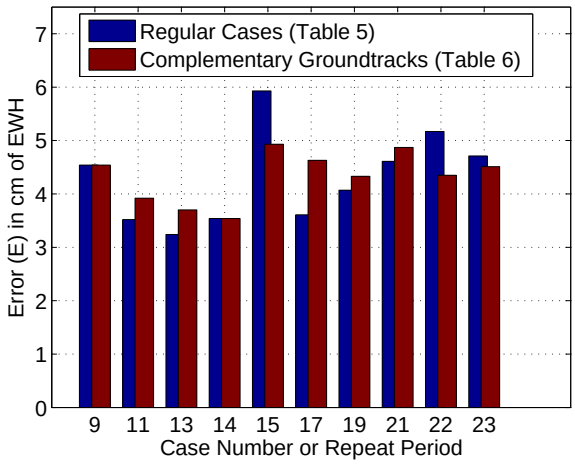

Figure 5.13: A comparison of the error between the orbits in Table 5.4 with those in Table 5.5, which have slightly higher altitudes for the polar pair of satellites but have complementary groundtrack patterns

in future applications that are not yet realized; i.e. using the crossing points as constraint points for determining the geopotential at particular locations. For a gravity mapping mission, analagous to an altimeter mapping mission such as TOPEX or Envisat, there is an argument for having a geometry between the two satellite pairs in terms of the groundtracks that permits a consistent synoptic mapping of the time-variable gravity variations.

5.4.6 Expected Performance

A detailed analysis on regional scales for the expected improvements that an optimized two-pair architecture provides over a single pair architecture is given in Chapter 6. However, a global comparison is shown in this section using the error metrics applied in this chapter. For this comparison, we select Case 13 in Table 5.5 consisting of a polar pair of satellites coupled with a lower inclined pair of satellites at 72^o, both in 13-day RP orbits and possessing a complementary groundtrack pattern as discussed in Section 5.4.5. Furthermore, we estimate daily 18x18 gravity fields for this case to further reduce temporal aliasing errors as discussed in Chapter 4, which is an additional advantage of having a polar pair coupled with a lower inclined pair. Figure 5.14 shows the truth signals (left), recovered signals (middle), and error (right) for recovering hydrology and ice mass variations (top) and ocean bottom pressure signals (bottom). The plots are represented out to degree 60 and are expressed in cm of EWH. Table 5.6 illustrates the signal and error associated with Figure 5.14 in cm of EWH.

	Signal (cm)	**Error (cm)**
Hydrology	$S(H) = 4.67$	$E(H) = 1.91$
Ice	$S(I) = 2.12$	$E(I) = 3.31$
Ocean	$S(O) = 2.46$	$E(O) = 2.41$
Total	$S = 3.08$	$E = 2.54$

Table 5.6: Signal and error associated with Figure 5.14. Units are expressed in cm of EWH.

Comparing the results from Figure 5.14 and Table 5.6 with those in Section 5.3 containing the results of a single polar pair of satellites in a 13-day RP groundtrack illustrates the advantage that strategically placing an extra pair of satellites provides. The global error, E is decreased by approximately 75% with the addition of the second pair of satellites, with the largest improvement coming in determining hydrology. As expected, the addition of the lower inclined pair substantially reduces the level of striping in the solutions. There are certain bands of coefficients which remain correlated, however. The large errors in the high latitude regions seen in Figure 5.14 are a direct consequence of correlations in coefficients of a fixed order and same parity of degree in the range

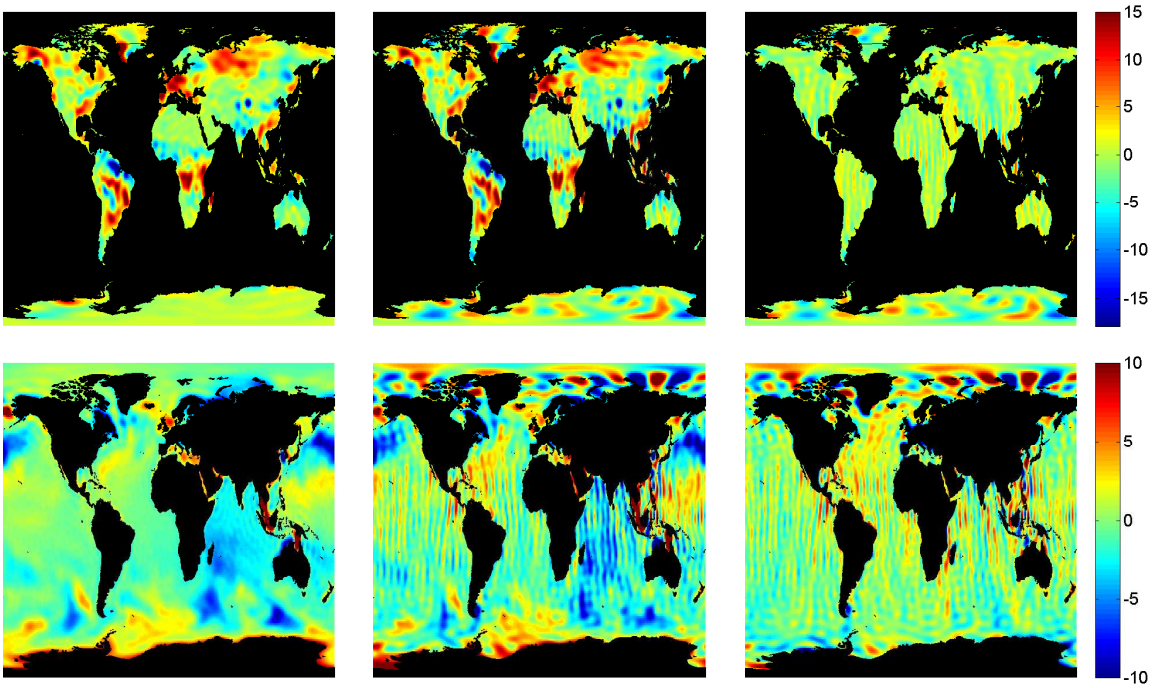

Figure 5.14: Truth signals (left), recovered signals (middle), and the error (right) for recovering hydrology and ice mass variations (top row of plots) and ocean bottom pressure signals (bottom row of plots) for Case 13 in Table 5.5 while estimating daily 18x18 gravity fields. Units are in cm of equivalent water height.

$n \geq 40$ and $3 \leq m \leq 14$. Note that these errors occur predominantly in geographical areas with latitudes higher than 72^o, as no East-West information is present here. It is expected that given a mission architecture of this type in the future, tailored filters will be developed to remove such correlated errors, similar to that developed by *Swenson and Wahr* [2006]. One such option is presented in Section 6.4. For the analysis presented here, however, it is seen that the solutions given in Figure 5.14 without any post-processing techniques applied still retain significant geophysical signals at small spatial scales.

5.5 Conclusions

The goal of this chapter was to optimize the orbits of two satellites pairs to provide increased spatial resolution in determining hydrology, ice mass variations, and ocean bottom pressure signals globally. While the search space for such a problem is, by nature, infinite, a Monte-Carlo analysis

using numerical simulations to degree and order 100 is implemented in an effort to reduce it. A search space originally consisting of fifteen variables is reduced to two variables with primary impact on mission performance: the inclination of one of the satellite pairs (the other pair is assumed to be polar), and the repeat periods of both pairs of satellites (shown to be near-optimal when they are equal to each other). In this study we consider only circular orbits in repeating groundtracks, a minimum allowable altitude of 290 km based on a projected 10-year mission lifetime, and assume a 100 km inter-satellite separation distance between each pair of satellites. It is found that an optimal value for the inclination of the second pair of satellites is between 70^o and 75^o, while an appropriate range for the repeat periods of both satellite pairs is between 11 and 14 days. The absolute lowest errors are given when both satellite pairs are in a 13-day repeat period, one being polar at an altitude of 299 km, and the other inclined at 72^o at an altitude of 290 km. It should be noted that the results of this study are influenced by the targeted altitude for the mission as well as the scientific goals of the mission.

The notion of optimizing the relative change in node and the argument of latitude between the two pairs is discussed in relation to creating complementary groundtrack patterns. It is shown that by raising the altitude of the polar pair, the nodal drift rate of the lower inclined pair can be compensated for such that a groundtrack pattern with crossings at constant lines of latitude is created. While numerical simulation results imposing this constraint are not conclusive as to whether this definitively results in improved mission performance, there is an argument for having a geometry that permits consistent global mapping of the gravity field. Finally, the importance of extending simulations to high degree and order is shown.

Results show that with an optimized architecture consisting of two satellite pairs, the time-variable gravity solutions do not need to be destriped or smoothed, resulting in a 75% reduction in the level of errors over what one pair of satellites provides, and a gravity field product with much higher spatial resolution. Chapter 6 provides an in-depth examination of the expected scientific benefits of an optimized two-pair architecture, extending the analysis to local regions as well as longer time spans.

Chapter 6

Expected Improvements in Determining Temporal Gravity Variations using Two Satellite Pairs

6.1 Introduction

This chapter aims to quantify the expected improvements in determining hydrology, ice mass variations, ocean bottom pressure signals, and earthquakes that having two pairs of dedicated satellites provides over only a single pair. We compare three cases: a single pair of polar satellites, two pairs of polar satellites, and a polar pair of satellites coupled with a lower inclined pair of satellites. Based on the discussion and results in Chapter 5, we select a near-optimal architecture for the case of two polar pairs as well as a polar pair coupled with a lower inclined pair.

6.2 Orbit Selection and Methodology

For the case of a polar pair coupled with a lower inclined pair of satellites, we select a near-optimal architecture consisting of a polar pair of satellites at 320 km coupled with a lower inclined pair of satellites at 72° at 290 km, both pairs being in 13-day repeating groundtracks (Case 13 in Table 5.5). This architecture ensures a groundtrack pattern where the two pairs of satellites cross each other at constant lines of latitude. While perhaps not yet fully exploited, a groundtrack pattern of this type is expected to be beneficial for future missions, allowing for consistent synoptic mapping of time variable gravity variations. For the case of two polar pairs of satellites, we use the same polar pair of satellites in the previously described architecture at 320 km altitude, and add another pair of polar satellites offset in the node according to Equation 5.15. This permits

consistent groundtrack crossings between the two pairs in time and space, and was found to be optimal for the case of two polar pairs. The architecture involving one pair of satellites chosen for comparison consists of the same polar pair of satellites common between the two architectures described above: a pair at 320 km in a 13-day repeating orbit. Figure 6.1 shows the groundtracks of all three cases, with the one-pair architecture (left), two polar pairs (middle), and a polar pair coupled with a lower inclined pair (right). The top set of plots shows the groundtracks over the entire globe, while the bottom set of plots shows the groundtracks over the Amazon so that one can understand the nature of the crossings between the two pairs. Note that for the case involving the lower inclined pair, this pair geographically extends to cover the southern half of Greenland as well as the western Antarctic peninsula. All analyses and comparisons made in this chapter involve these selected architectures.

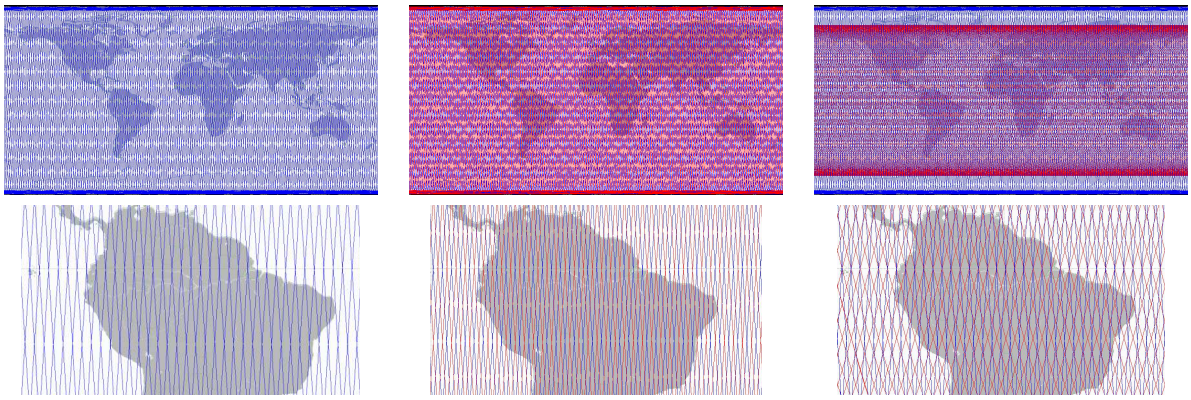

Figure 6.1: Groundtrack over 13 days for the case of one pair of satellites (left), two polar pairs (middle) and a lower inclined pair coupled with a polar pair (right). Groundtracks are shown for the entire globe (top) and over the Amazon (bottom).

The numerical simulations performed in Chapter 5 have been extended for one full year to quantify temporal gravity variations. Additionally, in this analysis, daily low degree and order gravity fields are estimated simultaneously in an effort to reduce temporal aliasing errors, as described in Chapter 4. For both cases involving two satellite pairs, we estimate 18x18 gravity fields every day, as this has been shown to be near-optimal and effective. For the case of a single pair of satellites, high frequency/low resolution gravity fields are not estimated. We do not estimate them

for this case due to the variability in the quality of the groundtracks over two-day periods (it was shown in Chapter 4 that two-day estimates are necessary to gain an accurate low degree gravity field estimate for the case of a single pair of satellites). Additionally, the solutions from one pair of satellites necessitate the standard post-processing procedures associated with GRACE (removal of correlated errors and smoothing of the solutions) regardless of whether two-day gravity fields are estimated or not; thus, negating any reduction in errors that performing the two-day estimates provides.

6.3 Covariance Analysis

Figure 6.2 shows the logarithm of the formal errors (top row) along with the actual errors (bottom row) for a simulation designed to recover hydrology and ice mass variations, as illustrated in Table 3.1. The plots on the left are for one pair of satellites, the middle plots show the results for two polar pairs, and the results on the right are for a polar pair coupled with a lower inclined pair. The covariance analysis indicates that a polar pair coupled with a lower inclined pair is expected to have substantially lower errors for the entire spectral domain of spherical harmonic coefficients, with particular improvements in determining the sectorials and near-sectorials. Two polar pairs of satellites shows a slight reduction in the formal errors over what one pair of satellites provides, albeit retaining the same error pattern. For the case of a single pair of satellites and two polar pairs of satellites, the actual errors show that higher degree and order tesseral harmonics are poorly determined, as is expected via the covariance analysis. Additionally, it is seen that the actual errors manifest themselves at the resonant order and multiples of the resonant order ($m = 16, 32, 48, ...$) (this is more dominant in the case of one pair of satellites than the case of two polar pairs). These can be reduced via estimating empirical accelerations with a frequency of once per revolution, twice per revolution, and so on. Many of the GRACE processing centers employ this step during their estimation schemes. While we have found that this step does reduce the errors at the resonant order and multiples of the resonant order, the resulting gravity field estimates still have longitudinal stripes, requiring standard post-processing procedures. Once these post-processing procedures have

been invoked, there are negligible differences in the resulting gravity field estimates whether we estimate empirical once per revolution and twice per revolution acceleration terms or not; hence, we forgo this step. With the addition of the lower inclined pair of satellites, the bands of error at the resonant order and multiples of the resonant order diminsh substantially. The highest errors are seen at the high degree and order tesseral harmonic coefficients, beginning at approximately degree 60. The larger errors for high degree and low order coefficients are a localized effect over the polar regions at latitudes greater than 72° where only North-South information is present in the observable.

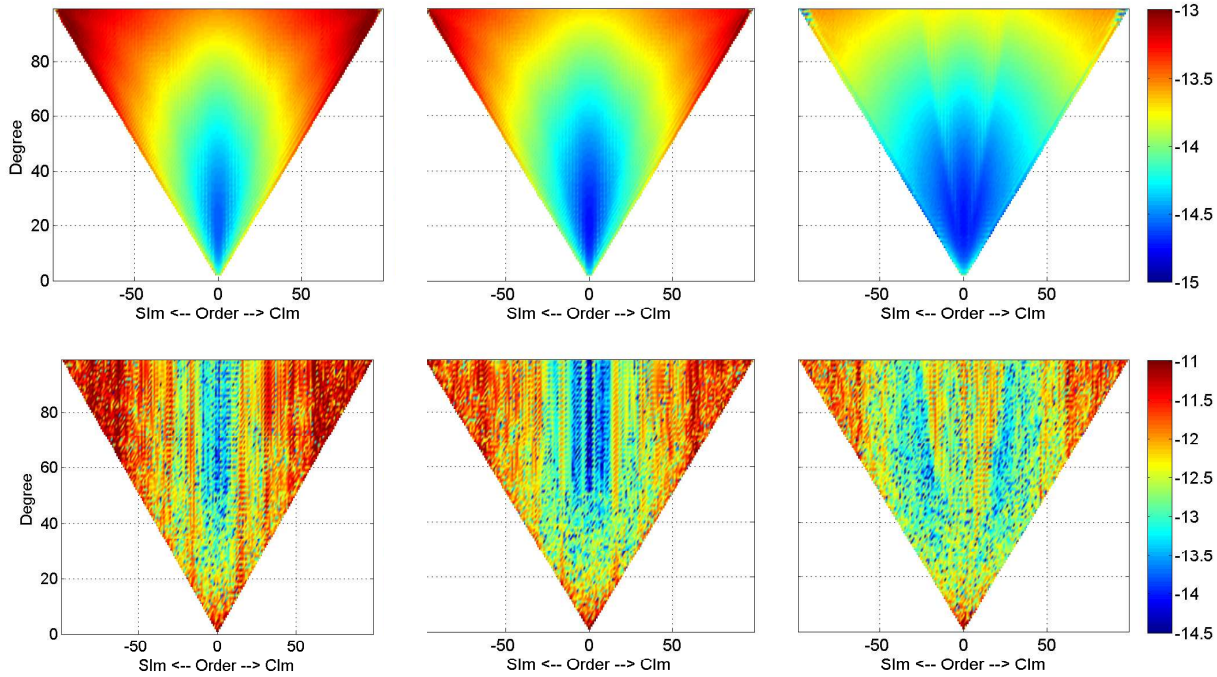

Figure 6.2: Logarithm of the formal error of the spherical harmonic coefficients (top row) for one pair of satellites (left), two polar pairs of satellites (middle) and a polar pair coupled with a lower inclined pair of satellites (right), along with the logarithm of the actual error in the spherical harmonic coefficients (bottom row)

It is also instructive to examine correlations between spherical harmonic coefficients. One cause of the longitudinal striping in the GRACE solutions is that coefficients of a fixed order and the same parity of degree are highly correlated due to the North-South alongtrack observable. Figure 6.3 shows the correlations for a resonant coefficient C(18,16) (top row), a tesseral coefficient

C(24,20) (middle row), and a sectorial coefficient C(30,30) (bottom row) for both the one-pair architecture (left column), two polar pairs (middle column), and a polar pair coupled with a lower inclined pair (right column). Plotted is the correlation of that particular coefficient with the other spherical harmonic coefficients, up to degree 60.

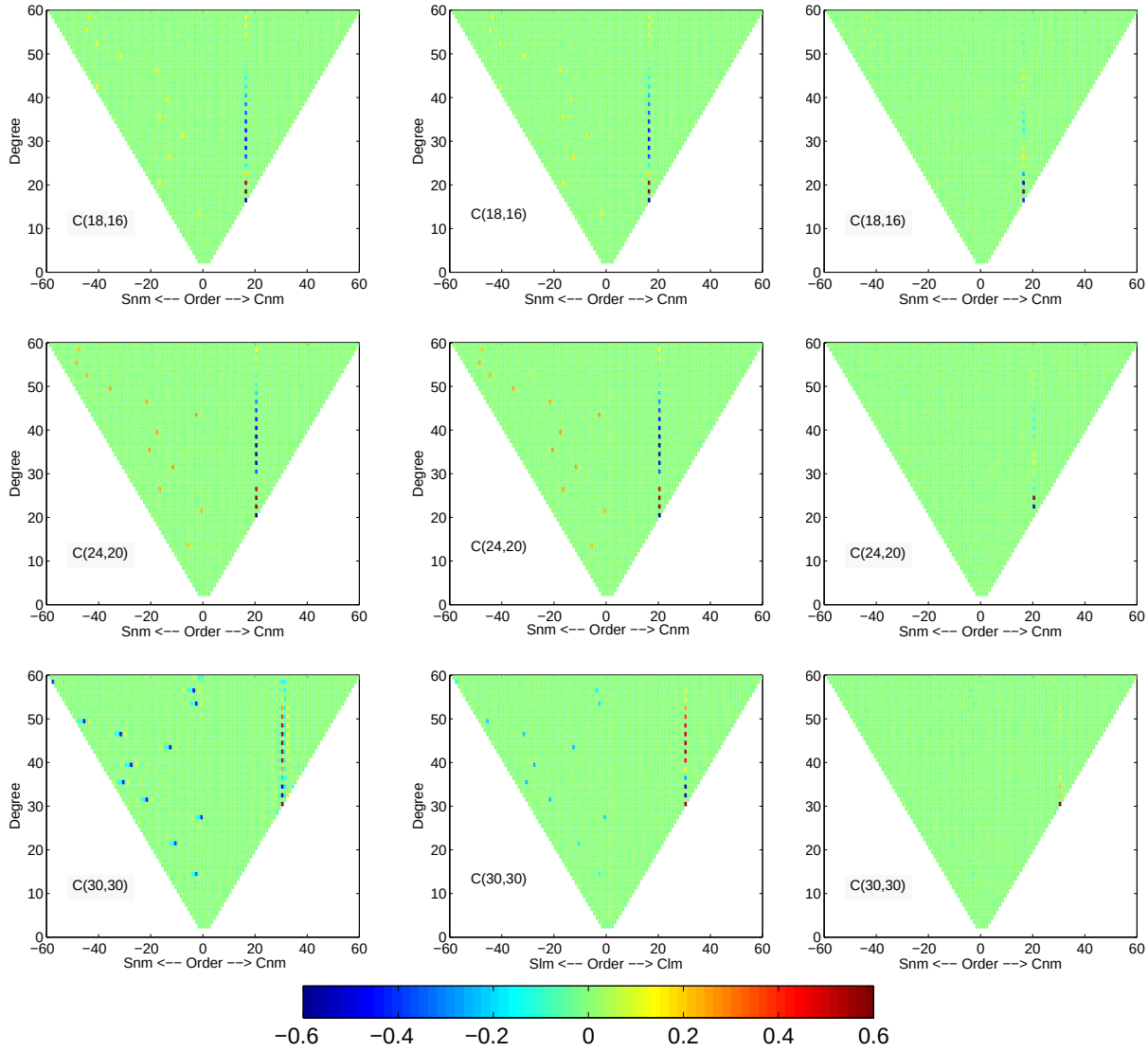

Figure 6.3: Correlation coefficients of selected spherical harmonic coefficients with others. The left column is the correlation coefficients for one satellite pair, the middle column is for two polar pairs, and the right column contains the correlation coefficients for a polar pair coupled with a lower inclined pair. Shown are the C(18,16) coefficient (top row), C(24,20) coefficient (middle row), and the C(30,30) coefficient (bottom row).

Figure 6.3 shows for the case of one satellite pair (left column), the correlations between coefficients of the same order and same parity of degree are easily recognizable. Additionally, there are other random correlations between coefficients that might otherwise not be expected. With the addition of the second polar pair of satellites, these same correlations persist, indicating that longitudinal striping will still be present in the gravity solutions. With the addition of the lower inclined pair of satellites, the correlations decrease substantially. There still exist correlations with coefficients of the same order and same parity of degree; however, these correlations are lower than the case of one satellite pair and less coefficients are correlated. The decrease in correlations allows the filter to better separate between coefficients and obtain a better estimate of the gravity field. This is reflected in the plot of errors shown in Figure 6.2.

6.4 Post-Processing Techniques Applied

As discussed in Section 1.4, solutions obtained using a single polar pair of satellites have correlated errors, as well as errors at high degrees, which tend to dominate the gravity solutions. These errors are readily seen in Figures 6.2 and 6.3. Typical users of the GRACE data handle these errors by applying post-processing techniques. For our analysis, given the case of one pair of satellites, we remove correlated errors via *Swenson and Wahr* [2006] (known as destriping), and smooth the solutions via Gaussian smoothing [*Jekeli*, 1981; *Wahr et al.*, 1998] with a 300 km averaging radius. This was found to be adequate to accurately resolve mass variations for the one-pair solutions. The destriped and smoothed solutions will be denoted as 'DS' throughout this chapter. Additionally, it will be shown in the next section that two polar pairs of satellites necessitates the same post-processing techniques used for one pair of satellites.

The solutions obtained from a polar pair of satellites coupled with a lower inclined pair of satellites have a completely different error spectrum than that of one pair, as shown in Figures 6.2 and 6.3. As such, an entirely different suite of post-processing tools could be developed for analyzing solutions of this type. As was shown in Figure 5.14, the recovered hydrology, ice, and ocean bottom pressure signals plotted to degree 60 tend to have errors in high latitude regions,

above the latitude which is covered by the lower inclined pair. This is a direct consequence of only having North-South information in these areas. Examining the errors in Figure 6.2 up to degree 60, it is seen that there are larger errors for coefficients with low order ($m \leq 16$) and high degree ($n \geq 40$). We can examine the spatial representations of this band of coefficients to see where they manifest spatially. Figure 6.4 shows the spatial representation of nine coefficients in this range. It is seen that these coefficients describe signal that is predominantly in the geographic areas that have the largest errors due to a lack of East-West information, showing consistency between Figures 5.14 and 6.2.

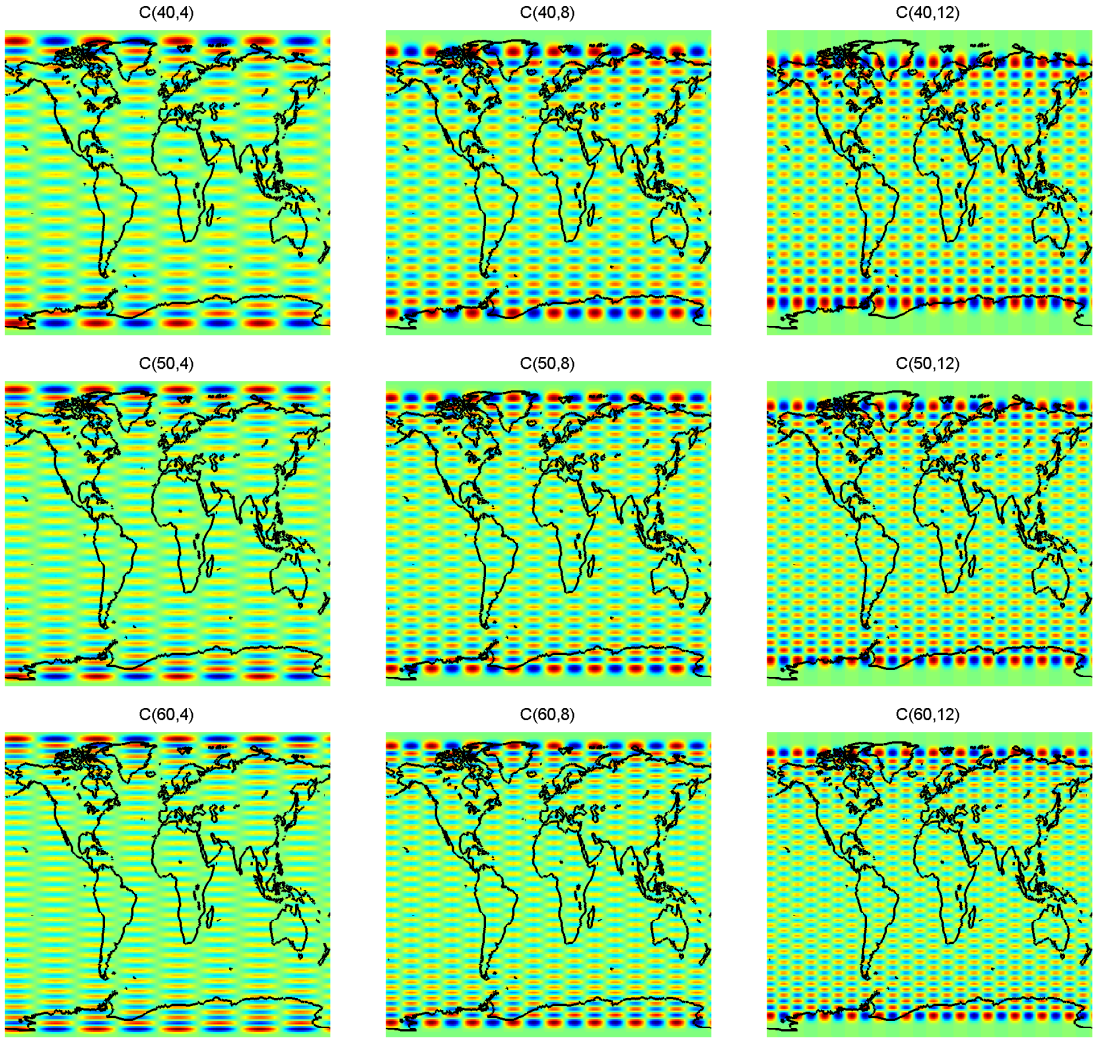

Figure 6.4: Spatial representation of select spherical harmonic coefficients in the range $m \leq 16$, $n \geq 40$.

It is also beneficial to examine the actual values of the recovered spherical harmonic coefficients from the simulation used to produce Figure 5.14 involving a polar pair coupled with a lower inclined pair. Figure 6.5 plots the value of the coefficients for orders 9 and 11 and degrees greater than 40. Shown are the recovered coefficients from the simulation, the recovered coefficients after they have been destriped via *Swenson and Wahr* [2006], and the *truth* coefficients (described by GLDAS + ESA).

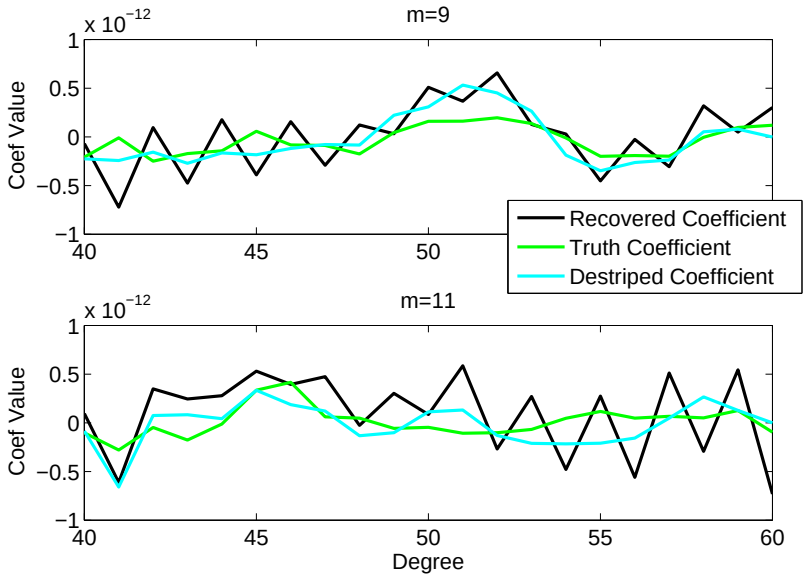

Figure 6.5: Values of spherical harmonic coefficients for order 9 (top) and order 11 (bottom) over degrees greater than 40. Shown are the value of the recovered coefficients from a simulation designed to recover hydrology and ice mass variations using a polar pair of satellites coupled with a lower inclined pair of satellites, along with the *truth* value of the coefficient defined by the hydrology and ice models, and the value of the recovered coefficient after it has been destriped via *Swenson and Wahr* [2006].

The 'sawtooth' behavior of the recovered coefficients is evident in Figure 6.5. This mimics the behavior of the recovered coefficients for one pair of satellites, as was shown in *Swenson and Wahr* [2006], revealing unrealistic correlations of coefficients of a fixed order and the same parity of degree. As we know, this error manifests itself as longitudinal stripes in the gravity solutions. It is seen that after we apply the destriping algorithm, these correlations are removed, and the new coefficients match much more closely to the *truth*. It should be emphasized that these correlations

only exist for the range of coefficients defined by $m \leq 16$, $n \geq 40$. This data indicates that we may be able to destripe coefficients only in this limited range to remove correlated errors and gain better estimates of mass variations in latitudes greater than 72°.

We find that applying the destriping algorithm described in *Swenson and Wahr* [2006] to the range of coefficients described by $3 \leq m \leq 14$, $n \geq 40$ provides optimal results. Note that the gravity solutions are still truncated at degree 60, as we wish not to deal with the errors in higher degree and order tesseral coefficients, as seen in Figure 6.2. For fair comparison, the solutions obtained from one pair of satellites are also truncated at degree 60. The effectiveness of this modified filter to remove correlated errors from the solution involving a polar pair and a lower inclined pair of satellites is shown in Figure 6.6. This figure is a continuation of the results shown in Figure 5.14 for recovering OBP. The recovered OBP signal is shown on the left, along with the recovered signal after correlated errors have been removed via the modified destriping algorithm (middle). The plot on the right shows the signal that was removed via the destriping of the limited range of spherical harmonic coefficients. In essence, it is the difference between the plot on the left and the middle plot.

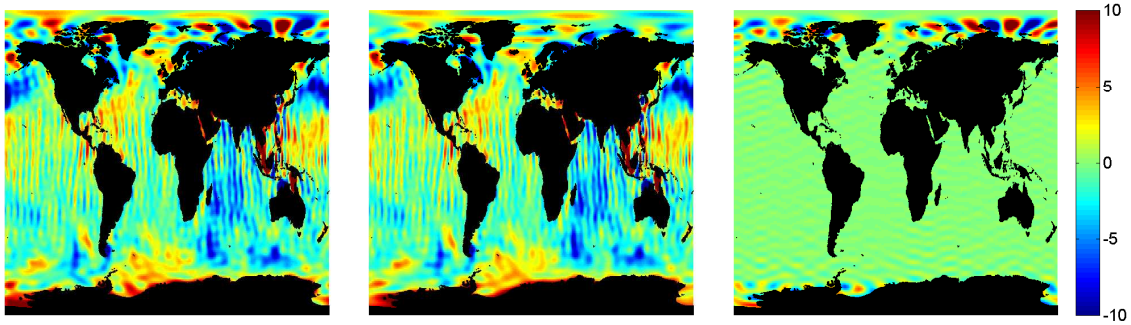

Figure 6.6: Recovered OBP variations from Figure 5.14 with no post-processing (left), after applying the modified destriping algorithm (middle), and the difference between the left and middle plots showing what signals were removed by applying the modified destriping algorithm (right). Plots are averaged over 13 days and expressed in cm of EWH.

Figure 6.6 shows that this modified destriping algorithm specifically targets the errors at high latitudes and removes them. The signals at lower latitudes (i.e. continental hydrology) are

relatively untouched by this algorithm. As such, it is recommended that this algorithm be applied if the user were examining ice mass variations in Antarctica, the northern half of Greenland, Arctic sea ice, or OBP variations at high latitudes.

To conclude this section of text, the following post-processing procedures are applied to the data throughout the remainder of the dissertation. Solutions obtained using one pair of satellites are destriped via *Swenson and Wahr* [2006] and smoothed with a 300 km Gaussian averaging radius. The same post-processing is applied to the solutions obtained from two pairs of polar satellites. For the case of a polar pair of satellites coupled with a lower inclined pair of satellites, no post-processing is applied. If the modified destriping algorithm is applied, then it will be stated as such. Solutions from all architectures are truncated at degree and order 60. Any deviations from these standard post-processing procedures will be stated.

6.5 Results: A Global Perspective

6.5.1 Hydrology and Ice Mass Variations

The expected spatial resolution that all three cases offer in recovering hydrology and ice mass variations is illustrated in both the spatial domain (Figure 6.7) as well as the spectral domain (Figure 6.8). Figure 6.7 shows the truth hydrology and ice signals (top), along with the recovered signals with no post-processing (middle row) for one pair of satellites (left), two polar pairs of satellites (middle), and a polar pair coupled with a lower inclined pair of satellites (right). The bottom row shows the recovered signals after the solutions have been post-processed via the methods discussed in Section 6.4. The solutions are averaged over a single 13-day timespan, have been truncated at degree 60, and are expressed in cm of EWH.

Figure 6.7 illustrates that both the cases of one pair and two polar pairs necessitate the destriping and smoothing processes. While the overall level of error is lower for the case of two polar pairs, the fact that the error pattern is the same as the case of one pair indicates the best way to remove the longitudinal stripes is to destripe via known techniques. Once the solution

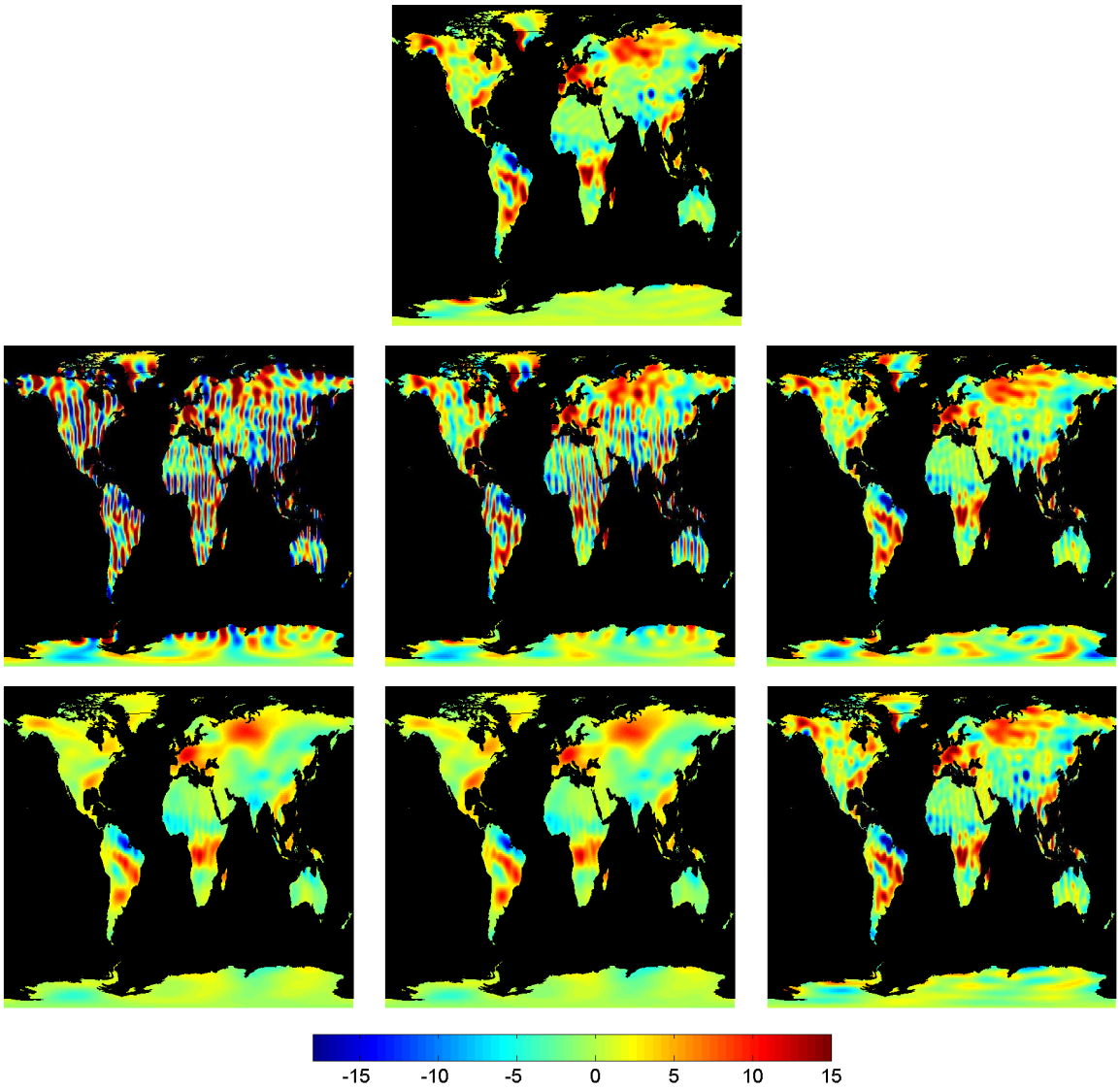

Figure 6.7: The top plot shows the truth hydrology and ice signals averaged over 13 days. The middle row shows the recovered signals for: one pair of satellites (left), two polar pairs (middle), and a polar pair coupled with a lower inclined pair (right). The bottom row shows the same recovered signals, only after post-processing has been applied. The one pair and two polar pair architectures have been destriped and smoothed with a 300 km averaging radius, while the architecture consisting of a lower inclined pair and a polar pair has been destriped via the modified algorithm. Units are in cm of EWH.

is destriped and smoothed (as is also necessary), the recovered mass variations are identical to those recovered using one pair of satellites, and are damped and smoothed with respect to the truth signals. This indicates a very important result in that while the temporal resolution will be

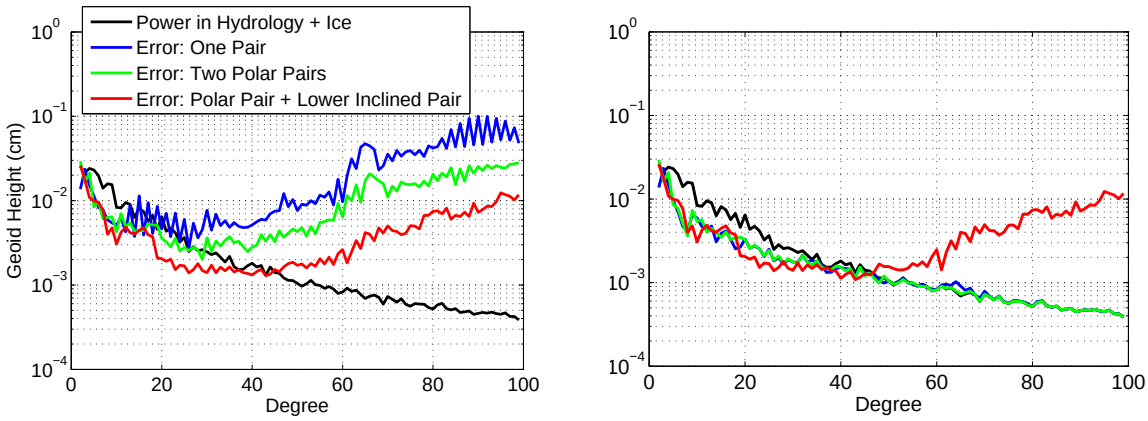

Figure 6.8: Geoid degree error for recovering hydrology and ice mass variations in Figure 6.7 with no post-processing (left) and with post-processing (right).

increased by a factor of two, one cannot expect much improvement in spatial resolution simply by adding another polar pair of satellites due to the presence of longitudinal stripes. Other methods to remove these correlated errors may disprove this statement; however, it was not within the scope of the project to test all available methods to remove correlated errors. The solution obtained using a polar pair of satellites coupled with a lower inclined pair of satellites closely resembles that of the truth signal, particularly at latitudes below 72^o. There are spurious errors in the northern half of Greenland as well as Antarctica which are shown to be removed once the modified destriping algorithm is implemented.

Figure 6.8 shows the error in terms of geoid height in determining hydrology and ice mass variations over a particular 13-day timespan as a function of spherical harmonic degree for all three cases. The plot on the left is when no post-processing is applied, and the plot on the right is after the solutions have been post-processed as described to obtain the results in Figure 6.7. Generally, the expected spatial resolution is approximated by $\sim 40,000/2n$ km. It is seen that with one pair of satellites, the errors become larger than the signal that is being estimated somewhere between degree 15 and 25 (corresponding to basin sizes of 800 and 1300 km), two polar pairs of satellites increases the spatial resolution to 670 km (corresponding to degree 30), while the addition of the lower inclined pair of satellites increases the spatial resolution to approximately

450 km (corresponding to degree 45). After the solutions from one pair of satellites and two polar pairs of satellites are destriped and smoothed, the spatial resolution increases to be approximately commensurate with that of the case involving the lower inclined pair of satellites. One cannot, however, take the results in Figure 6.8, and assume that one pair of satellites provides the same spatial resolution that a polar pair coupled with a lower inclined pair provides. A global analysis of this kind is insufficient, as it disregards the different spatial distributions of signals and errors, as pointed out by *Han and Ditmar* [2008]. As such, regional analyses are necessary to more accurately quantify the expected improvements that the addition of a second pair of satellites provides.

6.5.1.1 EOF Analysis

We use Empirical Orthogonal Functions (EOFs), as discussed in section 2.3.1.3 to analyze the time series of recovered hydrology and ice signals globally. This technique has been successfully applied to GRACE data for many applications, for example *Wouters and Schrama* [2007]. Figure 6.9 shows the first (left column) and second (right column) modes for hydrology and ice signals, which together account for 82% of the variance (the first mode accounts for 69% and the second mode accounts for 13%). Similarly, Figures 6.10 and 6.11 show the third and fourth, and fifth and sixth modes, respectively. The first six modes together account for 98% of the variance. The EOFs were constructed using 27 13-day solutions spanning the year. The time series are shown on the top row followed by the spatial respresentations of the truth signal (second row), recovered signals using a polar pair coupled with a lower inclined pair (third row), and recovered signals using one satellite pair (bottom row). Recovered signals from two polar pairs are not shown, as the results are identical to those from one pair of satellites after post-processing has been applied. The one-pair solutions have been destriped and smoothed with a 300 km averaging radius. The two-pair solutions have been destriped via the modified destriping algorithm (referred to as D*). Including this step in the analysis generally improves the EOF results, due to the global nature of this technique.

The EOF analyses shown in Figures 6.9, 6.10, and 6.11 reveal that the first five modes are

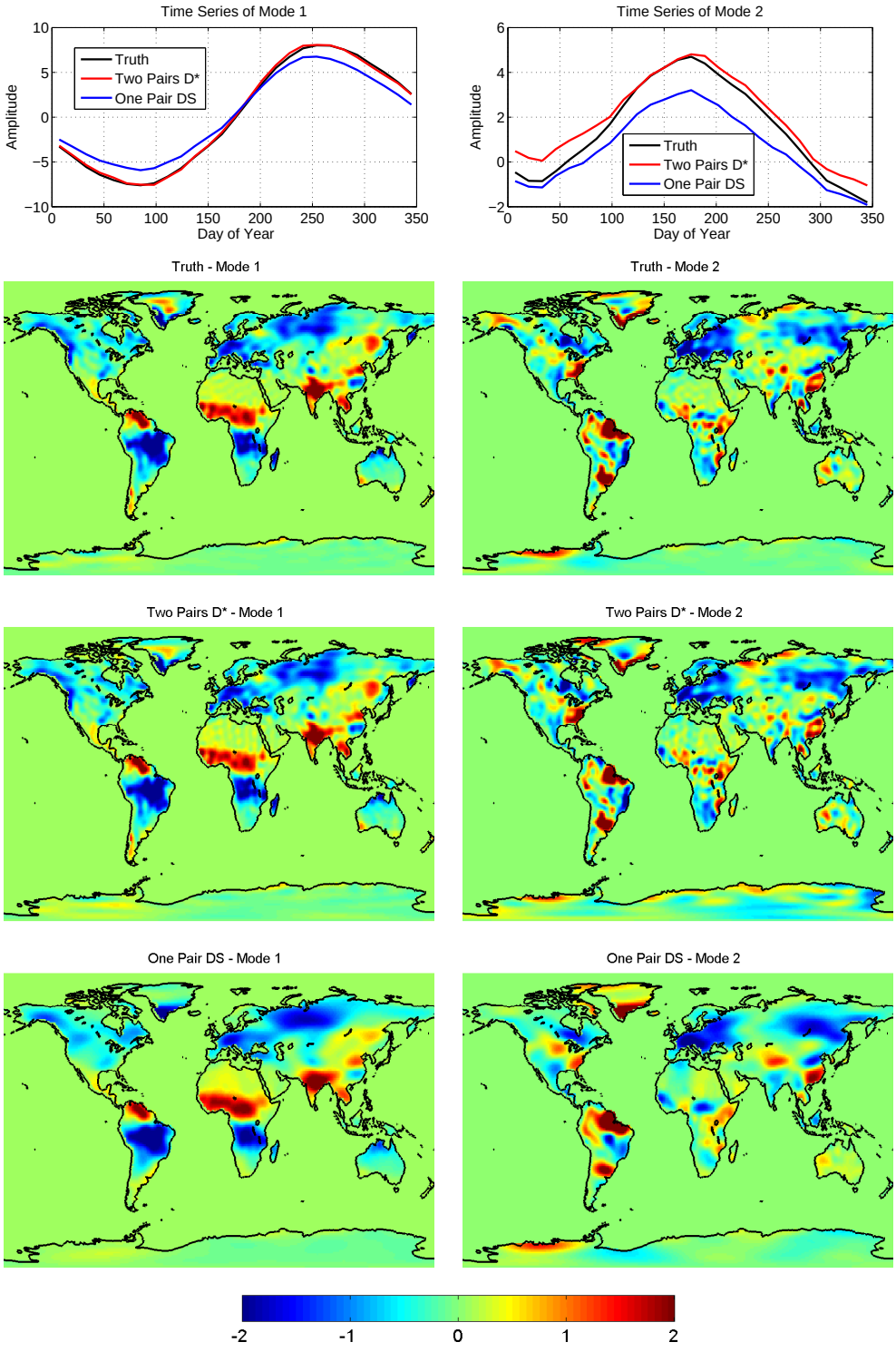

Figure 6.9: EOF analysis for recovering hydrology and ice signals. Shown are mode 1 (left column) and mode 2 (right column) with the time series (top row), truth signal(second row), recovered signal using two pairs with modified destriping (third row), and recovered signal using one pair with destriping and 300 km smoothing (bottom row). Units are in cm of EWH.

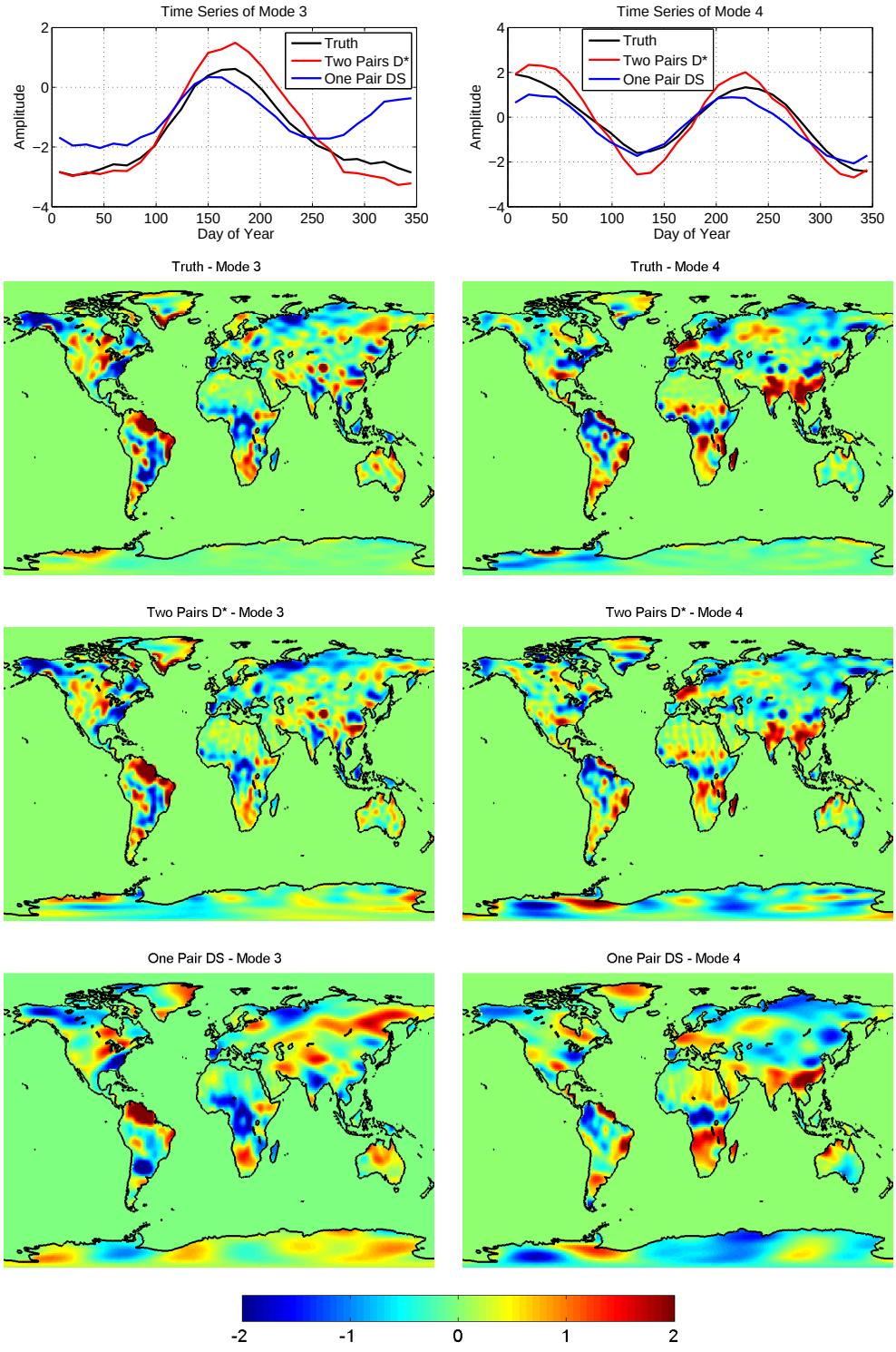

Figure 6.10: EOF analysis for recovering hydrology and ice signals. Shown are mode 3 (left column) and mode 4 (right column) with the time series (top row), truth signal(second row), recovered signal using two pairs with modified destriping (third row), and recovered signal using one pair with destriping and 300 km smoothing (bottom row). Units are in cm of EWH.

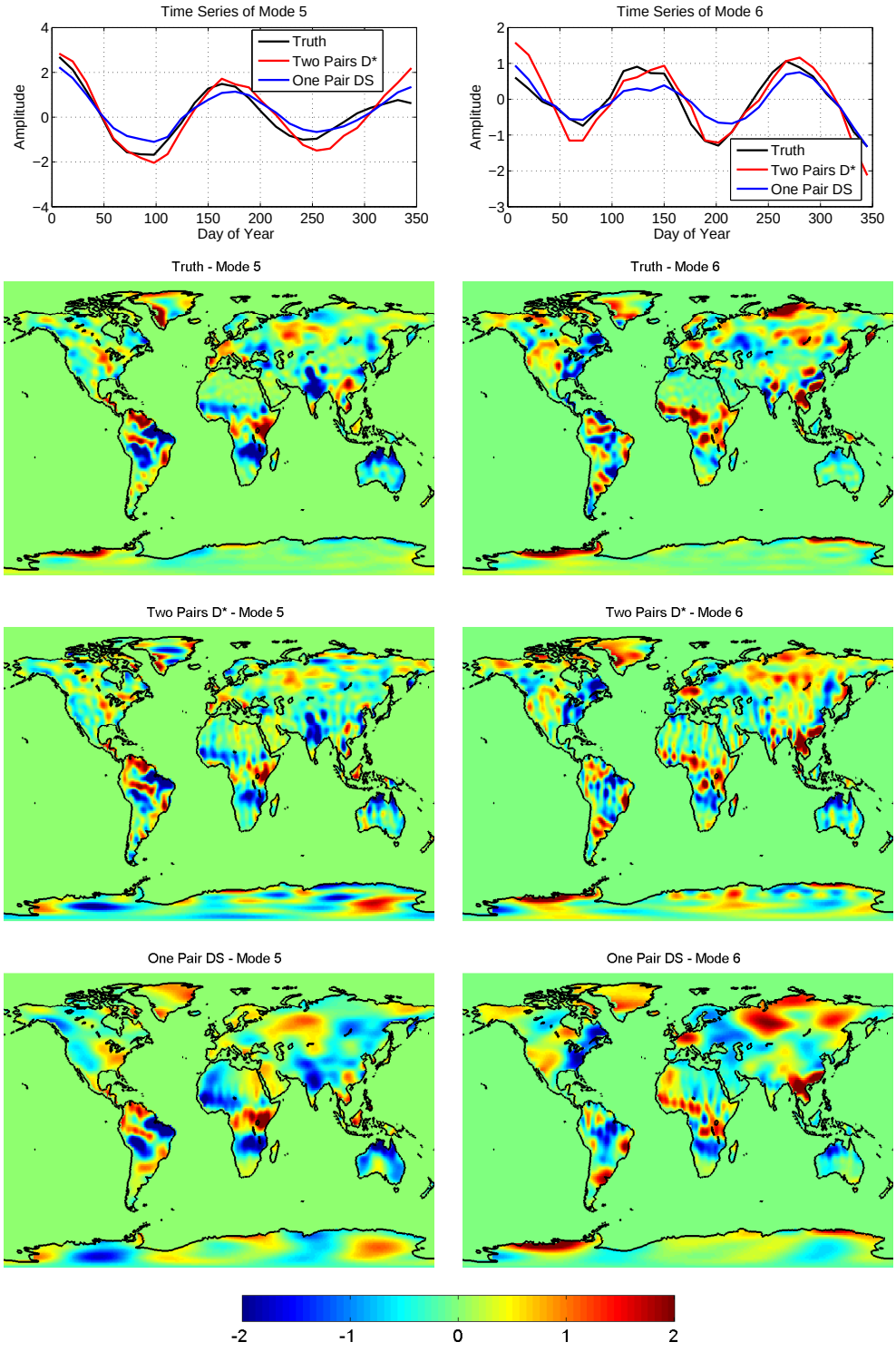

Figure 6.11: EOF analysis for recovering hydrology and ice signals. Shown are mode 5 (left column) and mode 6 (right column) with the time series (top row), truth signal(second row), recovered signal using two pairs with modified destriping (third row), and recovered signal using one pair with destriping and 300 km smoothing (bottom row). Units are in cm of EWH.

captured fairly well with two satellite pairs, but anything beyond that (i.e. the sixth mode) is poorly determined. It is seen that the first mode contains the annual signal. The second and third modes are most likely a precipitation mode with an annual variation. Given that they have the same time series, it is thought that the third mode is most likely a correction factor being applied to the second mode. The remaining modes shown (fourth, fifth, and sixth) reveal mass variations with higher frequencies, including the semi-annual signal. Perhaps the most impressive result from the EOF analysis is the ability of two satellite pairs to accurately resolve mass variations on much finer spatial scales than one satellite pair. A visual inspection of the recovered modes (particularly for the second mode) reveals small-scale hydrology signals in each continent (i.e. Alaska, central Africa, India, Australia) that are detected using two satellite pairs which are either not detected, or smoothed over, using one pair of satellites.

One does need to take care when comparing the recovered modes from each architecture, as each mission architecture recovers signals differently spatially and temporally. As such, the EOF analysis could reveal different modes (allowing for poor comparisons) between the cases. For example, examining the time series of the third mode shows that for the case of one satellite pair, the EOF analysis may be revealing a different mode than the truth signal, since the time series of mass variations increases towards the end of the year rather than decreases. Great care must be taken when making such comparisons. Perhaps a more fair comparison would be to take the first five modes from each case, add them together, then compare the ability of each architecture to recover mass variations in regions over the globe (using the first five modes only). This analysis is not performed here, as we already perform significant regional analysis using all the data; however, this process could lend additional insight into the problem.

Figure 6.12 shows the percent variance captured by the first 10 modes for each architecture. This analysis again reveals that great care must be taken when making the EOF comparisons. For example, the first mode for the truth model contains 69% of the total variance, while the first mode of the recovered signal using two satellite pairs contains only 60% of the total variance. Despite the discrepancy in percent variance captured, Figure 6.9 reveals excellent agreement both in space

and time between the truth signal and recovered signal using two satellite pairs for the first mode. The difference in the percent variance indicates that the two-pair solutions have higher modes with more power than the truth signal. Much of this power is contained in longitudinal stripes with low amplitude (as they have not been removed from the solutions via destriping processes and still exist due to small correlations between coefficients of a fixed order (see Figure 6.3)), and begin showing up in the sixth mode, as seen in Figure 6.11. Additionally, this analysis indicates that care must be taken when interpreting the GRACE results via EOF analysis. There is a large error bar when interpreting the percent variance in recovered signals, as well as the spatial and temporal signatures of the modes.

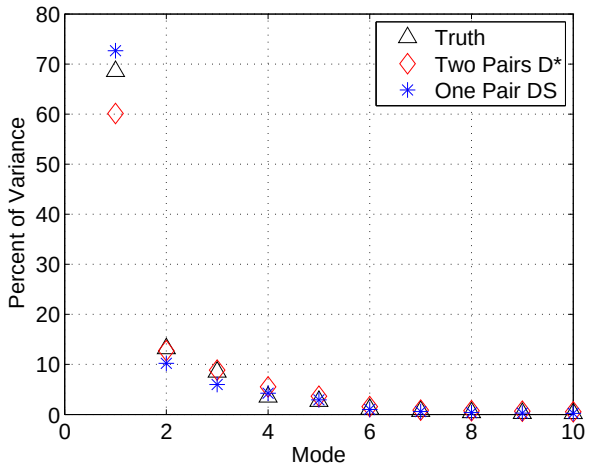

Figure 6.12: Percent variance captured by the first 10 modes

6.5.2 Ocean Bottom Pressure

The same analysis that was shown in Figures 6.7 and 6.8 can be performed for recovering OBP signals as well. Figure 6.13 and 6.14 show the ability of each architecture to recover OBP signals in the spatial domain and spectral domain, respectively. The top plot in Figure 6.13 shows the truth OBP signal which is being recovered. The middle row of plots shows the recovered signals with no post-processing applied: the left plot corresponding to solution obtained from one pair, the middle plot is for two polar pairs, and the right plot is for a polar pair coupled with a lower

inclined pair. The bottom row of plots indicates the solutions after post-processing techniques have been applied. Note that for this case, the solution obtained from the polar and lower inclined pair has been destriped via the modified destriping algorithm and smoothed with a 200 km averaging radius. The plots are truncated at degree 60, averaged over 13 days, and expressed in cm of EWH.

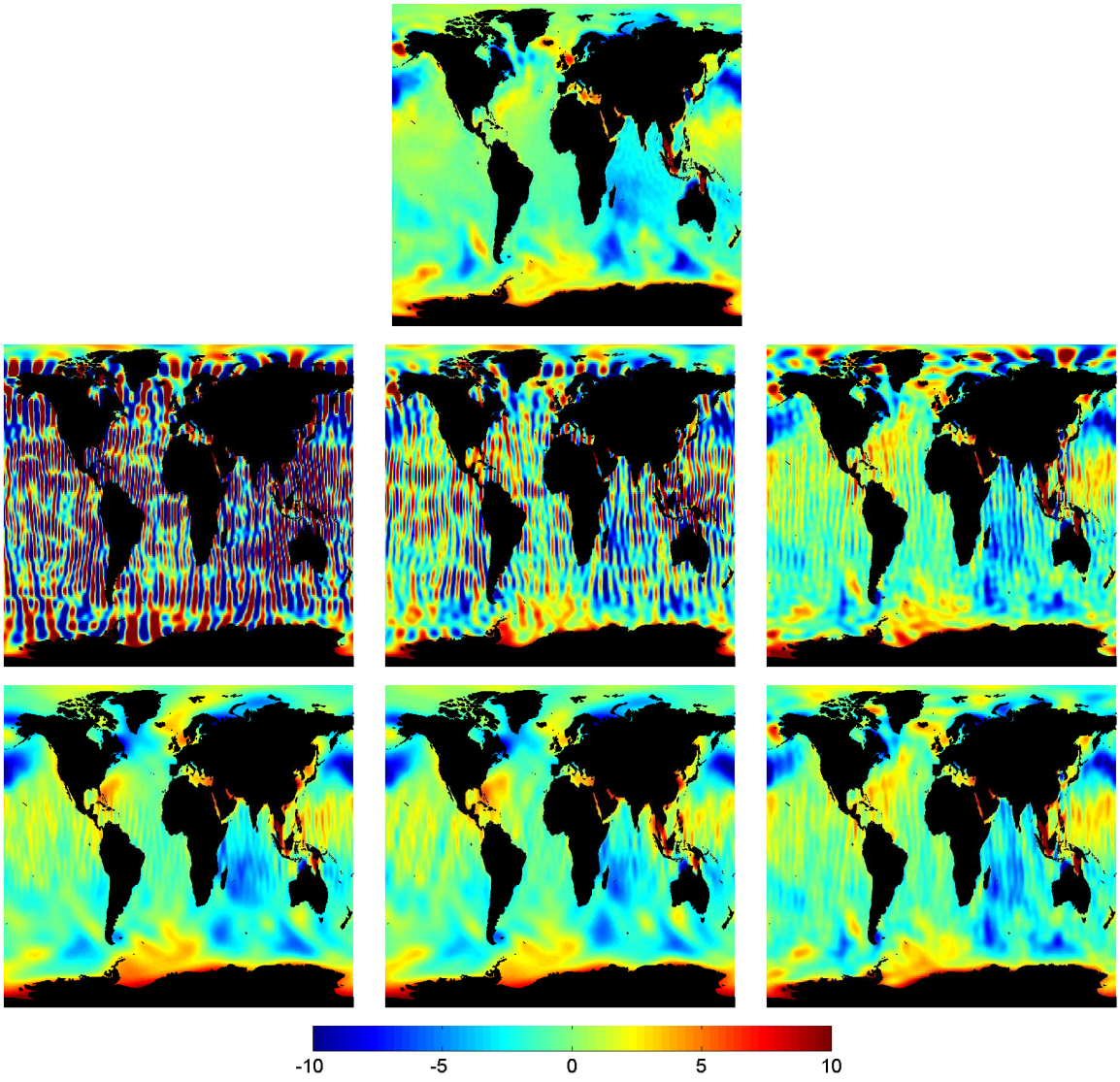

Figure 6.13: The top plot shows the truth OBP signals averaged over 13 days. The middle row shows the recovered signals for: one pair of satellites (left), two polar pairs (middle), and a polar pair coupled with a lower inclined pair (right). The bottom row shows the same recovered signals, only after post-processing has been applied. The one pair and two polar pair architectures have been destriped and smoothed with a 300 km averaging radius, while the architecture consisting of a lower inclined pair and a polar pair has been destriped via the modified algorithm and smoothed with a 200 km averaging radius. Units are in cm of EWH.

Similar to the result obtained from recovering hydrology and ice mass variations, Figure 6.13 shows that the solution obtained using two polar pairs of satellites still has predominant longitudinal striping in the solution, albeit smaller in magnitude than that with one pair of satellites. Once the solutions have been destriped and smoothed, the resulting signals are extremely similar, and have minor discrepancies. The solution obtained using a polar pair and lower inclined pair of satellites has considerably less error than the other two cases. However, there is noticeable longitudinal striping in the solution, unlike the results shown in Figure 6.7 pertaining to recovering hydrology and ice mass variations. The reason for this is simply a matter of scale: OBP signals are smaller in magnitude than hydrology and ice signals, hence, there is a smaller signal to noise ratio when detecting them. Errors which manifest as longitudinal stripes simply are not as visible in Figure 6.7 because the magnitude of the hydrology and ice mass variations is so much larger than the magnitude of the stripes. We have found that smoothing the OBP solutions with a 200 km averaging radius gives similar results as destriping and smoothing the one-pair results with a 300 km radius. Alternately, one could truncate at a lower degree to remove the stripes, as they predominantly manifest from errors in higher degree terms. Note that the errors at high latitudes have been removed via the modified destriping algorithm. Comparing all three post-processed cases reveal minor discrepancies between them due to the commonality of smoothing invoked. However, there are certain signals, particularly those off the coast of Alaska and in the Southeast Pacific Ocean, which appear to be better determined with the addition of a lower inclined pair of satellites. Again, regional analyses are necessary to further investigate the differences.

Finally, Figure 6.14 displays the error of each architecture in recovering OBP signals in terms of geoid height as a function of spherical harmonic degree. Again, the left plot is for solutions with no post-processing and the plot on the right is after the solutions have been post-processed via the same techniques as for Figure 6.13. This plot shows minor improvements with the addition of the second polar pair of satellites. The addition of the lower inclined pair of satellites improves the solution even more at high degrees. However, the error for all three cases is shown to exceed the power in the signal at approximately degree 15, indicating near-equal performance between

the three cases. After post-processing, the solutions are nearly identical. Regional analyses are necessary to further quantify improvements that adding a second pair of satellites provides in determining OBP variations. It is expected that the addition of the lower inclined pair will provide increased spatial resolution for determining local signals, as the error is shown to be only slightly above the power in the signal out to degree 30, where the other cases have considerably higher error at this point.

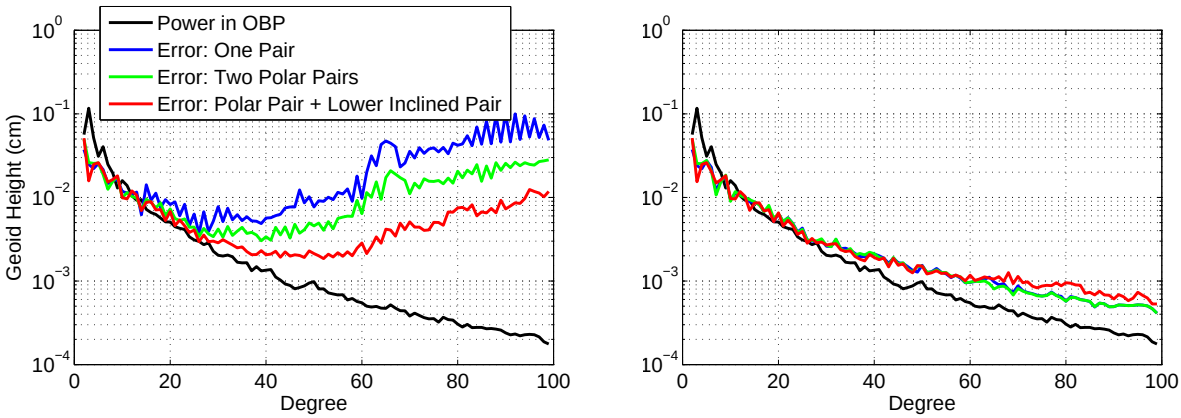

Figure 6.14: Geoid degree error for recovering OBP signals in Figure 6.13 with no post-processing (left) and post-processing (right)

6.5.3 Dominant Error Source

It is worthwhile to understand what the dominant source of error is associated with these hypothetical mission architectures. Figure 1.2 separates the error sources for an architecture in a 30-day repeat period at a higher altitude. We can perform the same analysis for the mission architectures considered here, at a lower altitude and in a 13-day repeat period. Figure 6.15 shows the geoid degree error for the one satellite pair architecture (left) and the architecture consisting of a polar pair coupled with a lower inclined pair of satellites (right). Each error source has been isolated such that its individual effect can be studied. The AOD errors are given by mismodelling atmosphere and ocean models while the tide errors are given by mismodelling the tides. The hydrology and ice errors are given by the undersampling of these phenomena over the

13-day timespan, and the measurement system errors are defined as the errors due to the laser interferometer as well as the drag-free system onboard. It is seen that for both cases, errors in determining the satellite positions have the least effect on the final solution while AOD errors dominate the solution at low degrees. Errors from tide models become commensurate with those from the AOD models at higher degrees.

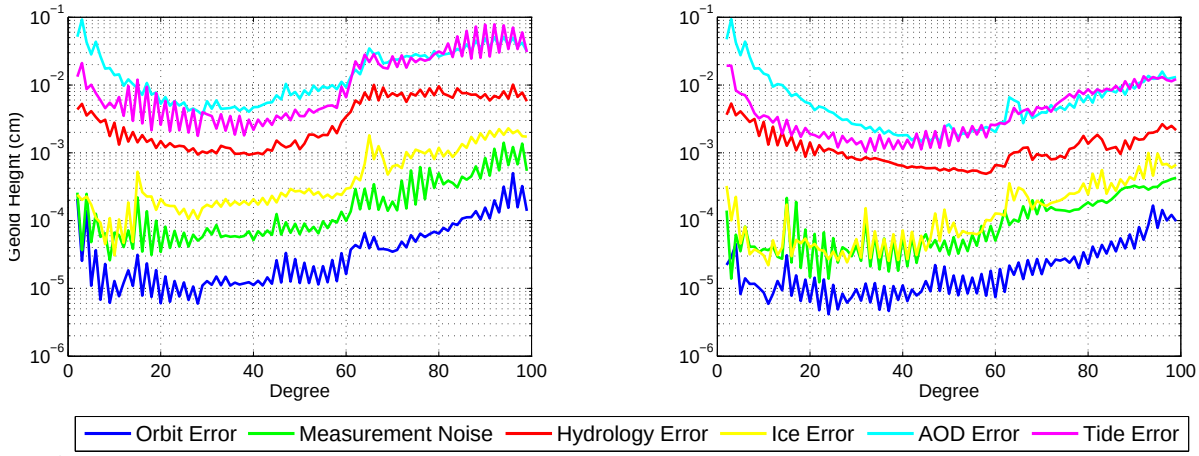

Figure 6.15: Geoid height error from isolated sources of error for one pair of satellites (left) and a polar pair coupled with a lower inclined pair of satellites (right)

These results indicate that in order to further improve upon the two-pair solutions (and lower the level of AOD errors), the sampling frequency of the mission would need to be increased through the addition of more satellite pairs. While it is seen that AOD errors dominate the error budget when averaged globally, one should not assume from this analysis that AOD errors will dominate the error budget for all regions of interest, due to the complex space-time sampling characteristics of signals and errors. As was shown in *Loomis* [2009], while AOD errors dominate the error budget when looking at mass variations in Greenland, the largest source of error when determining mass variations in the Amazon is actually due to undersampling hydrology. The reason for the discrepancy is due to better knowledge of atmospheric mass variations in South America versus Greenland. Hence, each specific region will have its own limiting source of error when determining mass variations. Regional analysis identifying the dominant source of error for specific regions of

interest is not performed in this study.

6.6 Results: A Regional Perspective

Analyzing the expected performance of a mission regionally is necessary to fully understand its capabilities. In order to perform regional analyses, we use averaging kernels and spatiospectral localization, the details of which are presented in Sections 2.3.2.1 and 2.3.2.2. Results in Section 6.6 showed that while the case of two polar pairs of satellites has lower errors than one polar pair of satellites, correlated errors manifesting as longitudinal stripes still dominate the solutions. Hence, these solutions necessitate standard GRACE post-processing techniques including destriping and smoothing. Once these are applied to the solutions, the recovered mass variations are nearly identical to those obtained using only one pair of satellites (after post-processing). Thus, one can expect similar performance from the cases of one pair of satellites and two polar pairs of satellites. As such, it is not necessary to examine the errors on a regional level, and the case of two polar pairs of satellites is not discussed in this section. Any reference to two satellite pairs in this section refers to the case of a polar pair of satellites coupled with a lower inclined pair of satellites.

6.6.1 Hydrology

The Amazon river basin has been the subject of many analyses using GRACE data due to the magnitude of the signal as well as the large spatial extent of the region. This region makes an excellent candidate to compare the capabilities of the one-pair and two-pair architectures using the spatiospectral localization technique. A spherical harmonic expansion of degree $L_h = 10$ with a spherical cap radius of $\theta_o = 45^\circ$ is used to calculate the optimal windowing function. The results from a single 13-day gravity solution are displayed in Figure 6.16.

Visually, one can see the improved spatial resolution that two pairs of satellites allow for in this region over the case of one pair. As expected, the one pair results contain the longitudinal stripes, and once these results are destriped and smoothed, the signals are damped and much of the finer spatial resolution is lost. Figure 6.17 shows the localized signal to noise ratio (SNR) computed

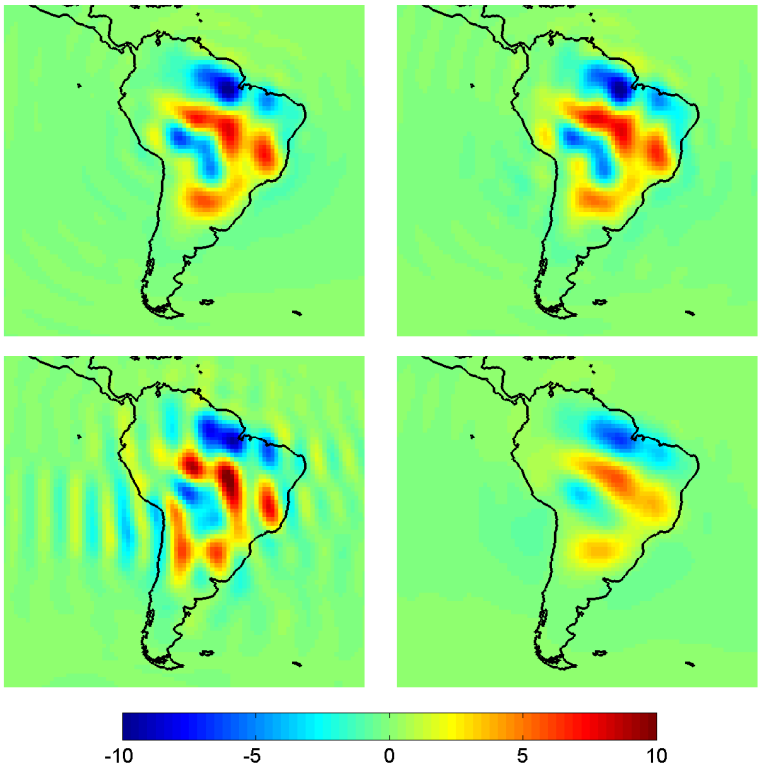

Figure 6.16: Spatiospectral localization technique applied to the Amazon region using $\theta_o = 45°$, $L_h = 10$. Truth signal (top-left) along with the recovered signals from: two pairs of satellites (top-right), one pair of satellites (bottom-left), and one pair of satellites DS (bottom-right) averaged over 13 days. Units are in cm of EWH.

from a localized degree-RMS plot. It is seen that for two pairs of satellites, the SNR is positive out to degree 50, corresponding to a spatial resolution of approximately 400 km. Alternately, for the case of one pair of satellites, one could argue that information is only present out to approximately degree 30, corresponding to a spatial resolution of approximately 667 km. Furthermore, the SNR for two satellite pairs is substantially higher than for the case of one pair for all degrees greater than 8, allowing for greater accuracy in determining the signal.

Next, we can use averaging kernels to calculate mass variations over the year in 53 different hydrological basins shown in Figure 6.18. This selection of basins represents different basin sizes, latitudes, geographic orientations, signal strenghts, etc, and gives a good sampling on the type of performance one could hope to achieve with two pairs of satellites over one pair of satellites. Figure

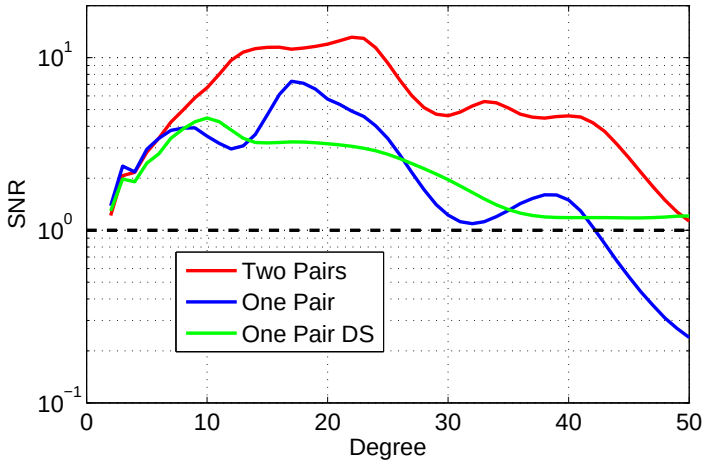

Figure 6.17: Signal to noise ratio for mass variations in the Amazon computed with the spatiospectral localization technique (see Figure 6.16).

6.19 focuses on the results for the Fraser Basin (Basin 18), in northwestern British Columbia. Mass variations for this analysis were calculated each day using a sliding boxcar filter with a window width of 13 days centered on the day of interest. Each solution has approximately the same spatial information in it, given that the orbits are in repeating groundtracks; however, it has different space-time sampling characteristics. Note that these solutions are not true "daily" solutions in the sense that solutions between days are independent from one another. In fact, independent solutions will happen every 13 days. It is also not being argued that this type of filter is optimal for recovering mass variations each day, as other filters have been explored for this purpose, including using a Gaussian filter similar to the boxcar filter that we use [*Bonin*, 2010], as well as using a Kalman filter during the estimation process to gain daily solutions [*Kurtenbach et al.*, 2009]. This simple analysis, however, allows one to see the variability in the solutions resulting from replacing a single day of data.

Figure 6.19 illustrates the mass variations in the basin calculated using an averaging kernel over the entire year in daily increments. Shown are the solution for one pair of satellites with no post-processing, the one pair solution that has been destriped and smoothed, the one pair solution that has been destriped and smoothed with a scale factor (SF) applied, and the solution given two

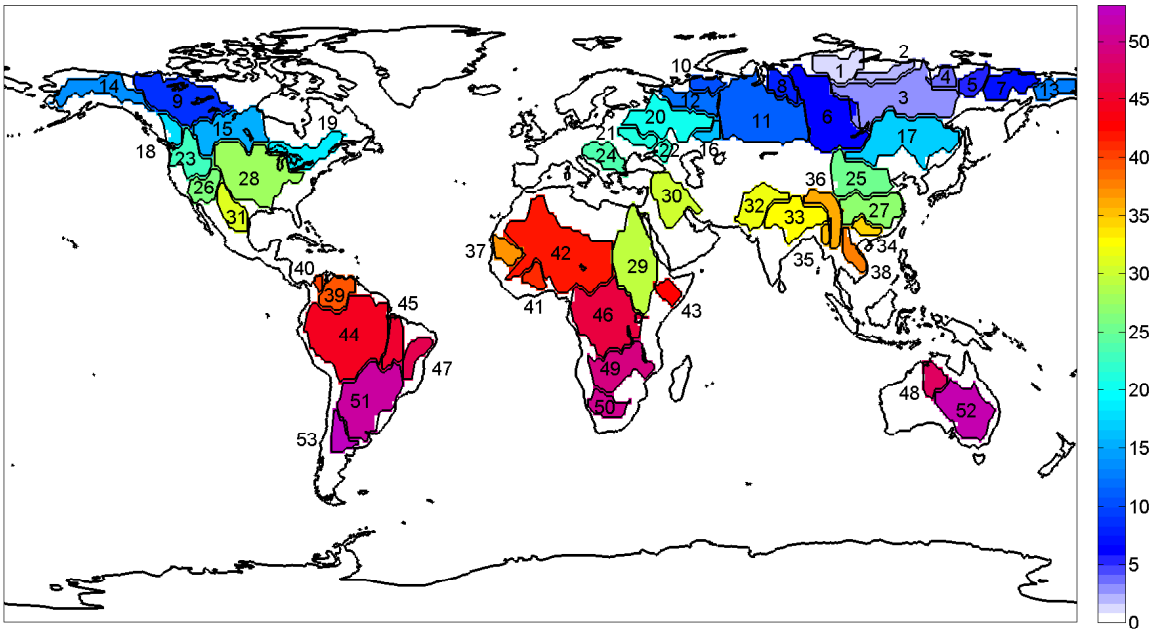

Figure 6.18: Map showing the location of the 53 hydrological basins for which averaging kernels are computed

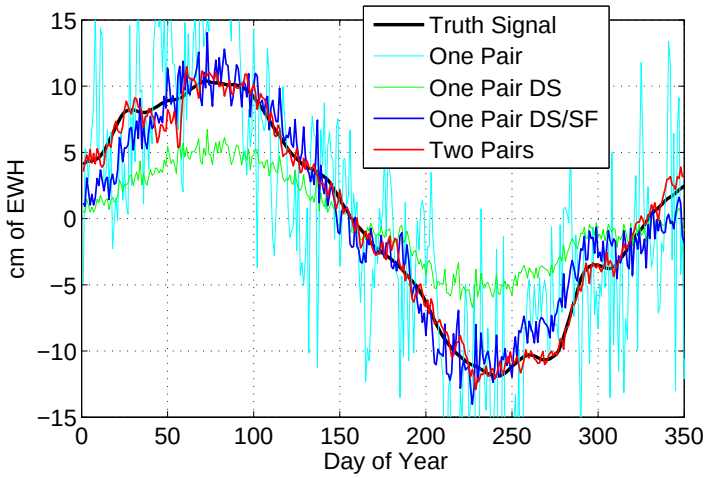

Figure 6.19: Mass variations calculated in the Fraser Basin (Basin 18) over the year for one pair of satellites, one pair of satellites DS, one pair of satellites DS with a scale factor applied, and for two pairs of satellites.

pairs of satellites. Scale factors are used within the GRACE community to account for signal that

the destriping and smoothing processes remove from the solution including leakage error. Typically, they are calculated by taking a model representing mass variations in the region, destriping and smoothing that model, and calculating how much mass has been removed via these processes. A scale factor is then calculated to restore this lost mass. For this study, we calculated scale factors three ways: (1) using the *truth* GLDAS hydrology model, (2) using an alternate hydrology model provided by the European Space Agency (ESA), and (3) using a uniform mass distribution over the basin. It was found that the scale factor computed was extremely sensitive to which method was used due to the empirical nature of the destriping filter. In fact, using a scale factor from methods (2) and (3) provided worse results on average than not using a scale factor at all. Thus, it was decided to compute scale factors using method (1): destriping and smoothing the *truth* model. This leads to overly-optimistic results for the case of one pair of satellites, as it represents the best possible scale factor one could hope to compute. Hence, the actual level of mass variations for one pair of satellites that one would compute most likely lies somewhere between the case of not applying any scale factor, and the case of applying the best possible scale factor.

Figure 6.19 illustrates that the signal calculated using one pair of satellites, but without post processing, has extremely large variability, varying by as much as 15 cm EWH from one time step to the next. Once the solution is destriped and smoothed, the variability in the solution decreases substantially; however, the signal is damped in amplitude with respect to the truth signal. Figure 6.18 illustrates that the Fraser Basin is predominantly oriented in the North-South direction. As such, the destriping process removes a substantial amount of signal (in addition to error) from the basin since the empirical filter developed by *Swenson and Wahr* [2006] is designed to remove North-South features. After applying the scale factor to account for this loss of signal, the one pair solution compares fairly well with the truth signal. The solution obtained from two pairs of satellites, however, still agrees much better with the truth signal than the best-case scenario involving one pair of satellites. The reader should be reminded, as well, that no post-processing has been applied to the solution involving two pairs of satellites.

Figures 6.20, 6.21, 6.22, and 6.23 show the mass variations over the year for all 53 hydrological

basins. The case of one polar pair with no post-processing is not shown in this series of plots due to the large errors associated with it. There are certain basins which have the same recovered mass variations using one pair of satellites whether a scale factor is applied or not. This is a unique circumstance in which the scale factor is calculated to be equal to 1, or has been manually set to 1 due to an unreasonably large calculated value for the scale factor. A close examination of the mass variations over the year for all basins reveals the additional accuracy provided with the addition of a lower inclined pair of satellites (see particularly Basins 1, 2, 19, 21, 22, 24, 32, 36, and 50).

Table 6.1 summarizes the results in Figures 6.20, 6.21, 6.22, and 6.23, showing the RMS of the errors (in cm of EWH) calculated over the year for all 53 basins that were analyzed. Listed are the name of each basin, the area, the amplitiude (amp.) of the signal in the basin over one full year (taken to be half of the peak-to-peak amplitude), as well as the RMS of the error for each case. Note that 'reg' stands for 'regular' and indicates no post-processing.

Table 6.1: Hydrological Basins and the RMS of the error in determining mass variations in each basin over one full year for the cases of one pair of satellites, one pair of satellites destriped and smoothed, one pair of satellites destriped and smoothed with an optimal scale factor applied, and two pairs of satellites

Basin No.	**Basin Name**	**Area (km^2)**	**Amp. (cm)**	**One Pair RMS (cm)**			**Two Pairs RMS(cm)**
				Reg.	**DS**	**DS/SF**	
1	Khatanga-Popigai	501,552	6.58	5.68	1.68	1.26	0.66
2	Olenek	309,322	2.83	4.24	1.69	1.00	0.82
3	Lena	2,415,920	3.51	1.56	0.78	0.79	0.78
4	Yana	242,039	2.97	11.26	1.54	1.29	0.98
5	Indigirka	341,076	3.33	10.95	1.51	1.99	1.23
6	Yenisei	2,376,483	4.38	2.32	0.81	0.79	0.64
7	Kolyma	617,341	5.51	5.19	2.09	1.83	1.53
8	Taz	382,104	10.87	7.26	1.36	1.08	0.79
9	Mackenzie	1,770,040	4.53	1.26	1.01	0.92	0.63
10	Pechora	254,272	10.52	7.06	1.65	1.29	1.24
11	Ob	3,012,693	7.59	1.32	0.91	0.92	0.74
12	Severnaya Dvina	661,781	10.91	1.79	1.22	0.98	0.89
13	Anadyr	410,068	5.12	6.57	2.02	1.46	1.26
14	Yukon	940,852	5.90	2.47	1.42	1.39	0.95
15	Nelson	1,693,827	4.18	1.54	0.67	0.62	0.52
16	Ural	312,629	5.35	4.92	1.07	1.14	1.09

Continued on next page

Table6.1 – continued from previous page

Basin No.	Basin Name	Area (km^2)	Amp. (cm)	One Pair RMS (cm)			Two Pairs RMS(cm)
				Reg.	DS	DS/SF	
17	Amur	2,876,880	3.87	1.28	0.82	0.85	0.63
18	Fraser	357,057	11.15	6.04	4.14	1.83	0.77
19	Saint Lawrence	1,263,145	6.04	1.63	1.21	1.20	0.47
20	Volga	1,580,750	6.17	1.41	0.94	0.91	0.65
21	Dnieper	446,335	8.34	2.85	1.21	1.15	0.73
22	Don	278,565	7.21	6.75	2.21	1.96	1.05
23	Columbia	1,048,534	6.56	2.79	1.95	1.07	0.63
24	Danube	836,815	10.47	2.23	1.76	1.19	0.64
25	Yellow River	1,872,050	4.12	1.40	0.88	0.91	0.66
26	Colorado (U.S.)	838,512	1.32	2.65	0.83	0.93	0.79
27	Yangtze River	1,833,747	4.34	1.56	0.92	0.93	0.62
28	Mississippi	3,525,101	4.19	0.90	0.53	0.53	0.46
29	Nile	3,761,542	3.54	1.94	0.92	0.96	0.57
30	Shatt al-Arab	1,732,018	2.39	2.11	0.95	1.04	0.64
31	Rio Grande	1,021,678	3.54	2.37	1.05	1.49	0.85
32	Indus	1,429,312	3.19	2.17	1.05	1.18	0.70
33	Ganges	1,920,796	10.12	1.53	1.23	0.82	0.62
34	Pearl River	439,492	9.22	3.64	1.42	1.33	1.30
35	Irrawaddy	296,014	3.94	8.54	2.14	0.91	1.89
36	Salween	1,014,279	2.63	3.67	1.48	1.35	0.93
37	Sénégal	765,749	3.49	2.47	0.99	0.91	1.25
38	Mekong	743,472	11.34	3.01	2.91	1.63	1.26
39	Orinoco	1,255,019	10.04	1.99	1.28	1.08	0.95
40	Magdalena	195,874	9.59	8.76	2.69	2.01	1.81
41	Volta	572,618	12.17	3.24	1.43	1.15	1.14
42	Niger	6,918,253	4.83	0.97	0.74	0.70	0.39
43	Jubba	627,755	4.63	3.05	0.99	1.18	1.14
44	Amazon	6,129,528	8.11	0.97	0.82	0.74	0.49
45	Tocantins	1,011,450	18.44	3.62	3.22	2.09	1.29
46	Zaire	4,449,039	3.57	1.02	0.92	0.91	0.56
47	São Francisco	904,455	8.89	3.26	1.59	1.62	1.18
48	Victoria	816,232	7.90	3.50	1.12	1.12	1.14
49	Zambezi	2,351,974	10.18	1.19	1.32	0.84	0.52
50	Oranje	891,596	2.15	2.03	1.66	1.66	0.80
51	Paraná	3,635,738	7.38	1.34	1.40	1.10	0.48
52	Murray	2,452,873	2.63	1.92	1.06	1.09	0.76
53	Colorado (Argentina)	659,923	3.46	4.54	0.89	1.01	1.16
	RMS of RMS			**4.22**	**1.55**	**1.23**	**0.94**

Studying the RMS values in Table 6.1 reveals that in all but four of the basins, two pairs of satellites have a lower RMS than for the case of one pair of satellites being destriped and smoothed

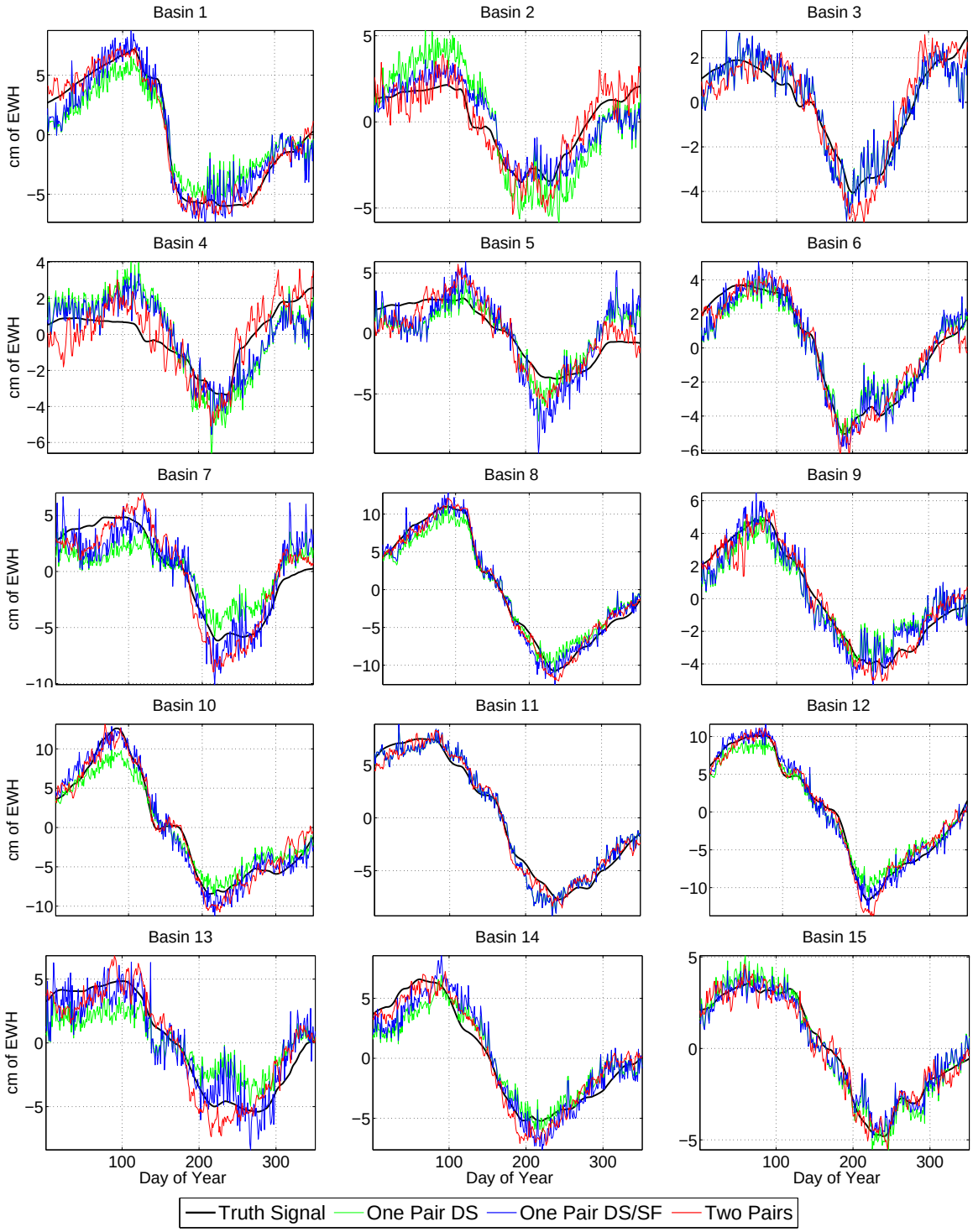

Figure 6.20: Comparison of recovered hydrological mass variations in Basins 1-15. Shown are the truth signal (black), and recovered signals from one pair (green), one pair DS (blue), and two pairs (red).

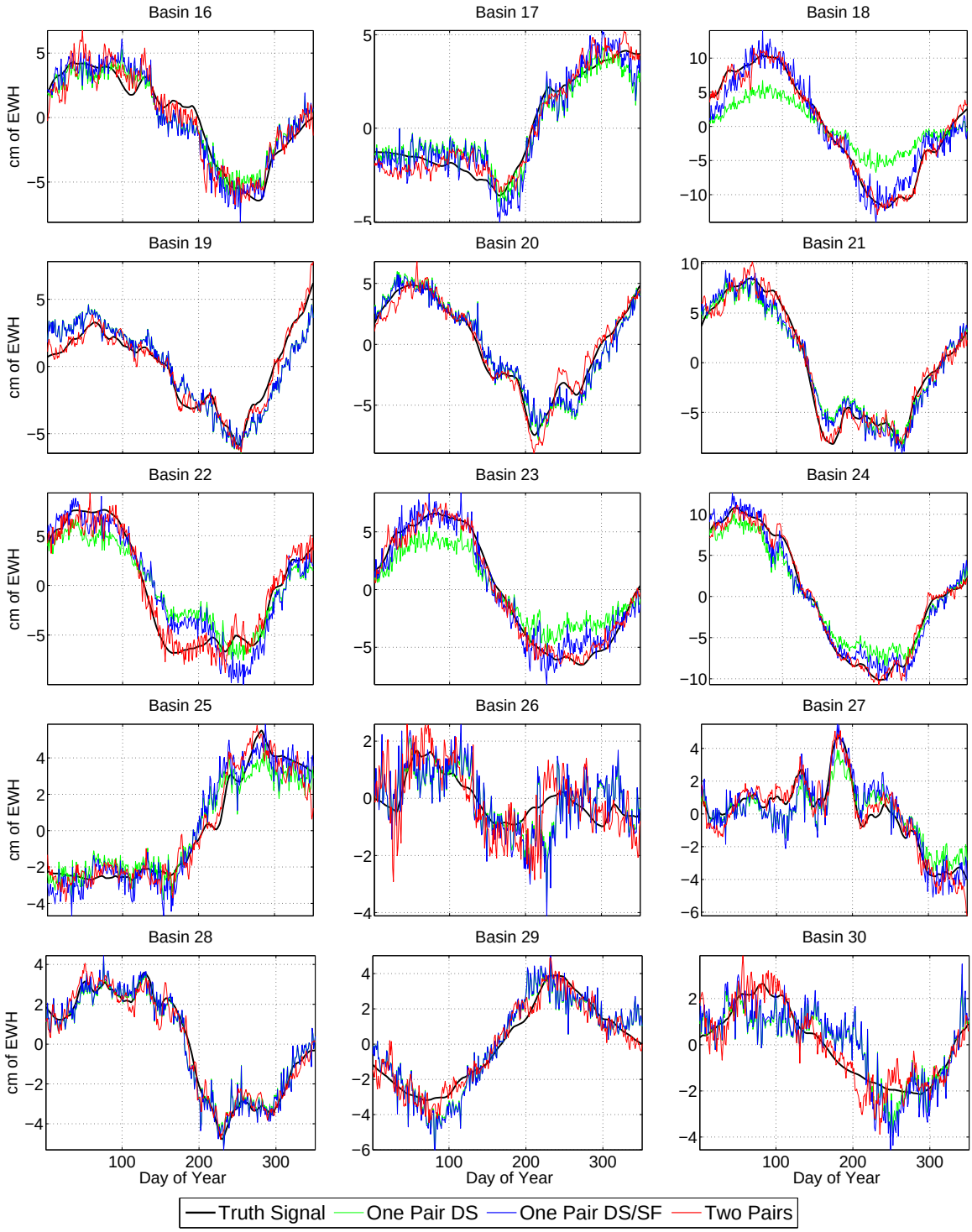

Figure 6.21: Comparison of recovered hydrological mass variations in Basins 16-30. Shown are the truth signal (black), and recovered signals from one pair (green), one pair DS (blue), and two pairs (red).

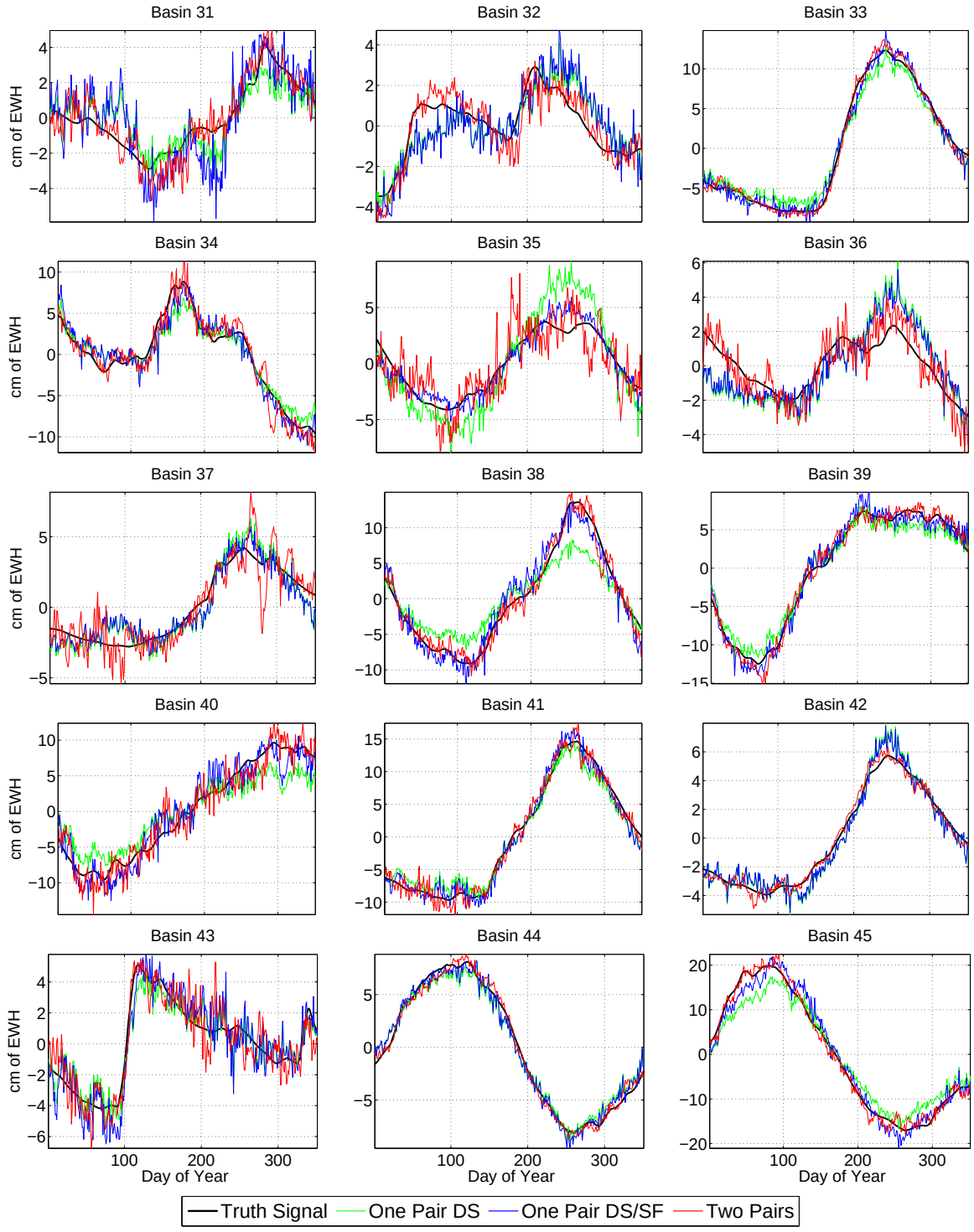

Figure 6.22: Comparison of recovered hydrological mass variations in Basins 31-45. Shown are the truth signal (black), and recovered signals from one pair (green), one pair DS (blue), and two pairs (red).

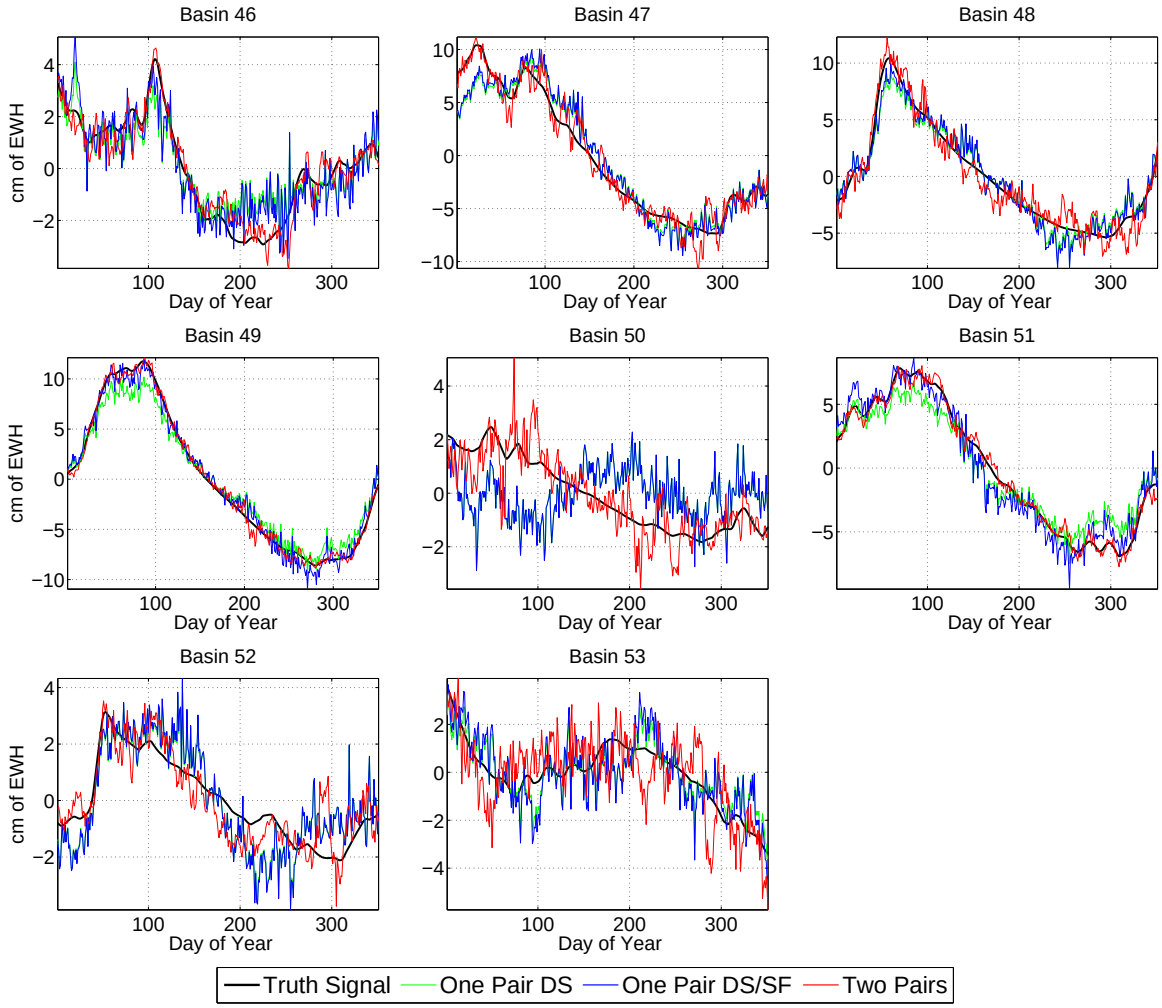

Figure 6.23: Comparison of recovered hydrological mass variations in Basins 46-53. Shown are the truth signal (black), and recovered signals from one pair (green), one pair DS (blue), and two pairs (red).

with an optimal scale factor applied. It has a lower RMS than the one-pair case with no post-processing 100% of the time. Furthermore, if one looks at the effect of applying the scale factor, it is seen that in some cases, the scale factor actually makes the solution slightly worse. This indicates the risks that one takes by applying scale factors to the mass estimates. Even given an optimal scale factor, the results sometimes degrade.

Finally, Figure 6.24 provides a summary, showing the RMS of the yearly error RMS values for the 53 basins displayed in Table 6.1 for each case. From this chart, it can be concluded that two pairs of satellites determine the hydrological mass variations in the basins with approximately 25%

more accuracy than the case of one pair of satellites destriped and smoothed with an optimal scale factor applied, 40% more accuracy than the case of one pair of satellites destriped and smoothed with no scale factor applied, and 80% more accuracy than in the case of one pair of satellites with no post-processing.

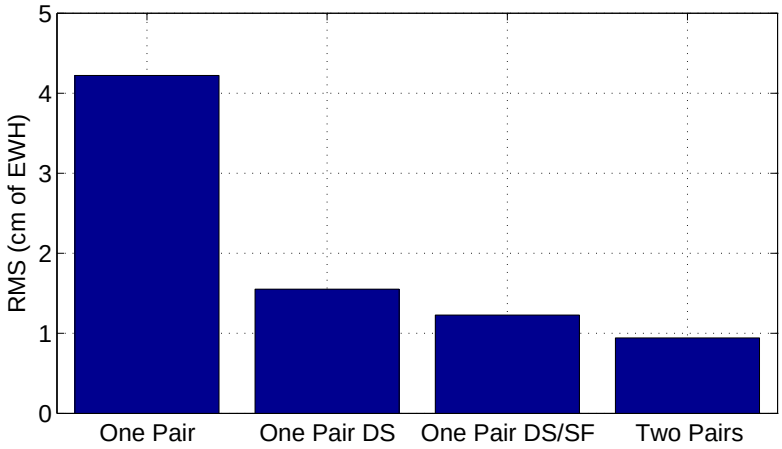

Figure 6.24: RMS of the yearly error RMS values shown in Table 6.1 for determining mass variations in the 53 hydrological basins. Units are in cm of EWH.

6.6.2 Ice Mass Variations

Ice mass variations are defined as mass variations in Greenland and Antarctica. Unfortunately, a model defining glaciers was not available at the time of publication. In order to study ice mass variations on a regional scale, Greenland has been subdivided into 12 basins, as shown in Figure 6.25, in accordance with basin definitions given in *Luthcke et al.* [2006]. The melting of Greenland around the coastal areas, particulaly the southern regions, has been the focus of many recent investigations due to accelerating melting rates. As such, detailed simulation results for mass variations in Basin 5, along the southwestern coast of Greenland, are shown in Figure 6.26.

Figure 6.26 paints a similar picture as that of the Fraser basin shown in Figure 6.19. The solution from one pair of satellites is extremely noisy; however, once the solutions are destriped and smoothed, the daily variability has decreased and the amplitude of the signal has been suppressed

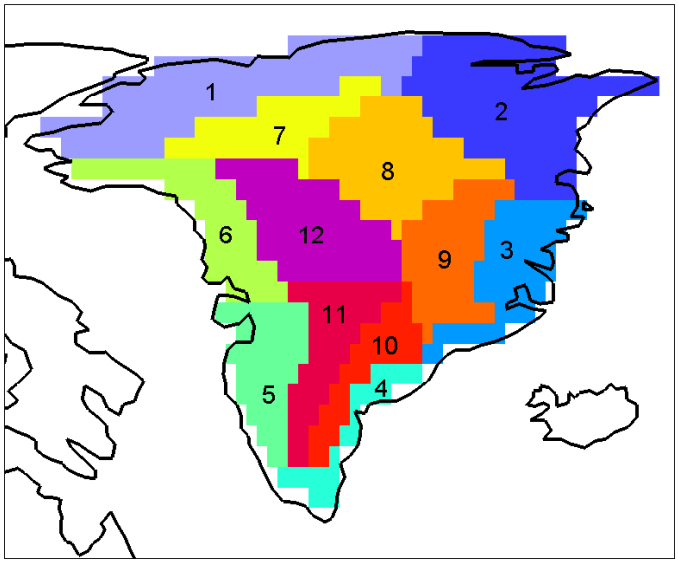

Figure 6.25: Map showing the location of the 12 Greenland basins

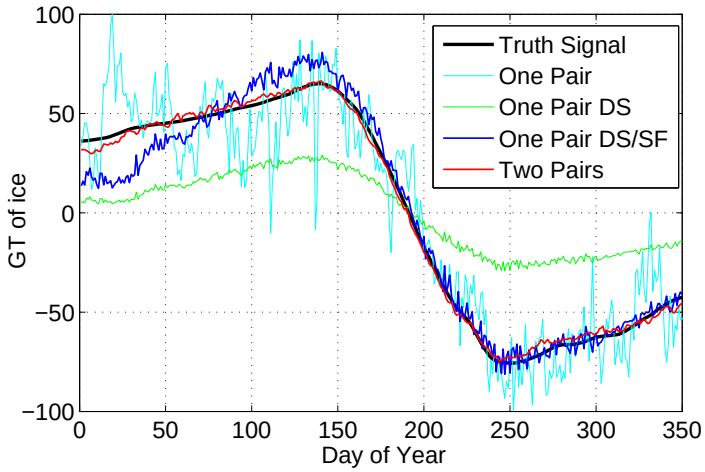

Figure 6.26: Mass variations calculated in southwestern Greenland (Basin 5) over the year for one pair of satellites, one pair of satellites DS, one pair of satellites DS with a scale factor applied, and for two pairs of satellites.

with respect to the truth. This is in a large part due to the North-South orientation of this particular basin, and the fact that the destriping process is designed to remove North-South features in the gravity field. Once an optimal scale factor is applied, the amplitude has been restored and the

calculated mass matches much closer to the truth. However, particularly for the first half of the year, there is a poor estimate of the rate of mass increase. Two pairs of satellites, conversely, recover the true mass variations in the basin with very good accuracy for the duration of the year. It should be noted that no post-processing has been applied to the solution for two pairs of satellites.

Figure 6.27 shows the mass variations in all twelve Greenland basins over the year. Again, the case of one polar pair of satellites with no post-processing is not shown due to the large scale of the errors associated with this case.

Table 6.2 summarizes the results in Figure 6.27 and shows the calculated error RMS values for all 12 Greenland basins over the year. For the sake of comparison, the RMS of the error for the case of destriping the two-pair case via the modified destriping algorithm (indicated by D*) with and without a scale factor applied is shown. It is seen that on average, destriping the two-pair solutions slightly degrades the accuracy. The three basins that are improved when destriping (without applying a scale factor) are Basins 2, 8, and 12, all of which are located at higher latitudes. After applying an optimal scale factor, Basins 2, 3, 4, 8, 10, and 12 have improved mass estimates; however, on average, the results are still slightly worse. It is not terribly surprising that destriping via the modified algorithm results in overall slightly degraded results, since the basins are at latitudes both above and below 72^o. In all but 2 of the basins, two pairs of satellites provide lower RMS values than the best case scenario using one pair of satellites. Two pairs of satellites provide lower RMS values 100% of the time over what one pair of satellites provides with no post-processing. Again, it should be noted that applying an optimal scale factor does not always guarantee a better solution for the case of one pair of satellites, indicating that care must be taken when applying scale factors to real data. Finally, the reason that the magnitude of the RMS values are larger than those associated with hydrology has to do with several factors. First, as was shown in *Loomis* [2009], AOD errors in Greenland are much larger than errors over areas such as the Amazon, or North America, where there is much more data to have good AOD models. Second, high degree resonant order coefficients manifest themselves spatially between 70^o and 75^o, which is where Greenland lies. Particularly for the case of a single pair of satellites, the errors at high degree

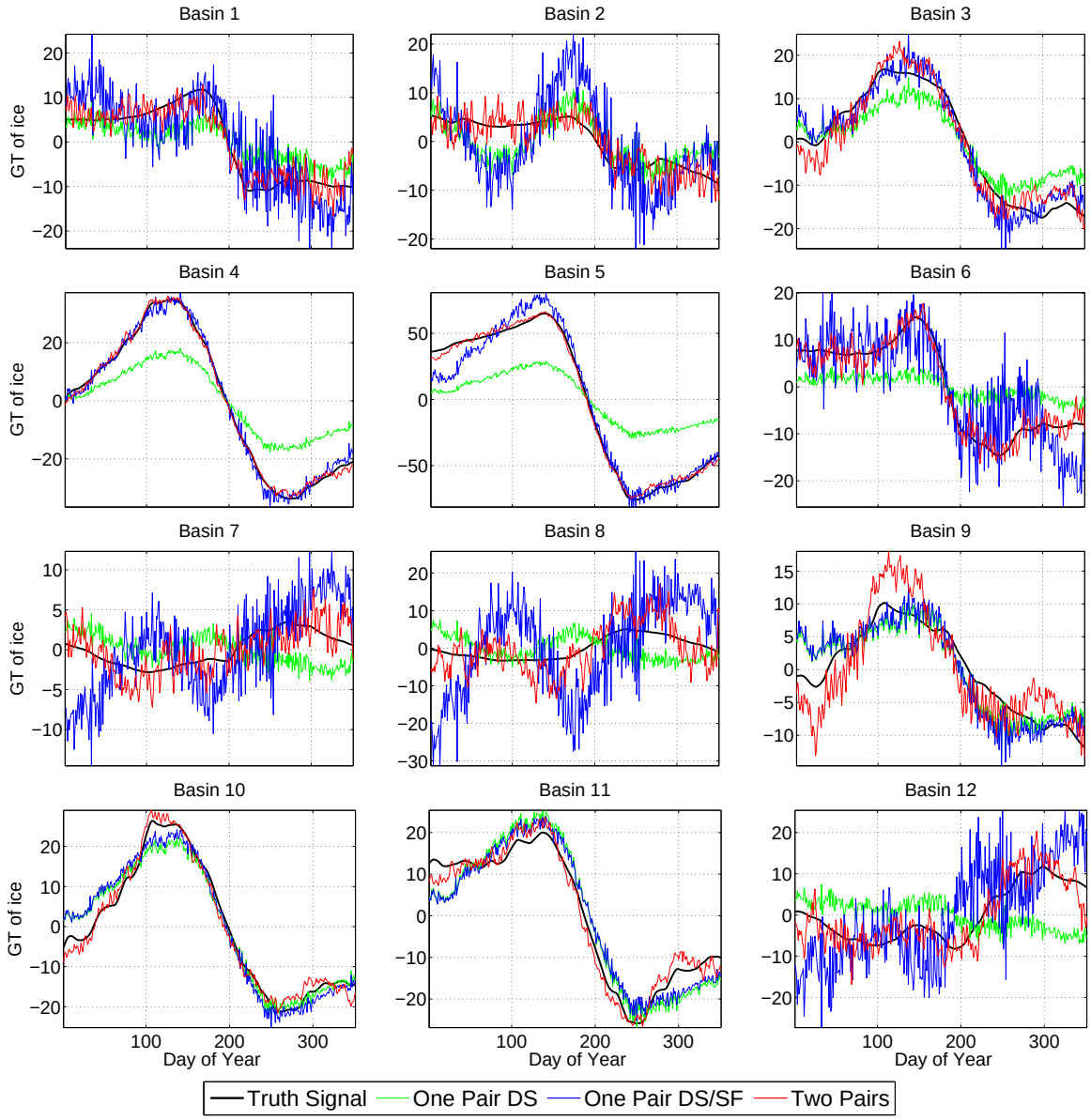

Figure 6.27: Comparison of recovered mass variations in all twelve Greenland basins over the year. Shown are the truth signal (black), and recovered signals from one pair (green), one pair DS (blue), and two pairs (red).

resonant coefficients are large, as seen in Figure 6.2, and as such, there is a substantial amount of error at this latitude band.

Finally, Figure 6.28 summarizes the RMS of the yearly error RMS values displayed in Table 6.2 over the 12 Greenland basins. It can be concluded that on average, two pairs of satellites provide mass estimates for Greenland that are approximately 55% more accurate than in the case of one

Basin No.	Area (km^2)	Amp. (GT)	One Pair RMS (GT)			Two Pairs RMS (GT)		
			Reg.	DS	DS/SF	Reg.	D*	D*/SF
1	207,331	11.36	4.63	5.56	6.26	2.83	3.91	3.14
2	225,127	6.97	9.77	4.19	7.49	2.73	2.60	2.66
3	178,723	17.14	21.04	5.23	3.29	3.31	3.52	2.90
4	109,816	34.34	7.03	12.37	1.97	1.21	1.41	1.15
5	194,759	70.35	17.86	34.52	9.63	2.82	3.34	3.22
6	149,417	14.72	17.64	7.91	6.51	2.06	3.98	3.01
7	103,225	3.14	3.63	3.15	5.01	2.10	2.82	4.42
8	190,789	4.18	9.57	4.79	12.05	4.77	2.54	3.99
9	191,186	11.02	28.12	2.94	3.21	4.08	4.34	4.36
10	146,600	23.84	14.31	3.36	3.41	2.06	2.08	1.96
11	196,199	22.95	21.32	4.87	4.49	2.46	3.56	2.53
12	235,481	9.97	21.06	8.78	9.74	3.66	2.69	3.50
RMS of RMS			**16.43**	**11.68**	**6.78**	**2.99**	**3.17**	**3.20**

Table 6.2: Greenland Basins and the RMS of the error (expressed in GT of ice) in determining mass variations in each basin over one full year for the cases of one pair of satellites, one pair of satellites destriped and smoothed, one pair of satellites destriped and smoothed with an optimal scale factor applied, and two pairs of satellites

pair of satellites that have been destriped and smoothed with an optimal scale factor applied, 75% more accurate than in the case of one pair of satellites that have been destriped and smoothed without applying a scale factor, and 80% more accurate than in the case of one pair of satellites with no post-processing.

To confirm that two pairs of satellites does not degrade the ability to detect ice mass variations in Antarctica, we do a simple mass balance estimate on the entire continent of Antarctica using an averaging kernel. Figure 6.29 shows total mass in Antarctica over the year. The solutions from one pair of satellites have been destriped and smoothed with a 300 km averaging radius, while the results from two pairs of satellites have been destriped with the modified destriping algorithm. No scale factors have been applied to the data as models for ice mass variations in Antarctica are not expected to be very accurate. It is seen that the RMS of the errors is decreased by 38% using two pairs of satellites versus one pair of satellites.

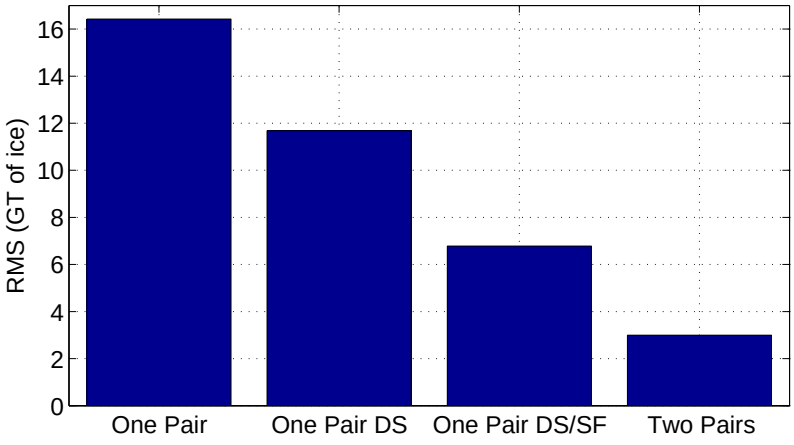

Figure 6.28: RMS of the yearly error RMS values in determining mass variations in the 12 Greenland basins. Units are in GT of ice.

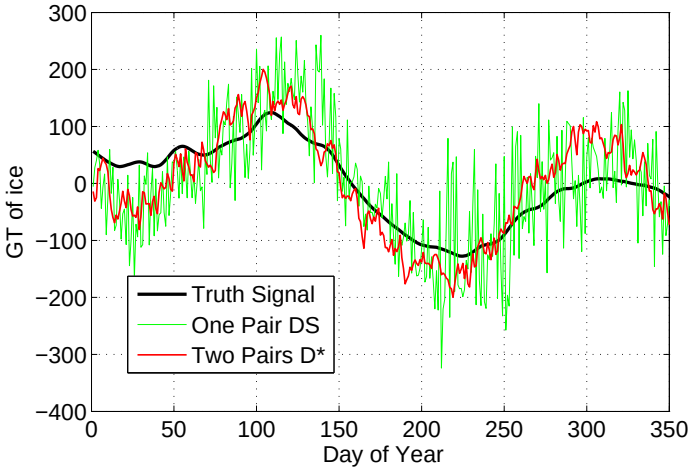

Figure 6.29: Mass variations calculated in Antarctica over the year for one pair of satellites DS, and for two pairs of satellites D*.

6.6.3 Ocean Bottom Pressure Signals

Ocean bottom pressure (OBP) signals are, on average, much larger in spatial scale and smaller in magnitude than hydrology or ice signals. The smaller magnitude of the signals indicates that OBP signals will have a smaller SNR when recovering them than hydrology and ice mass variations, making them more difficult to detect. As a result of this, OBP signals have been more difficult to quantify using GRACE, and regional analyses of the data have been limited to a handful of studies.

In this analysis, we use spatiospectral localization to analyze OBP signals in the Southeast Pacific Basin. This particular basin is of interest due to high variability in the OBP signals, primarily due to topographically trapped signals. Figure 6.30 illustrates the dipole signal in the Southeast Pacific Basin via spatiospectral localization using a spherical cap radius of $\theta_o = 25°$ and maximum degree of expansion $L_h = 15$. Shown are the 13-day average of the truth signal (top-left), and the 13-day averages of the recovered signal using two satellite pairs (top-right), one pair (bottom-left), and one pair destriped and smoothed (bottom-right), expressed in cm of EWH.

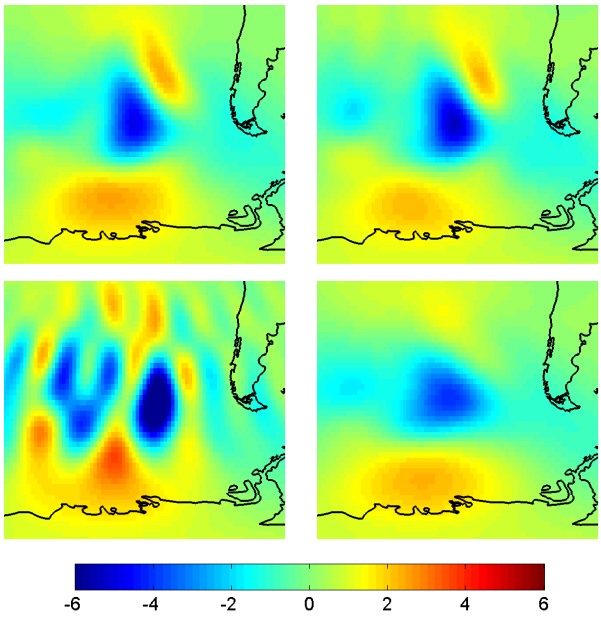

Figure 6.30: Spatiospectral localization technique applied to the Southeast Pacific Basin using $\theta_o = 25°$, $L_h = 15$. Truth signal (top-left) along with the recovered signals from: two pairs of satellites (top-right), one pair of satellites (bottom-left), and one pair of satellites DS (bottom-right) averaged over 13 days. Units are in cm of EWH.

Figure 6.30 shows that two pairs of satellites recover this signal particularly well. The signal is not discernible with one pair of satellites and no post-processing. Once the solutions are destriped and smoothed, the negative part of the dipole signal is present, although distorted spatially, while the positive part is faintly present in the solution. Figure 6.31 illustrates the signal to noise ratio as a function of spherical harmonic degree of the three cases. The solution obtained with two pairs of satellites have a positive SNR out to approximately degree 35, while the destriped and

smoothed solution using one pair of satellites has information until approximately degree 25 or so. This represents an improvement in spatial resolution from 800 km to 571 km in determining this particular signal.

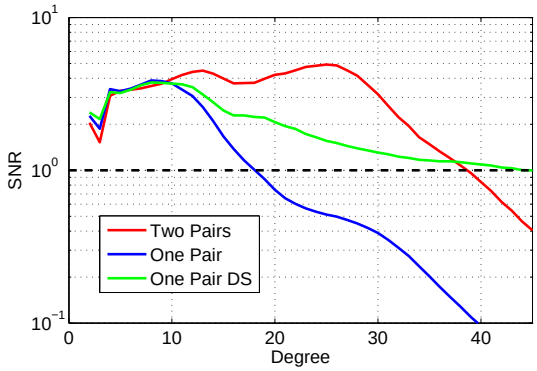

Figure 6.31: Signal to noise ratio for OBP signals in the Southeast Pacific Basin computed using spatiospectral localization (see Figure 6.30).

Finally, we analyze mass variations over the year in this basin (boundaries given by 90°-140° W, 35°-55° S, as defined by *Boening et al.* [2011]) using an averaging kernel. Figure 6.32 shows the ability of each architecture to recover OBP variations in the Southeast Pacific Basin. Figure 6.32 shows excellent agreement between the truth signal and the recovered signal using two pairs of satellites, particularly during times of high variability. The RMS of the error is decreased by 72%, from 1.25 cm to 0.36 cm, with the addition of the second pair of satellites. One pair of satellites fails to capture much of the high frequency variability in OBP in this region.

6.6.4 Earthquakes

GRACE has been used effectively to determine coseismic and postseismic gravity deformations due to large earthquakes, in particular the 2004 Sumatra-Andaman earthquake [*Chen et al.*, 2007; *Panet et al.*, 2007; *Han and Simons*, 2008] and the 2010 Maule, Chile earthquake [*Han et al.*, 2010; *Heki and Matsuo*, 2010]. It is our goal to quantify the expected performance that two satellite pairs offers in determining mass changes due to the coseismic part of the earthquake signal via spatiospectral localization. To perform this simulation, we use an earthquake model representative

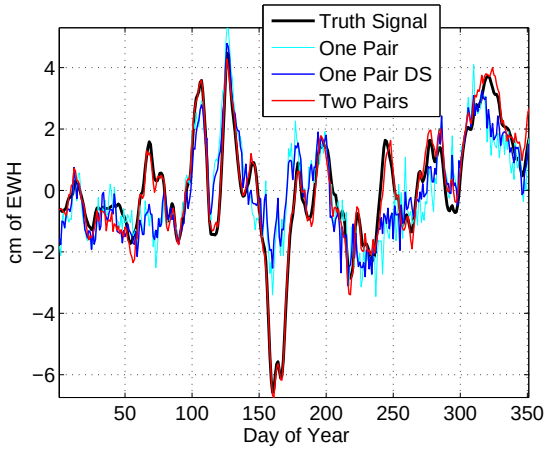

Figure 6.32: Mass variations in the Southeast Pacific Ocean over the year showing the calculated mass from one pair of satellites, one pair DS, and two pairs of satellites.

of the magnitude 8.8 2010 Maule, Chile earthquake (available from the U.S. Geological Survey, http://earthquake.usgs.gov). This model is introduced in the *truth* set of models as a step function that is added to the static gravity field model, EIGEN-GL04C, and is then recovered in addition to the hydrology and ice signals. We apply an optimal windowing function with $\theta_o = 25°$ and $L_h = 15$ to analyze the signal. Figure 6.33 shows the modelled earthquake signal (top-left), the recovered signal using two satellite pairs (top-right), the recovered signal using one pair of satellites (bottom-left), and the recovered signal if the single satellite pair solution is destriped and smoothed (bottom-right). The plots are expressed in cm of EWH. It should be noted that the positive mass anomaly in the upper-right part of the truth signal is actually a hydrology signal in the Paraná Basin that has been captured by the windowing function that is applied. It could be removed via forward modelling to isolate the earthquake signal, but this was deemed unnecessary for the purposes of this study. Figure 6.34 illustrates the localized SNR associated with the recovered earthquake signal.

It is seen that while two pairs of satellites do an exceptional job of recovering the signal with a high SNR out to degree 45, one pair of satellites is also capable of recovering the signal, although with a lower SNR, particularly at low degrees. It is expected that two pairs of satellites will be able to recover earthquakes lower in magnitude than what one pair of satellites can recover.

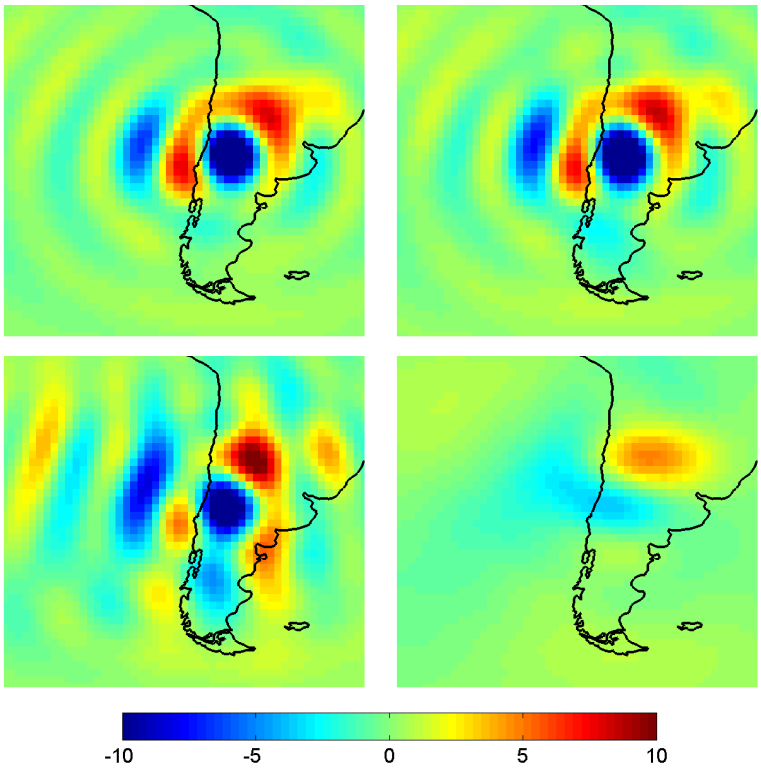

Figure 6.33: Spatiospectral localization technique applied to recover a simulated signal similar to the 2010 Maule, Chile earthquake, using $\theta = 25°$, $L_h = 15$. Truth signal (top-left) along with the recovered signals from: two pairs of satellites (top-right), one pair of satellites (bottom-left), and one pair of satellites DS (bottom-right) averaged over 13 days. Units are in cm of EWH.

Figure 6.34: Localized SNR for recovering the simulated 2010 Maule, Chile earthquake

The threshold of recovery will depend on the location of the earthquake, the magnitude of the earthquake, as well as the type of earthquake. An extensive set of simulations varying the size, strength, and type of earthquake is necessary to characterize a detection threshold that two pairs of satellites offer over one pair. This analysis is not presented here; however, we have shown that large earthquakes, such as the 2010 Maule, Chile earthquake can be detected with much greater accuracy using two pairs of satellites over one pair of satellites.

6.7 A More Realistic Scenario: Higher Altitude and Measurement Noise

The work put forth in this dissertation has assumed the next generation of dedicated missions to measure the gravity field will fly drag-free and utilize laser interferometry for inter-satellite ranging. Additionally, it assumes that an appropriate operating altitude for such a mission will be around 300 km. These assumptions undoubtedly lead to improved results over what GRACE provides, which operates with less precise instruments and at a higher altitude. At the time of publication, it is expected that the gap-filler mission to replace GRACE (estimated launch date in 2016) will simply be a reflight of GRACE at the same altitude and with the same instruments (accelerometers for removal of non-conservative forces and a K-band microwave ranging system for inter-satellite ranging), only with a laser interferometer onboard as a technology demonstration. Given this plausible scenario, the question arises as to how much benefit the addition of a second pair of satellites would provide to a mission at a higher altitude and with larger measurement system errors. This section of text attempts to address this question.

It is expected that the gap-filler mission will fly accelerometers similar in performance to those on GRACE. The accelerometer noise can be modelled as (*Bill Folkner, private communicate, 2011*)

$$ACC_{noise} = 0.1 \times \sqrt{1 + \frac{.005}{f}} \frac{nm}{s^2\sqrt{Hz}}, \tag{6.1}$$

with f being the frequency. Furthermore, a realistic level of noise for the laser interferometer being

considered for the mission is given by (*Bill Folkner, private communicate, 2011*)

$$LAS_{noise} = \begin{cases} 50\frac{nm}{\sqrt{Hz}} \times NSF & 0.2 \text{ mHz} < f < 100 \text{ mHz} \\ 50\frac{nm}{\sqrt{Hz}} & \text{all other } f \end{cases} \tag{6.2}$$

with

$$NSF = \sqrt{1 + \left(\frac{f}{2 \text{ mHz}}\right)^{-2}} \times \sqrt{1 + \left(\frac{f}{10 \text{ mHz}}\right)^{-2}} \tag{6.3}$$

With these levels of errors, the accelerometer noise is the limiting source of error for the mission.

We assume that the altitude of the gap-filler mission will be similar to GRACE, and will be around 500 km or slightly lower. Selecting appropriate values for the repeat period of the satellite orbits as well as the inclination of the lower inclined pair is done by taking into consideration the results from Chapter 5. As such, for the case of one satellite pair, we select a polar pair of satellites at an altitude of 501 km in a 13-day repeating groundtrack. For the case of two satellite pairs, we add a lower inclined pair of satellites to the one-pair architecture that is inclined at 72°, in a 13-day repeat period, and at an altitude of 473 km. Note that the two-pair architecture has a complementary groundtrack pattern, as discussed in Chapter 5. For these simulations, we use the simulation definition given in Table 3.1. Additionally, we estimate daily 18x18 gravity fields for the case of two satellite pairs. Estimating the daily gravity fields provides much smaller benefits at the higher altitude, as was discussed in Chapter 4, so this process could be eliminated entirely if desired.

Figure 6.35 shows the errors in the spherical harmonic coefficients from the one-pair (left) and two-pair architectures (right) from a simulation designed to recover hydrology and ice mass variations. The plots on the top are the errors given the case of having measurement system errors as defined in Equations 6.1 and 6.2. The plots on the bottom show the error from a simulation (with the same orbits) using noise levels previously described in this dissertation assuming drag-free operation and laser interferometry for inter-satellite ranging (see Section 3.2), and were included to discriminate between the impact of raising the altitude of the satellites versus having less precise measurements.

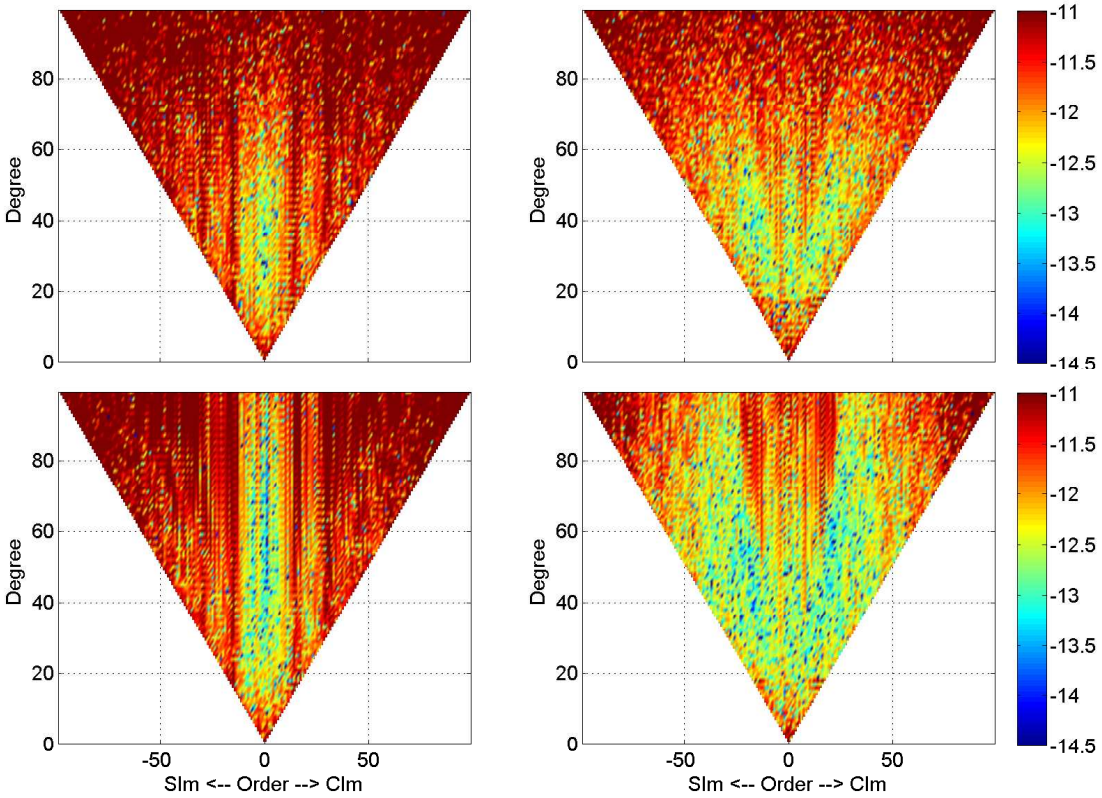

Figure 6.35: Logarithm of the error in the spherical harmonic coefficients from recovering hydrology and ice mass variations while using measurement system errors given by Equations 6.1 and 6.2 (top), and for using measurement system errors as described in Section 3.2 (bottom). The plots on the left are the results from the one-pair simulations while the plots on the right are the results from the two-pair simulations.

Figure 6.35 shows much larger errors for all cases than those seen previously in this dissertation (see Figure 6.2). For the case of higher measurement system errors, the two-pair architecture offers slightly lower errors in the low degree coefficients than the one-pair architecture. When lower measurement noise is considered, the two-pair architecture is shown to have considerably lower errors than the one-pair architecture. This indicates that measurement system errors are the limiting source of error for this case, as the error spectrum can be lowered simply by improving the accuracy of the measurements.

Figure 6.36 shows the geoid height error from each architecture in recovering hydrology and ice mass variations. For reference, an error curve from the current GRACE mission is shown. This curve was obtained by running a simulation with one pair of satellites in a near-polar orbit in a

30-day repeating groundtrack separated by 220 km at an altitude of 475 km with measurement noise levels commensurate with that of GRACE. The plot on the left is the error from a simulation with noise levels outlined in Equations 6.1 and 6.2 (higher measurement system errors), while the plot on the right is the error from a simulation using noise levels as previously described in this dissertation (see Section 3.2; lower measurement system errors).

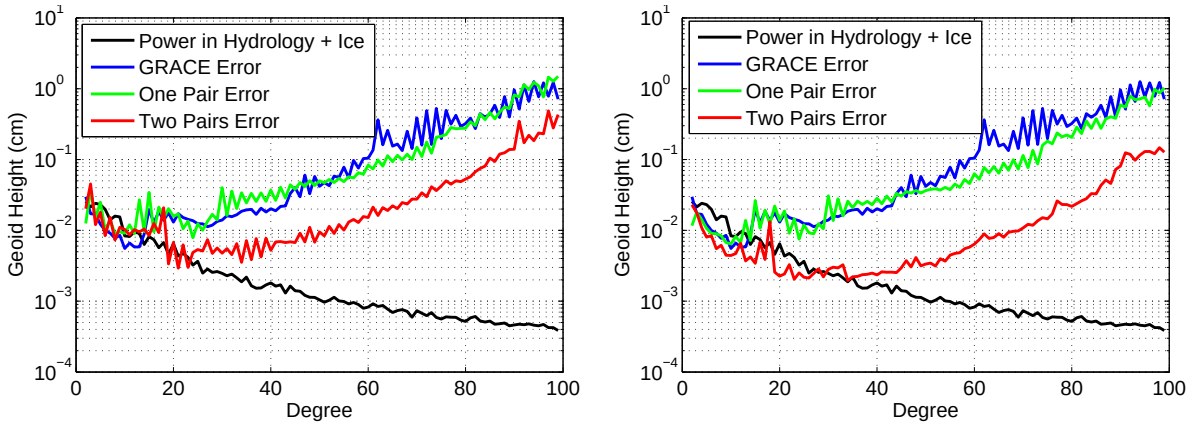

Figure 6.36: Geoid height error as a function of degree from recovering hydrology and ice mass variations while using measurement system errors given by Equations 6.1 and 6.2 (left), and for using measurement system errors as described in Section 3.2 (right)

Figure 6.36 shows there are minimal differences (for both levels of measurement noise) between the case of GRACE and the case of one satellite pair. This comparison more or less shows that one can do equally well accumulating measurements for 13 days as what can be accomplished with accumulating measurements for 30 days. Since the spacecraft are not flying drag-free for the case of higher measurement noise, however, this repeat groundtrack would be difficult to maintain. As such, homogeneous spacing over 13 days could not be guaranteed, meaning one would likely need to accumulate measurements for 30 days prior to forming a gravity solution, similar to the operations of the current GRACE missions. Both cases show the improvement that two satellite pairs offers over one satellite pair. It is seen that with the higher precision measurements, two pairs of satellites offer a greater improvement in performance, indicating that measurement errors are limiting the mission performance at this point rather than the altitude or temporal aliasing errors. It is seen that one can recover hydrology and ice signals out to approximately degree 30 with

the higher measurement precision, while signals can only realistically be recovered out to degree 10-20 with the lower precision in measurements. In fact, it appears that the for the case of higher measurement system errors, two pairs of satellites does not offer much improvement over what one pair of satellites offers.

To examine this more thoroughly, Figure 6.37 shows the recovered signals spatially represented to degree 60 for the case with higher measurement system errors. Figure 6.38 shows the equivalent plot, only with lower measurement system errors. The top plot is the truth hydrology signal, while the middle row shows the recovered signals from one pair of satellites (left) and two pairs of satellites (right). The bottom row of plots are the same results after the solutions have been destriped and smoothed with a 300 km Gaussian averaging radius.

Figure 6.37 shows that with no post-processing, the two-pair solution has lower errors than the one-pair solution. However, the solutions are quite noisy, and require destriping and smoothing. After post-processing, the two-pair solution is seen to have slightly lower errors; it can be assumed that a slightly smaller averaging radius could be used with these solutions versus the one-pair solutions, resulting in a small improvement in spatial resolution. Rather than truncating the solutions at degree 60 for this analysis, we could have truncated at a lower degree in hopes of improving the two-pair solutions to such a level that they do not require post-processing. This was attempted; however, it was found that post-processed degree 60 solutions offer better spatial resolution than truncated solutions (at lower degrees) that do not require post-processing.

Alternately, for the case of lower measurement noise (given by that described in Section 3.2), Figure 6.38 shows the two-pair solution has much smaller errors, however still large enough to merit the destriping and smoothing processes due to errors at high degree coefficients. While Figure 6.38 represents the signals to degree 60, it was found that the two-pair solutions could be truncated at degree 40 without the need for post-processing. The spatial resolution of the solutions truncated at degree 40 is superior to solutions that have been truncated at higher degrees and post-processed. Figure 6.39 illustrates this fact, showing the truth (left) and recovered signal (right) using two satellites pairs (and lower measurement system errors) truncated at degree 40.

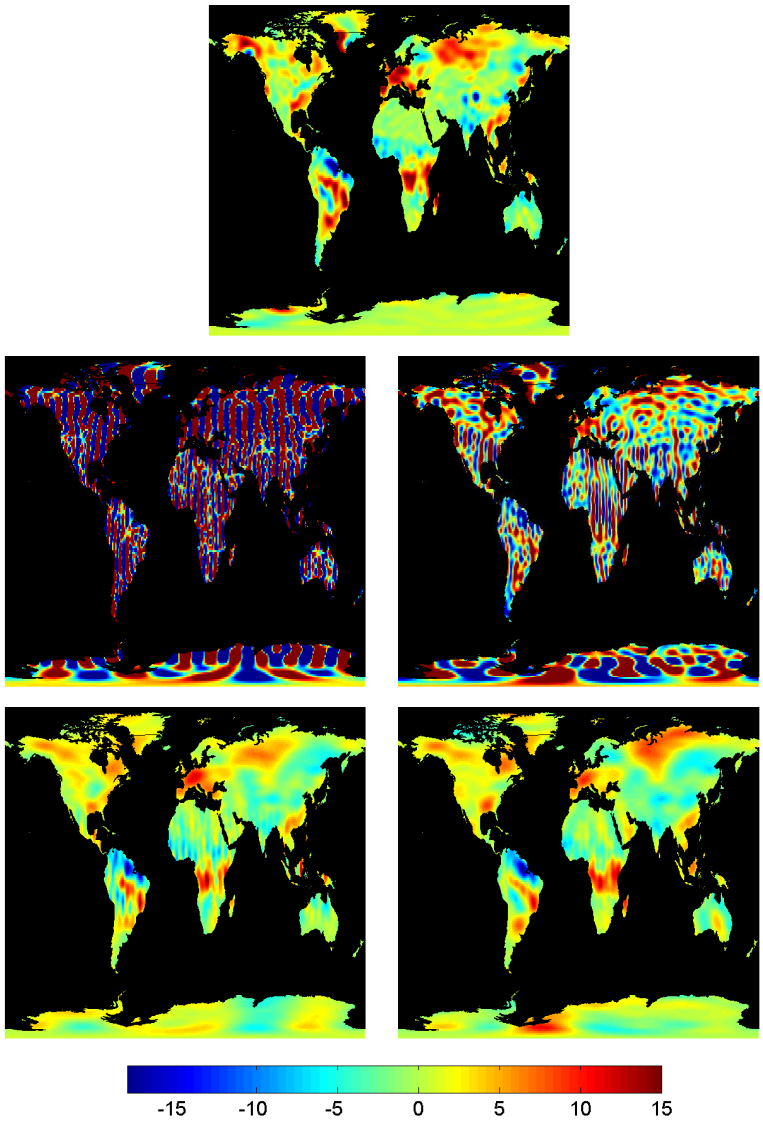

Figure 6.37: The top plot shows the truth hydrology and ice signals averaged over 13 days. The middle row shows the recovered signals for: one pair of satellites (left) and two pairs of satellites (right) with higher measurement system errors. The bottom row shows the same recovered signals, only after the solutions have been destriped and smoothed with a 300 km averaging radius. Units are in cm of EWH.

As such, one can conclude from this section that there would be minimal scientific benefits in adding a second pair of satellites if the satellites were flown at a higher altitude with measurement noise levels commensurate with those described by Equations 6.1 and 6.2. Should the measurement noise be improved to such a level as that described in Section 3.2, then the scientific benefits of

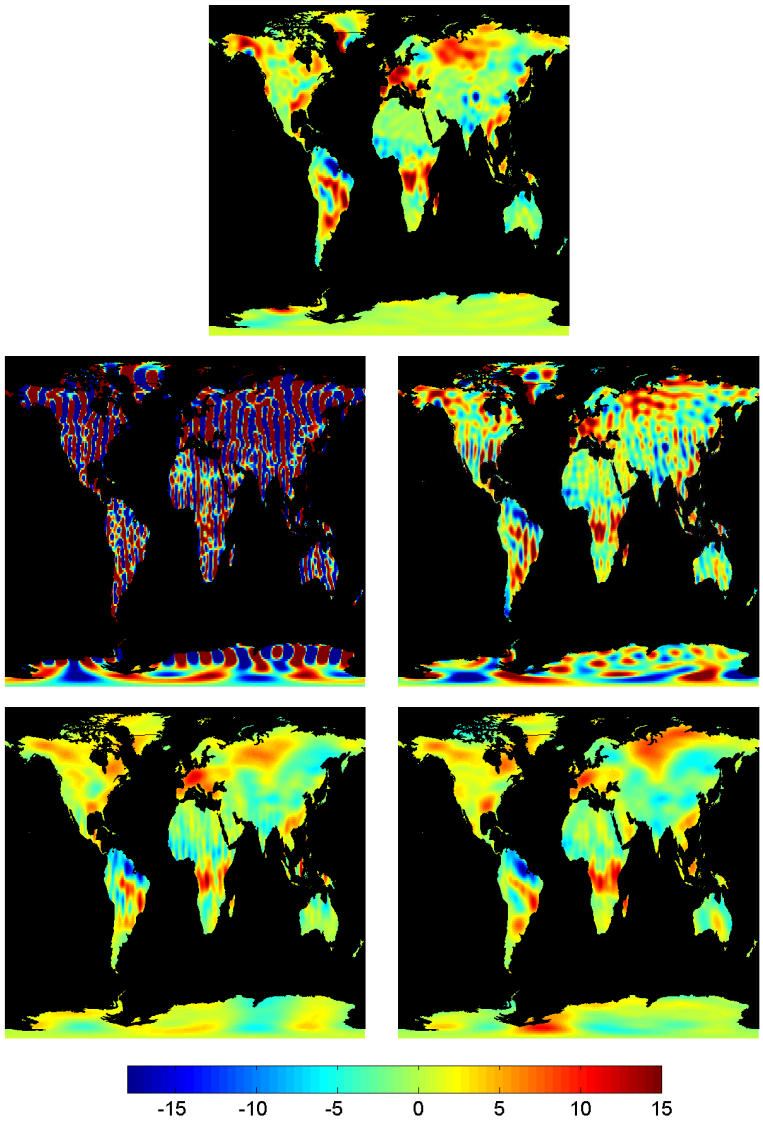

Figure 6.38: The top plot shows the truth hydrology and ice signals averaged over 13 days. The middle row shows the recovered signals for: one pair of satellites (left) and two pairs of satellites (right) with lower measurement system errors. The bottom row shows the same recovered signals, only after the solutions have been destriped and smoothed with a 300 km averaging radius. Units are in cm of EWH.

having two pairs of satellites improve substantially, and continues improving as the altitude of the satellites is lowered.

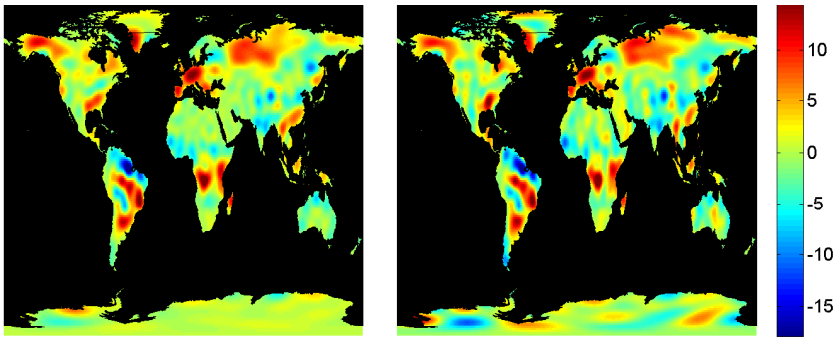

Figure 6.39: Truth hydrology and ice signals (left) and recovered signals (right) using two satellite pairs with lower measurement system errors truncated at degree 40. Units are in cm of EWH.

6.8 Conclusions

This chapter examines the expected performance for one pair of satellites, two polar pairs of satellites, and a polar pair coupled with a lower inclined pair of satellites. It was shown that the addition of a second polar pair of satellites does nothing to reduce correlations between coefficients of the same order and same parity of degree. As such, longitudinal stripes still persist in the solutions, and standard GRACE post-processing techniques are necessary. Once the solutions are post-processed, the mass variations are nearly identical to the post-processed solutions obtained using only a single pair of satellites. This indicates minimal, if any, improved performance in determining mass variations with the addition of a second polar pair of satellites. Alternately, we see with the addition of an optimally selected lower inclined pair of satellites (Case 13 in Table 5.5), correlations between coefficients decrease, as do the formal and actual errors. The magnitude of longitudinal stripes (for degrees up to 60) are small in comparison to the magnitude of hydrology and ice signals. As such, solutions do not necessitate post-processing, and much more spatial information is retained.

An EOF analysis reveals that two satellite pairs (one polar and one lower inclined) detects annual variations in small river basins which are undetected using one pair of satellites. Averaging kernels are used to analyze 53 hydrological basins across the globe as well as 12 basins in Greenland. On average, when no post-processing is applied to the gravity solutions, two pairs of satellites offer

an 80% reduction in error in determining mass variations in the basins over the year. After the single satellite pair solutions have been destriped, smoothed, and mass has been restored using an appropriate scale factor, two pairs of satellites (with no post-processing) still, on average, provide a 25%-40% reduction in errors in determining mass variations in the hydrological basins and a 55%-75% reduction in errors in determining mass variations in the Greenland basins over the year. Spatiospectral localization analysis is used to analyze ocean bottom pressure signals in the Southeast Pacific Basin as well as a simulated earthquake signal similar to the 2010 Maule, Chile earthquake. Two pairs of satellites improve the spatial resolution in determining the ocean bottom pressure signal from 800 km to 570 km, and determines the total mass in the basin over the year with 70% more accuracy than one satellite pair. While the earthquake signal is detected using both architectures, two pairs of satellites increase the signal to noise ratio at higher degrees by approximately one-half of an order of magnitude. It is expected that the addition of a second pair of satellites will also allow for earthquakes smaller in magnitude to be quantified which otherwise would be undetected with gravity measurements.

Perhaps the largest advantage of adding a second pair of satellites is that the solutions do not necessitate ad hoc GRACE post-processing procedures when studying signals to spatial resolution of $\sim$ 330 km. This eliminates much of the confusion as to what the destriping and smoothing algorithms do to geophysical signals. Additionally, one does not need to worry about applying incorrect scale factors to the solutions when trying to restore mass that the destriping and smoothing processes have removed. The results presented here are regarded to be relatively pessimistic for the case of two pairs of satellites. It is expected that optimized post-processing techniques will be developed for such an architecture which would increase the spatial resolution in the solutions even further. This, in turn, would allow for mass variations to be determined in smaller river basins than those analyzed in this study.

Chapter 7

Conclusions and Recommendations

7.1 Conclusions

It is expected that future missions dedicated to recovering temporal gravity variations will take advantage of improvements in technology by flying drag-free and using a laser interferometer for inter-satellite ranging. With these improved measurement types, studies have shown that the limiting source of error for such a mission will be due to undersampling signals of interest and mis-modelling unwanted geophysical signals (i.e. temporal aliasing errors). The focus of this dissertation has been on the reduction of temporal aliasing errors through the addition of an optimally-placed second pair of satellites, as well as directly estimating high frequency gravity field variations.

Chapter 4 explored the option of estimating high frequency/low resolution gravity fields to directly reduce temporal aliasing errors. This was performed for the case of a single polar pair of satellites, two polar pairs of satellites, and a polar pair of satellites coupled with a lower inclined pair of satellites. We found that for the case of a single pair of satellites, estimating 2-day 10x10 gravity fields provides some reduction in the level of error. However, in this scenario, the quality of the estimates varies due to the variability in the groundtrack spacing over two days. On the contrary, for the cases involving two pairs of satellites, it was shown that estimating daily 18x18 gravity fields is optimal, providing the most reduction in temporal aliasing errors. The absolute lowest level of errors is given by the case of having a polar pair coupled with a lower inclined pair. Estimating daily 18x18 gravity fields reduces the level of error in these solutions by approximately 33%.

Chapter 5 optimized the orbits of two satellite pairs for recovering temporal gravity variations. Given the scenario of having two dedicated pairs of satellites for temporal gravity recovery, the search space for finding an optimal set of orbital parameters is infinite; and, in a large part depends on the scientific objectives of the mission as well as mission constraints, such as required mission lifetime and fuel availability, which directly affects the choice of orbital altitude. We assume the scientific objectives of the mission are to determine hydrology, ice mass variations, and ocean bottom pressure signals with as high spatial resolution as possible (with each area of science being weighted equally). Additionally, we set a minimum allowable altitude of 290 km based on a projected 10-year mission lifetime. Using a Monte-Carlo analysis and numerical simulations extended to degree and order 100, a search space originally consisting of fifteen variables (the position and velocity of the lead spacecraft of each pair, the separation distance between the satellite pairs, and the length of time data are collected) is reduced to two variables with primary impact on mission performance: the inclination of one of the satellite pairs (the other pair is assumed to be polar), and the repeat periods of both pairs of satellites (shown to be near-optimal when they are equal to each other). This analysis assumes a 100 km inter-satellite separation distance, and circular orbits in repeating groundtracks. It is found that an optimal value for the inclination of the second pair of satellites is between 70^o and 75^o, while an appropriate range for the repeat periods of both satellite pairs is between 11 and 14 days. The notion of optimizing the relative differences in the longitude of ascending node and the argument of latitude between the two pairs was also discussed in relation to creating complementary groundtrack patterns. It is shown that by raising the altitude of the polar pair, the nodal drift rate of the lower inclined pair can be compensated for such that a groundtrack pattern with crossings at constant lines of latitude is created. While numerical simulation results imposing this constraint are not conclusive as to whether this definitively results in improved mission performance, there is an argument for having a geometry that permits consistent global mapping of the gravity field. As such, we choose an 'optimized' two-pair mission architecture to consist of a polar pair of satellites at 290 km coupled with a lower inclined pair of satellites (72°) at 320 km, both in 13-day repeating orbits, and having a complementary groundtrack pattern with

crossings at constant lines of latitude.

Chapter 6 discussed the expected improvements in performance that an optimized two-pair architecture provides over one pair of satellites. Results are analyzed both globally and regionally. An EOF analysis reveals that two satellite pairs detect mass variations in small river basins which are undetected using one pair of satellites. Global analysis of results are insufficient by themselves, however, as the ability to recover mass variations in a particular region depend on the size of the signal and error, the geographic location, and the space-time sampling characteristics of the satellites. As such, the best one can hope to do to characterize mission performance is to perform realistic numerical simulations to recover mass variations in a variety of regions. Averaging kernels are used to analyze 53 hydrological basins across the globe as well as 12 basins in Greenland. On average, when no post-processing is applied to the gravity solutions, two pairs of satellites offer an 80% reduction in error in determining mass variations in the basins over the year. After the single satellite pair solutions have been destriped, smoothed, and mass has been restored using an appropriate scale factor, two pairs of satellites (with no post-processing) still, on average, provide a 25%-40% reduction in errors in determining mass variations in the hydrological basins and a 55%-75% reduction in errors in determining mass variations in the Greenland basins over the year. Spatiospectral localization analysis is used to analyze ocean bottom pressure signals in the Southeast Pacific Basin as well as a simluated earthquake signal similar to the 2010 Maule, Chile earthquake. Two pairs of satellites improve the spatial resolution in determining the ocean bottom pressure signal from 800 km to 570 km, and determines the total mass in the basin over the year with 70% more accuracy than one satellite pair. While the earthquake signal is detected using both architectures, two pairs of satellites increase the signal to noise ratio at higher degrees by approximately one-half of an order of magnitude. It is expected that the addition of a second pair of satellites will also allow for earthquakes smaller in magnitude to be quantified which otherwise would be undetected with gravity measurements.

Perhaps the largest advantage of adding a second pair of satellites is that the solutions do not necessitate ad hoc GRACE post-processing procedures when studying signals to spatial

resolution of $\sim$ 330 km. This eliminates much of the confusion as to what the destriping and smoothing algorithms do to geophysical signals. Additionally, one does not need to worry about applying incorrect scale factors to the solutions when trying to restore mass that the destriping and smoothing processes have removed. The results in this paper are regarded to be relatively pessimistic for the case of two pairs of satellites. It is expected that optimized post-processing techniques will be developed for such an architecture which would increase the spatial resolution in the solutions even further. This, in turn, would allow for mass variations to be determined in smaller river basins than those analyzed in this study.

The option of having two polar pairs of satellite was also discussed. It was found that while two polar pairs of satellites does provide lower errors than one pair, correlations between coefficients persist, and as such, longitudinal striping dominates the solutions. After the solutions have been destriped and smoothed, there are negligible differences between the solutions obtained from one pair of satellites and two polar pairs of satellites. This indicates minimal, if any, increases in spatial resolution (although the temporal resolution will be increased by a factor of two) simply by adding a second pair of polar orbiting satellites. Finally, it was shown that for a scenario in which the satellites are at higher altitudes and have measurement system errors commensurate with those of the current GRACE mission (as is expected for the 2016 gap-filler mission), minimal scientific benefits are seen by adding an optimally-placed second pair of satellites, as the performance is limited by the measurement system errors.

7.2 Recommendations

If sufficient funds are available in the future to provide two pairs of satellites dedicated to recovering temporal gravity variations (and are flown drag-free with inter-satellite laser ranging), we recommend that one of the pairs be placed in a polar orbit and the other be placed at a moderate inclination, between 70° and 75°. Both satellites should be placed in repeating groundtracks with equivalent repeat periods between 11 and 14 days, and flown at as low of an altitude as possible (300 km has been shown to be sufficient for large scientific benefits). This work has provided the context

to significantly reduce the search space for an optimal architecture based on the specific scientific objectives of the mission as well as mission constraints (such as satellite altitude/mission lifetime), and should be used accordingly. We expect significant scientific benefits given this scenario.

Bibliography

Aguirre-Martinez, M., and N. Sneeuw, Needs and tools for future gravity measuring missions, *Space Science Reviews*, *108*, 409–416, 2002.

Alnis, J., A. Matveev, N. Kolachevsky, T. Udem, and T. W. Hansch, Subhertz linewidth diode lasers by stabilization to vibrationally and thermally compensated ultralow-expansion glass Fabry-Pérot cavities, *Physical Review A*, *77*(5), doi: 10.1103/PhysRevA.77.053,809, 2008.

Bandikova, T., J. Flury, and U.-D. Ko, Impact of spacecraft attitude variations on the grace scientific results, in *Vol. 12, EGU2010-8319-1, EGU General Assembly*, 2010.

Beerer, J. G., and F.-H. Massmann, Status GRACE Mission Operations, in *GRACE Science Team Meeting*, Potsdam, Germany, 2010.

Bender, P., Integrated laser doppler method for measuring planetary gravity fields, in *From Mars to Greenland: Charting Gravity with Space and Airborne Instruments*, edited by O. L. Colombo, pp. 63–72, 1992.

Bender, P. L., J. L. Hall, J. Ye, and W. M. Klipstein, Satellite-satellite laser links for future gravity missions, *Space Science Reviews*, *108*, 377–384, doi: 10.1023/A:1026195913,558, 2003.

Bender, P. L., D. N. Wiese, and R. S. Nerem, A possible dual-GRACE mission with 90 degree and 63 degree inclination orbits, in *Proceedings of the Third International Symposium on Formation Flying, Missions and Technologies*, pp. 1–6, ESA/ESTEC, Noordwijk, The Netherlands, 2008.

Boening, C., T. Lee, and V. Zlotnicki, A record-high ocean bottom pressure in the South Pacific observed by GRACE, *Geophysical Research Letters*, *38*(L04602), doi: 10.1029/2010GL046,013, 2011.

Bonin, J. A., Improving the observation of time-variable gravity using grace rl04 data, Ph.D. thesis, University of Texas at Austin, 2010.

Brouwer, D., Solution of the problem of artificial satellite theory without drag, *Astronaut Journal*, *64*, 378–397, 1959.

Bruinsma, S., J.-M. Lemoine, R. Biancale, and N. Vales, CNES/GRGS 10-day gravity field models (release 2) and their evaluation, *Advances in Space Research*, *45*, 587–601, doi: 10.1016/j.asr.2009.10.012, 2010.

Carrère, L., and F. Lyard, Modeling the barotropic response of the global ocean to atmospheric wind and pressure forcing, *Geophysical Research Letters*, *30*(6), 1275, 2003.

Chambers, D. P., Evaluation of new GRACE time-variable gravity data over the ocean, *Geophysical Research Letters*, *33*, L17,603, doi: 10.1029/2006GL027,296, 2006.

Chambers, D. P., and J. K. Willis, A Global Evaluation of Ocean Bottom Pressure from GRACE, OMCT, and Steric-Corrected Altimetry, *Journal of Atmospheric and Oceanic Technology*, *27*(8), 1395–1402, 2010.

Chen, J. L., C. R. Wilson, and K. W. Seo, Optimized smoothing of gravity recovery and climate experiment (GRACE) time-variable gravity observations, *Journal of Geophysical Research*, *111*, B06,408, doi: 10.1029/2005JB004,064, 2006.

Chen, J. L., C. R. Wilson, B. D. Tapley, and S. Grand, GRACE detects coseismic and postseismic deformation from the Sumatra-Andaman earthquake, *Geophysical Research Letters*, *34*, L13,302, doi: 10.1029/2007GL030,356, 2007.

Chen, J. L., C. R. Wilson, D. Blankenship, and B. D. Tapley, Accelerated Antarctic ice loss from satellite gravity measurements, *Nature Geoscience*, *2*(12), 859–862, 2009.

Colombo, O., The global mapping of gravity with two satellites, *Tech. Rep. 3*, Netherlands, Geodetic Commission, Publications on Geodesy, New Series, 1984.

Colombo, O. L., and B. F. Chao, Advanced techniques for mapping gravity and its changes from space, in *Proceedings of the International GraGeoMar-97 Symposium on Marine Gravimetry, Marine Surveying, and Navigation, IAG Series*, 1997.

Davis, J. L., M. E. Tamisiea, P. Elósegui, J. X. Mitrovica, and E. M. Hill, A statistical filtering approach for gravity recovery and climate experiment (GRACE) gravity data, *Journal of Geophysical Research*, *113*, B04,410, doi: 10.1029/2007JB005,043, 2008.

Dirac, P. A. M., *The Principles of quantum mechanics, 4th edition*, The international series of monographs on physics 27, Oxford University Press, Oxford, England, 1958.

Dolesi, R., et al., Gravitational sensor for LISA and its technology demonstration mission, *Classical and Quantum Gravity*, *20*(10), S99–S108, 2003.

Drinkwater, M., R. Haagmans, D. Muzzi, A. Popescu, R. Floberghagen, M. Kern, and M. Fehringer, The GOCE gravity mission: ESA's first core explorer, in *Proceedings of the Third GOCE User Workshop*, pp. 1–7, Frascati, Italy, ESA SP-627, 2007.

Duan, X. J., J. Y. Guo, C. K. Shum, and W. van der Wal, On the postprocessing removal of correlated errors in GRACE temporal gravity field solutions, *Journal of Geodesy*, *83*, 1095–1106, doi: 10.1007/s00,190–009–0327–0, 2009.

Dunn, C., et al., Instrument of GRACE: GPS augments gravity measurements, *GPS World*, *14(2)*, 16–28, 2003.

Ebisuzaki, W., A method to estimate the statistical significance of a correlation when the data are serially correlated, *Journal of Climate*, *10*, 2147–2153, 1997.

Elsaka, B., Simulated satellite formation flights for detecting temporal variations of the earth's gravity field, Ph.D. thesis, University of Bonn, 2010.

Encarnacao, J., P. Ditmar, and X. Liu, Analysis of satellite formations in the context of gravity field retrieval, *Proceedings of the 3rd international symposium on formation flying, missions and technologies*, ESA Communication Production Office, ESA SP-654, 2008.

ESA, Gravity Field and Steady-State Ocean Circulation Mission, *Reports for Mission Selection, The Four Candidate Earth Explorer Core Missions, SP-1233(1)*, European Space Agency, 1999.

Fehringer, M., R. Floberghagen, D. Muzi, C. Steiger, and J. Pineiro, GOCE Satellite and Mission Performance, in *Fall AGU Meeting Proceedings*, San Francisco, CA, 2010.

Fengler, M. J., W. Freeden, A. Kohlhaas, V. Michel, and T. Peters, Wavelet modeling of regional and temporal variations of the Earth's gravitational potential observed by GRACE, *Journal of Geodesy*, *81*(1), 5–15, doi: 10.1007/s00,190–006–0040–1, 2007.

Flechtner, F., AOD1b product description document for product releases 01 to 04, *GRACE 327-750 (GR-GFZ-AOD-0001), Rev 3.0*, GeoForschungszentrum Potsdam, Department 1: Geodesy and Remote Sensing, 2007.

Flechtner, F., Introduction, in *GRACE Science Team Meeting*, Potsdam, Germany, 2010.

Förste, C., et al., The GFZ/GRGS satellite and combined gravity field models EIGEN-GL04S1 and EIGEN-GL04C, *Journal of Geodesy*, *82*(6), 331–346, 2008.

Guo, J. Y., X. J. Duan, and C. K. Shum, Non-isotropic Gaussian smoothing and leakage reduction for determining mass changes over land and ocean using GRACE data, *Geophysical Journal International*, *181*, 290–302, doi: 10.1111/j.1365–246X.2010.04,534.x, 2010.

Han, D., and J. Wahr, The viscoelastic relaxation of a realistically stratified Earth, and a further analysis of postglacial rebound, *Geophysical Journal International*, *120*, 287–311, 1995.

Han, S., C. Jekeli, and C. Shum, Time-variable aliasing effects of ocean tides, atmosphere, and continental water mass on monthly mean GRACE gravity field, *Journal of Geophysical Research - Solid Earth*, *109*, B04,403, doi:10.1029/2003JB002,501, 2004.

Han, S.-C., and P. Ditmar, Localized spectral analysis of global satellite gravity fields for recovering time-variable mass redistributions, *Journal of Geodesy*, *82*, 423–430, doi: 10.1007/s00,190–007–0194–5, 2008.

Han, S.-C., and F. J. Simons, Spatiospectral localization of global geopotential fields from the Gravity Recovery and Climate Experiment (GRACE) reveals the coseismic gravity change owing to the 2004 Sumatra-Andaman earthquake, *Journal of Geophysical Research*, *113*, B01,405, doi: 10.1029/2007JB004,927, 2008.

Han, S. C., C. K. Shum, C. Jekeli, C. Y. Kuo, C. R. Wilson, and K. W. Seo, Non-isotropic filtering of GRACE temporal gravity for geophysical signal enhancement, *Geophysical Journal International*, *163*, 18–25, doi: 10.1111/j.1365–246X.2005.02,756.x, 2005.

Han, S. C., J. Sauber, and S. Luthcke, Regional gravity decrease after the 2010 Maule (Chile) earthquake indicates large-scale mass redistribution, *Geophysical Research Letters*, *37*, L23,307, doi: 10.1029/2010GL045,449, 2010.

Heki, K., and K. Matsuo, Coseismic gravity changes of the 2010 earthquake in central Chile from satellite gravimetry, *Geophysical Research Letters*, *37*, L24,306, doi: 10.1029/2010GL045,335, 2010.

Horwath, M., J. M. Lemoine, R. Biancale, and S. Bourgogne, Improved GRACE science results after adjustment of geometric biases in the Level-1B K-band ranging data, *Journal of Geodesy*, *85*, 23–38, doi: 10.1007/s00,190–010–0414–2, 2011.

Jekeli, C., Alternative methods to smooth the earth's gravity field, *Department of geodetic science, report no. 327*, The Ohio State University, 1981.

Kalnay, E., et al., The NCEP/NCAR 40-year reanalysis project, *Bulletin of the American Meteorological Society*, *77*, 437–470, 1996.

Kaula, W. M., *Theory of Satellite Geodesy*, Blaisdell Publishing Company, Waltham, Massachusetts, 1966.

Kim, J.-R., Simulation study of a low-low satellite-to-satellite tracking mission, Ph.D. thesis, University of Texas at Austin, 2000.

Klees, R., E. A. Revtova, B. C. Gunter, P. Ditmar, E. Oudman, H. C. Winsemius, and H. H. G. Savenije, The design of an optimal filter for monthly GRACE gravity models, *Geophysical Journal International*, *175*, 417–432, doi: 10.1111/j.1365–246X.2008.03,922.x, 2008.

Klokocnik, J., C. A. Wagner, J. Kostelecky, A. Bezdek, P. Novak, and D. McAdoo, Variations in the accuracy of gravity recovery due to ground track variability: GRACE, CHAMP, and GOCE, *Journal of Geodesy*, *82*, 917–927, 2008.

Koop, R., and R. Rummel, The future of satellite gravimetry, *Report from the workshop on the future of satellite gravimetry*, ESTEC, Noordwijk, The Netherlands, 2007.

Kurtenbach, E., T. Mayer-Gürr, and A. Eicker, Deriving daily snapshots of the Earth's gravity field from GRACE L1B data using Kalman filtering, *Geophysical Research Letters*, *36*, L17,102, doi: 10.1029/2009GL039,564, 2009.

Kusche, J., Approximate decorrelation and non-isotropic smoothing of time-variable GRACE-type gravity field models, *Journal of Geodesy*, *81*, 733–749, doi: 10.1007/s00,190–007–0143–3, 2007.

Lemoine, F. G., et al., The development of the joint NASA GSFC and NIMA geopotential model EGM96, *NASA/TP-1998-206861*, NASA Goddard Space Flight Center, 1998.

Leuliette, E. W., and L. Miller, Closing the sea level rise budget with altimetry, Argo, and GRACE, *Geophysical Research Letters*, *36*, 2009.

Loomis, B., Simulation study of a follow-on gravity mission to GRACE, Ph.D. thesis, University of Colorado at Boulder, 2009.

Loomis, B. D., R. S. Nerem, and S. B. Luthcke, Simulation study of a follow-on gravity mission to GRACE, *Submitted to Journal of Geodesy*, 2010.

Luthcke, S. B., H. J. Zwally, W. Abdalati, D. D. Rowlands, R. D. Ray, R. S. Nerem, F. G. Lemoine, J. J. McCarthy, and D. S. Chinn, Recent Greenland ice mass loss by drainage system from satellite gravity observations, *Science*, *314*(5803), 1286–1289, 2006.

Luthcke, S. B., A. A. Arendt, D. D. Rowlands, J. J. McCarthy, and C. F. Larsen, Recent glacier mass changes in the Gulf of Alaska region from GRACE mascon solutions, *Journal of Glaciology*, *54*(188), 767–777, 2008.

Lyard, F., F. Lefevre, T. Letellier, and O. Francis, Modelling the global ocean tides: modern insights from FES2004, *Ocean Dynamics*, *56*, 394–415, 2006.

Marchetti, P., J. J. Blandino, and M. A. Demetriou, Electric propulsion and controller design for drag-free spacecraft operation, *Journal of Spacecraft and Rockets*, *44*(6), 1303–1315, doi: 10.2514/1.36,307, 2008.

Moore, P., Q. Zhang, and A. Alothman, Annual and semiannual variations of the Earth's gravitational field from satellite laser ranging and CHAMP, *Journal of Geophysical Research*, *110*, B06,401, doi: 10.1029/2004JB003,448, 2005.

Mueller, G., I. Thorpe, P. Mcnamara, and J. Camp, Laser frequency stabilization for LISA, *NASA/TM-2005-212794*, NASA Goddard Space Flight Center, December 2005.

Nerem, R. S., C. Jekeli, and W. M. Kaula, Gravity field determination and characteristics: Retrospective and prospective, *Geophysical Research Letters*, *100*, 15,053–15,074, 1995.

Panet, I., V. Mikhailov, M. Diament, F. Pollitz, G. King, O. de Viron, M. Holschneider, R. Biancale, and J. M. Lemoine, Coseismic and post-seismic signatures of the Sumatra 2004 December and 2005 March earthquakes in GRACE satellite gravity, *Geophysical Journal International*, *171*(1), 177–190, doi: 10.1111/j.1365–246X.2007.03,525.x, 2007.

Pavlis, D. E., C. Deng, and J. J. McCarthy, GEODYN operations manual, *Contractor report*, SGT, Inc., Greenbelt, MD, 2010.

Pierce, R., J. Leitch, M. Stephens, P. Bender, and R. Nerem, Inter-satellite range monitoring using optical interferometry, *Applied Optics*, *47*, 5007–5019, doi: 10.1364/AO.47.005,007, 2008.

Preisendorfer, R. W., *Principal Component Analysis in Meteorology and Oceanography*, Elsevier, Seattle, Washington, 1988.

Ray, R. D., A global ocean tide model from TOPEX/POSEIDON altimetry: GOT99.2, *NASA technical memorandum 209478*, Goddard Space Flight Center, 1999.

Ray, R. D., and S. B. Luthcke, Tide model errors and GRACE gravimetry: towards a more realistic assessment, *Geophysical Journal International*, *167*, 1055–1059, doi:10.1111/j.1365–246X.2006.03,229.x, 2006.

Reubelt, T., N. Sneeuw, and M. Sharifi, Future mission design options for spatio-temporal geopotential recovery, in *Proceedings of Gravity, Geoid, and Earth Observation*, Chania, Crete, Greece, June 23-27, 2008.

Rodell, M., J. Chen, H. Kato, J. S. Famigleietti, J. Nigro, and C. R. Wilson, Estimating groundwater storage changes in the Mississippi River Basin (USA) using GRACE, *Hydrogeology Journal*, *15*, 159–166, 2007.

Rodell, M., et al., The Global Land Data Assimilation System, *Bulletin of the American Meteorological Society*, *85*, 381–394, 2004.

Rodell, M., I. Velicogna, and J. S. Famiglietti, Satellite-based estimates of groundwater depletion in India, *Nature*, *460*(7258), 999–U80, 2009.

Rosborough, G. W., and B. D. Tapley, Radial, Transverse, and Normal Satellite Position Perturbations due to the Geopotential, *Celestial Mechanics*, *40*, 409–421, 1987.

Rowlands, D. D., R. D. Ray, D. S. Chinn, and F. G. Lemoine, Short-arc analysis of intersatellite tracking data in a gravity mapping mission, *Journal of Geodesy*, *76*, 307–316, doi: 10.1007/s00,190–002–0255–8, 2002.

Rowlands, D. D., S. B. Luthcke, J. J. McCarthy, S. M. Klosko, D. S. Chinn, F. G. Lemoine, J. P. Boy, and T. J. Sabaka, Global mass flux solutions from GRACE: A comparison of parameter estimation strategies - Mass concentrations versus Stokes coefficients, *Journal of Geophysical Research*, *115*(B01403), doi: 10.1029/2009JB006,546, 2010.

Sabaka, T. J., D. D. Rowlands, S. B. Luthcke, , and J. B. Boy, Improving global mass flux solutions from Gravity Recovery and Climate Experiment (GRACE) through forward modeling and continuous time correlation, *Journal of Geophysical Research*, *115*, B11,403, doi: 10.1029/2010JB007,533, 2010.

Save, H. V., Using regularization for error reduction in grace gravity estimation, Ph.D. thesis, University of Texas at Austin, 2009.

Schrama, E. J. O., B. Wouters, and D. A. Lavallée, Signal and noise in gravity recovery and climate experiment (GRACE) observed surface mass variations, *Journal of Geophysical Research*, *112*, B08,407, doi: 10.1029/2006JB004,882, 2007.

Seeber, G., *Satellite Geodesy: 2nd Edition*, Walter de Gruyter, Berlin, 2003.

Sharifi, M., N. Sneeuw, and W. Keller, Gravity recovery capability of four generic satellite formations, in *Gravity field of the Earth. General Command of Mapping, ISSN 1300-5790, Special Issue 18*, edited by A. Kilicoglu and R. Forsberg, pp. 211–216, 2007.

Simons, F. J., F. A. Dahlen, and M. A. Wieczorek, Spatiospectral concentration on a sphere, *SIAM Rev.*, *48*(3), 504–536, doi: 10.1137/S0036144504445,765, 2006.

Sneeuw, N., and H. Schaub, Satellite clusters for future gravity field missions, in *Gravity, Geoid and Space Missions*, vol. 129, edited by C. Jekeli, L. Bastos, and J. Fernandes, pp. 12–17, Springer Berlin Heidelberg, 2005.

Sneeuw, N., J. Flury, and R. Rummel, Science requirements on future missions and simulated mission scenarios, *Earth, Moon, and Planets*, *94*, 113–142, 2005.

Sneeuw, N., M. Sharifi, and W. Keller, Gravity recovery from formation flight missions, in *VI Hotine-Marussi Symposium on Theoretical and Computational Geodesy*, vol. 132, edited by X. Peiliang, L. Jingnan, and D. Athanasios, Springer Verlag, 2008.

St. Rock, B., J. J. Blandino, and M. A. Demetriou, Propulsion requirements for drag-free operation of spacecraft in Low Earth Orbit, *Journal of Spacecraft and Rockets*, *43*(3), 594–606, doi: 10.2514/1.15,819, 2006.

Swenson, S., and J. Wahr, Methods for inferring regional surface-mass anomalies from Gravity Recovery and Climate Experiment (GRACE) measurements of time-variable gravity, *Journal of Geophysical Research*, *107*(B9), 2193, doi:10.1029/2001JB000,576, 2002.

Swenson, S., and J. Wahr, Post-processing removal of correlated errors in GRACE data, *Geophysical Research Letters*, *33*, L08,402, doi: 10.1029/2005GL025,285, 2006.

Tapley, B. D., S. Bettadpur, M. Watkins, and C. Reigber, The gravity recovery and climate experiment: Mission overview and early results, *Geophysical Research Letters*, *31*, L09,607, doi:10.1029/2004GL019,920, 2004a.

Tapley, B. D., B. E. Schutz, and G. H. Born, *Statistical Orbit Determination*, Elsevier Inc., San Diego, 2004b.

Thompson, P. F., S. V. Bettadpur, and B. D. Tapley, Impact of short period, non-tidal, temporal mass variability on grace gravity estimates, *Geophysical Research Letters*, *31*, L06,619, doi:10.1029/2003GL019,285, 2004.

Tiwari, V. M., J. Wahr, and S. Swenson, Dwindling groundwater resources in northern India, from satellite gravity observations, *Geophysical Research Letters*, *36*, 2009.

Torge, W., *Geodesy: 3rd Edition*, Walter de Gruyter, Berlin, 2001.

Touboul, P., E. Willemenot, B. Foulon, and V. Josselin, Accelerometers for CHAMP, GRACE, and GOCE space missions: synergy and evolution, *Bollettino di Geofisica Teorica ed Applicata*, *40*, 321–327, 1999.

Ullman, R., SOLVE program mathematical formulation, *Rep. HSTX- G and G-9201*, 1997.

Vallado, D. A., *Fundamentals of Astrodynamics and Applications: Second Edition*, Microcosm Press and Kluwer Academic Publishers, El Segundo, California, 2001.

van Dam, T., P. Visser, N. Sneeuw, M. Losch, T. Gruber, J. Bamber, M. Bierkens, M. King, and M. Smit, Monitoring and modelling individual sources of mass distributions and transport in the Earth system by means of satellites, *Tech. rep.*, Final Report, ESA Contract 20403, 2008.

Velicogna, I., Increasing rates of ice mass loss from the Greenland and Antarctic ice sheets revealed by GRACE, *Geophysical Research Letters*, *36*, 2009.

Visser, P. N. A. M., N. Sneeuw, T. Reubelt, M. Losch, and T. van Dam, Space-borne gravimetric satellite constellations and ocean tides: aliasing effects, *Geophysical Journal International*, *181*(2), 789–805, doi: 10.1111/j.1365–246X.2010.04,557.x, 2010.

Visser, P. N. A. M., E. J. O. Schrama, N. Sneeuw, and M. Weigelt, Dependency of resolvable gravitational spatial resolution on space-borne observation techniques, in *Proceedings of the 2009 IAG Symposium, Buenos Aires, Argentina, 31 August - 4 September 2009*, edited by S. Kenyon and M. C. Pacino and U. Marti, ISBN 978-3-642-20337-4, vol. 136 (Prel.) of International Association of Geodesy Symposia, Springer-Verlag, 2011.

von Storch, H., and F. W. Zwiers, *Statistical Analysis in Climate Research*, Cambridge University Press, Cambridge, UK, 1999.

Wagner, C., D. McAdoo, J. Klokocnik, and J. Kostelecky, Degradation of geopotential recovery from short repeat-cycle orbits: application to GRACE monthly fields, *Journal of Geodesy*, *80*, 94–103, 2006.

Wahr, J., M. Molenaar, and F. Bryan, Time variability of the Earth's gravity field: hydrological and oceanic effects and their possible detection using GRACE, *Journal of Geophysical Research*, *103*(B12), 30,205–30,229, 1998.

Wieczorek, M. A., and F. J. Simons, Localized spectral analysis on the sphere, *Geophysical Journal International*, *162*, 655–675, doi: 10.1111/j.1365–246X.2005.02,687.x, 2005.

Wiese, D. N., W. M. Folkner, and R. S. Nerem, Alternative mission architectures for a gravity recovery satellite mission, *Journal of Geodesy*, *83*, 569–581, doi: 10.1007/s00,190–008–0274–1, 2009.

Wiese, D. N., R. S. Nerem, and S.-C. Han, Expected improvements in determining continental hydrology, ice mass variations, ocean bottom pressure signals, and earthquakes using two pairs of dedicated satellites for temporal gravity recovery, *submitted to Journal of Geophysical Research*, 2011a.

Wiese, D. N., R. S. Nerem, and F. G. Lemoine, Design considerations for a dedicated gravity recovery satellite mission consisting of two pairs of satellites, *submitted to Journal of Geodesy*, 2011b.

Wiese, D. N., P. N. A. M. Visser, and R. S. Nerem, Estimating low resolution gravity fields at short time intervals to reduce temporal aliasing errors, *submitted to Advances in Space Research*, 2011c.

Wolff, M., Direct measurements of the earth's gravitational potential using a satellite pair, *Journal of Geophysical Research*, *74*(22), 1969.

Wouters, B., and E. J. O. Schrama, Improved accuracy of GRACE gravity solutions through empirical orthogonal function filtering of spherical harmonics, *Geophysical Research Letters*, *34*, L23,711, doi: 10.1029/2007GL032,098, 2007.

Wu, X., M. B. Heflin, H. Schotman, B. L. A. Vermeeersen, D. Dong, R. S. Gross, E. R. Ivins, A. W. Moore, and S. E. Owen, Simultaneous estimation of global present-day water transport and glacial isostatic adjustment, *Nature Geoscience*, *3*, 642–646, 2010.

Young, B. C., F. C. Cruz, W. M. Itano, and J. C. Bergquist, Visible lasers with subhertz linewidths, *Physical Review Letters*, *82*(19), 3799–3802, 1999.

Zenner, L., T. Gruber, A. Jaeggi, and G. Beutler, Propagation of atmospheric model errors to gravity potential harmonics-impact on GRACE de-aliasing, *Geophysical Journal International*, *182*(2), 797–807, 2010.